Leveraging Microtechnology to Study Multicellular Microvascular Systems and Macromolecular Interaction

Hesam Parsa

Submitted in partial fulfillment of the
Requirements for the degree of
Doctor of Philosophy
in the Graduate School of Arts and Sciences

COLUMBIA UNIVERSITY

2013

Abstract

Leveraging Microtechnology to Study Multicellular Microvascular Systems and Macromolecular Interactions

Hesam Parsa

Biological systems are large-scale, complex systems comprised of many hierarchical subsystems interacting physico-chemically in a dynamic and coordinated fashion. The complex interactions of subsystems (in micro-scale) lead to the formation of emergent properties (in macro-scale); these are properties that are not visible if individual subsystems are studied.

The inherent high-throughput characteristics of microfabrication technology (microtechnology) along with its ability to manipulate biological species at the micro-scale makes it an ideal tool to elucidate the mechanisms leading to the formation of emergent properties at the macro-scale. In this dissertation, by combining microtechnologies with advanced computational algorithms, we demonstrate system-level analysis of biological systems in development and disease.

The abundance of high quality molecular and genetic data along with the drastic increase in computational power resulted in considerable progress in genomics, epigenomics and proteomics, but not for the so-called cellomics as we define it here: high-throughput study of single-cell phenotype and heterotypic cell-cell interaction via micromanipulation and bioinformatics analysis. Lack of high-throughput robust experimental tools is the major roadblock to cellomics. Using microtechnologies, in the context of developmental biology we studied vascular tissue morphogenesis (vasculogenesis). Formation of microvessels is of critical significance in development and for vascularizing newly engineered tissues in regenerative medicine. First, we sought to map the heterogeneous morphodynamic behavior of individual

clonal cells in the process of capillary-like structure (CLS) formation (Chapter 2 and 3). Then we looked into deciphering the role of extracellular matrix (ECM) mediated mechanical signals in deriving the process of CLS formation (Chapter 4).

In the second half of this thesis, we demonstrated the capabilities of microtechnologies and advanced computational algorithms in tackling the challenging problems in disease: global health diagnostics and cancer drug screening. First, we studied the performance of microfluidic-based diagnostic as a large-scale complex system under real-world constraints (Chapter 5). Then, we present the development of two microfluidic-based platforms to study the heterotypic interaction of cells in both a biomimetic *in vitro* and a realistic *in vivo* setting. We developed an implantable construct carrying a densely-packed heterogeneous panel of tumor cells. This platform could ultimately be used to test anti-cancer drug efficacy against a large number of genotypes in an *in vivo* setting (Appendices A and B).

Together, these methods provide a powerful suite of tools for high-throughput analysis of biological species at the micro-scale and could potentially unlock the mysteries behind the emergent properties observed at the macro-scale.

Table of Contents

List of Figures……..……v

Acknowledgements……..……vii

Chapter 1 Overview 1

1.1 Introduction 1

1.2 Organization 6

Chapter 2 Characterizing population dynamics during microvasculogenesis 12

2.1 Introduction 12

2.2 Methods 16

2.2.1 Preparation of Matrigel 16

2.2.2 Cell labeling and delivery to Matrigel 17

2.2.3 Data acquisition 18

2.2.4 Image segmentation 19

2.3 Results 22

2.3.1 Unique challenges in single-cell tracking of tissue morphogenesis 22

2.3.2 Multispectral fluorescence microscopy enables accurate single-cell tracking 24

2.3.3 Microvasculogenesis occurs in five distinct and reproducible phases according to quantitative analysis of collective multicellular behavior 25

2.4 Discussion 30

2.4.1 Mechanism of microvasculogenesis 30

2.5 Conclusion 31

Chapter 3 Uncovering the behaviors of individual cells within a multicellular microvascular community 32

3.1 Introduction 32

3.2 Methods 32

3.2.1 Clustering algorithm 32

3.2.2 Initial inhibition of nonmuscle myosin II 34

3.2.3 Classification of cells as nodes or branches 35

3.3 Results 35

3.3.1 Behaviors of most endothelial cells follow a handful of unique patterns 35

3.3.2 Population-averaged measurements mask the trends of most individual endothelial cells 38

3.3.3 Cells in superficially similar microenvironments diverge in behaviors and fates 40
3.3.4 Initial inhibition of myosin II changed subsequent displacement dynamics and fates 41
3.3.5 Cellular behavior can exhibit large variations with different types of distributions 42
3.4 Discussion 45
3.4.1 Mechanism of microvasculogenesis 45
3.4.2 Means and variations of cellular phenotypes 46
3.5 Conclusion 47
Chapter 4 Role of ECM-mediated strain propagation in microvascular tissue formation 48
4.1 Introduction 48
4.2 Methods 49
4.2.1 Preparation of fluorescent bead-laden Matrigel layer for PIV 49
4.2.2 Single-cell patterning using non-adherent PDMS stencil 49
4.2.3 Image Acquisition 51
4.2.4 Image Processing and Data Acquisition and Processing 51
4.3 Results 55
4.3.1 Patterning an array of single-cells on Matrigel 56
4.3.2 Particle Image Velocimetry (PIV), and Finite Element Analysis (FEA) capture the cell-to-cell transmission of mechanical signals in real-time 58
4.4 Discussion 60
4.5 Future work 61
Chapter 5 Modeling analyte capture and enhancement strategies in microfluidic heterogeneous immunoassays under real-world constraints 65
5.1 Introduction 65
5.2 Methods 67
5.2.1 Theoretical background and numerical simulation of analyte capture process ... 67
5.2.2 Extension of current computational framework to study analyte-capture in two-phase flow 69
5.2.3 Device design and fabrication 70
5.2.4 Heterogeneous immunoassay for analyte capture 70
5.2.5 Immunoassays for kinetics of gold-silver enhancement 72
5.3 Results 72
5.3.1 Basic description of theoretical model 72
5.3.2 Modeling of capture of analytes without real-world constraints 73

5.3.3 Physical regimes of analyte-capture process 75
5.3.4 Simulation under real-world constraints: finite volume and time 79
5.3.5 Effect of dilution into larger plug volume: fixed amount 80
5.3.6 Experimental Microfluidic Binding Assays 82
5.3.7 Inherent transport limitation in conventional microfluidic: vortex-like flow as a remedy 84
5.3.8 Gold-silver signal enhancement 86
5.4 Discussion 91
5.5 Conclusion 92
Chapter 6 Conclusion 94
Appendix 1. To develop a real-time microfluidic system for studying mammalian cells in 3D microenvironments 97
1.1. Introduction 97
1.2. Methods 98
1.2.1. Device design and fabrication 98
1.2.2. Culture of mammalian cells and preparation of cell-encapsulated 3D ECM 100
1.2.3. Operation of microfluidic chip: loading of cells and ECM and perfusion of reagents 101
1.2.4. Fluorescence microcopy 104
1.3. Results 104
1.3.1. Design and fabrication of microfluidic system 104
1.3.2. Loading of 3D ECM and cells into microchambers 106
1.3.3. Perfusion through 3D ECM 108
1.3.4. Culture and staining of mouse embryonic stem cells inside 3D ECM 112
1.4. Discussion 115
1.5. Conclusion 116
Appendix 2. To develop a platform to accurately identify *in vivo* drug efficacy across heterogeneous genotypes 117
2.1. Introduction 117
2.2. Methods 119
2.2.1. Construct design and fabrication 119
2.2.2. Cancer and stromal cells culture 121
2.2.3. Hedgehog (HH) pathway reporter 121
2.2.4. Construct cell loading and culture 122

2.3. Results 122
2.3.1. Construct fabrication 123
2.3.2. Cell loading for *in vitro* cross-talk experiment 124
2.3.3. Luciferase assay 125
2.4. Discussion 127
Bibliography……130

List of Figures

Figure 1-1: Large-scale systems 2
Figure 1-2: Microtechnologies and advanced computational algorithms in development and disease 3
Figure 2-1: Background - Tissue formation analysis and modeling 14
Figure 2-2: Snapshot of three different capillary-like structures (CLS) 16
Figure 2-3: Experimental setup 17
Figure 2-4: Data collection and image processing. 20
Figure 2-5: Imaging of microvasculogenesis 25
Figure 2-6: Dynamics of morphological and motility phenotypes during microvasculogenesis 26
Figure 2-7: Deviation of n-cell-averaged behavior from population-averaged behavior. 27
Figure 2-8: Staining group comparison for triplicate data. 29
Figure 2-9: Dynamics of morphological and motility phenotypes during microvasculogenesis, based on averages across cell population 29
Figure 2-10: Schematic model of CLS formation 29
Figure 3-1: Clustering of cells with similar temporal variations in phenotypes. 34
Figure 3-2: Schematic diagram of stress-fiber formation inhibition). 35
Figure 3-3: Clustering of cells with similar temporal variations in phenotypes. 36
Figure 3-4: Five very similar patterns of displacement dynamics. 37
Figure 3-5: Classification of cells with similar temporal variations in phenotypes. 38
Figure 3-6: Behaviors of cell clusters relative to the population-averaged behavior 39
Figure 3-7: Clustering of cells with similar temporal variations in phenotypes. 40
Figure 3-8: Correlation of migratory dynamics to structural role in final plexus 41
Figure 3-9: Correlation of migratory dynamics to structural role in final plexus 42
Figure 3-10: Variations in behavior from cell to cell. 44
Figure 4-1: Intercellular mechanical signaling 56
Figure 4-2: Setup preparation 57
Figure 4-3: Single-cell patterning on Matrigel 58
Figure 4-4: Mechanically-guided cell movement 59

Figure 4-5: Biochemical stimuli. 61

Figure 4-6: Establishing growth factor gradient. 62

Figure 4-7: Deciphering the role of mechanical versus chemical stimuli in microvascular tissue formation..... 64

Figure 5-1: Schematic diagram of the physical processes and experimental setup of a microfluidic-based heterogeneous immunoassay. 67

Figure 5-2: Captured analytes predicted by finite-element models as a function of flow rate, under three operating scenarios without real-world constraints. 75

Figure 5-3: Identification of physical regimes in microfluidic heterogeneous immunoassays ... 78

Figure 5-4: Concentration of captured analytes C_s predicted by FEM and also experimental microfluidic binding assays as a function of flow rate Q, under the real-world constraints of finite volume (5 mL). At the simulated flow rates in this figure (except for Q=0.01 mL/min), the actual time of the assay is less, since the entire plug of sample passes through the channel before the maximum allowable assay time (20 min). 81

Figure 5-5: Two-phase flow..... 85

Figure 5-6: Modeling of silver development.. 87

Figure A1-1: Design and structure of the microfluidic setup…….……106

Figure A1-2: Demonstration of actuation of valves……..…….…108

Figure A1-3: Characterization of ring-shape microvalves and microposts..……..110

Figure A1-4: Fluid modeling of perfusion efficiency…….……111

Figure A1-5: Flow study of mouse ES cells in chambers of 3D Matrigel inside microfluidic chip……...113

Figure A2-1: Overall experimental strategy and schematic of tumor cell laden construct……123

Figure A2-2: Construct fabrication…..…….…….…….124

Figure A2-3: Construct loading for in vitro cross-talk assay…….…….125

Figure A2-4: Luciferase assay. …….….…126

Acknowledgements

Six years ago, I embarked on a journey 6,000 miles away from home to pursue graduate studies, and little did I know that I would not be able to return to my family in Iran anytime soon. The first scenes of New York from the plane were gloomy and sad when I was first flying over the Atlantic Ocean into Queens on an August evening. Then I got lost in Manhattan struggling with two huge suitcases and intimidating skyscrapers hovering over my head. It took me quite some time to adapt to the new environment, settle down, and discover the beauty of the city. My experience at Columbia University has been unique and very rewarding, which helped me to prosper personally and scientifically. This journey was not possible without love, help, support and the guidance of many people.

I would like to express my extreme gratitude to my parents, Afsaneh and Manoochehr, for their love, sacrifice, and all of their efforts to shape my character, and I would like to thank my siblings, Hosein and Hosna, for their love and support. Dr. Samuel Sia, my PhD advisor, has been the one graciously helping me with my thesis and all of my academic endeavors throughout these years. I would like to thank him for his mentorship, support, and patience to train me as a scientist. I would like to express my respect and admiration for his knowledge, vision, management, dedication, and hard work that goes into running the lab.

I would also like to thank the committee members, Dr. Gordana Vunjak-Novakovic, Dr. Clark Hung, Dr. Lance Kam and Dr. Jeremy Mao for their advice, perspective and generosity with their time. They have been a precious source of inspiration to me and their valuable feedback shaped this research. Also, I would like to thank Dr. Vunjak-Novakovic and Dr. Kam for generously letting me use their lab equipment.

I would also like to thank the members of Sia lab, especially Dr. Curtis Chin, Dr. Yukkee Cheung, and Dr. Brian Gillette for all their help and support throughout these years. Although they are younger or the same age as me, they were like older siblings to me; I admire their character, knowledge, and passion for science. Similarly, I would like to thank Dr. George Eng, Dr. Olga Ordeig, Dr. Zuankai Wang, Tassaneewan Laksanasopin, Sau Yin Chin, Tiffany Guo, Nalin Tejavibulya, Tatiana Kniazeva, Mario Modena, Angelo Angelini, Paolo Cadinu, Benjamin Lee, Amandine Godier, Dr. Stanly Huang, Dr. Andrew Baik, all lovely people in Kam lab, and so many others for all of their help throughout these years and for making these times very much enjoyable. Special thanks to Keith Yeager for generously sharing his prototyping knowledge with me. Thanks to Jarmaine Lomax, Michelle Cintron, Paulette Louissaint, and Shila Maghji. Throughout these years, I had the opportunity to work with many undergraduate and master students; I want to thank them all, especially, Ranjan Upadhyay and Sophie Wang without them I could not have finished this thesis. I would also like to thank my Iranian friends, Ali, Aboozar, Babak, Behrooz, Ehsan, Elaheh, Hasti, Hooman, Hami, Marjan, Mazdak, Orkideh, Peyman, Reza, Sina, Sasan, Setareh, Sheida, Saba, Siavash, Sepideh, and many others who have been like family to me throughout these years.

Lastly, I would like to express my gratitude to my previous advisors: Dr. Ali Ghaffari, Dr. Mansour Nikkhah-Bahrami, Dr. and Souran Manoochehri, to my fourth-grade teacher, Ms. Gholami, whose dedication and love changed my attitude toward life, to my dear friend Amir Poursamad, and to my spiritual mentors, Mohammad Yousefi and Dr. Hossein Kamali.

Hesam Parsa

New York, New York

April, 2013

Chapter 1 Overview

1.1 Introduction

Starting with the seminal works of Norbert Wiener in the 20th century, system-level analysis of biological systems, known as **systems biology**, has become a recurrent theme [1]. In the beginning of the 21st century with, a plethora of microscale biological and chemical data, scientists have refocused on systems biology with the ambition of discovering, analyzing and modeling "*emergent properties*" in large scale complex systems. As an interdisciplinary approach, systems biology has two main objectives: (1) understand and control the behavior of large scale (biological) systems by considering the interaction of its components (molecules, genes, proteins, cells, etc.) and (2) study cellular and molecular interactions using a combined approach of mathematical modeling and experimentation [2]. As opposed to the reductionist approach that says a complex system is nothing but the sum of its parts, a systems approach focuses on the interactions of the components to discover the emergent properties (Figure 1-1A).

High-throughput experimental techniques have been developed to generate sufficient data to describe the complex interaction of biological elements. Yet, reliable and robust techniques are mainly established for genetic and molecular screening, resulting in a considerable progress in genomics, epigenomics and proteomics but not for so-called cellomics. Every living organism is a large-scale complex system which is comprised of many hierarchical subsystems. A vertebrate organism, for instance, is comprised of many complex organs, such as a vascular system--itself is formed from different cell types including endothelial cells. In order to unravel complex patterns of vascular formation, in addition to decoding the integrated networks of gene, protein and

metabolites the dynamic interaction of endothelial cells, as the basic unit of vasculatures, should be scrutinized (Figure 1-1B).

Microtechnologies, with the inherent properties suitable for high-throughput manipulation of micro-sized biospecies has the potential to significantly advance systems biology by overcoming limitations hindering the currently available instrumentation. However, many breakthroughs in experimental devices, advanced software, and analytical methods are required before the achievements of systems biology can live up to its advertised potentials.

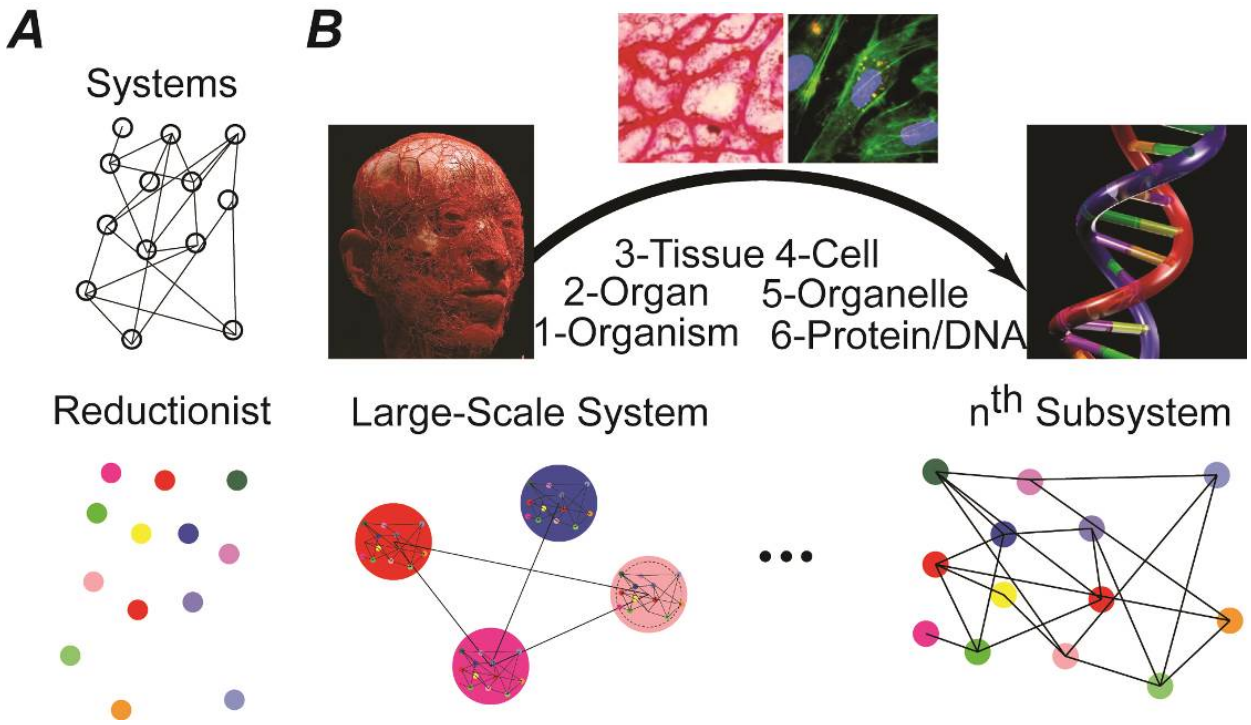

Figure 1-1: Large-scale systems. (A) Systems versus reductionist approach **(B)** Hierarchical, multicomponent, multidimensional and miniaturized systems

The central premise of this thesis is to combine microtechnologies with advanced computational algorithms to facilitate the systematic collection and analysis of large sets of molecular and cellular data in development and disease (Figure 1-2).

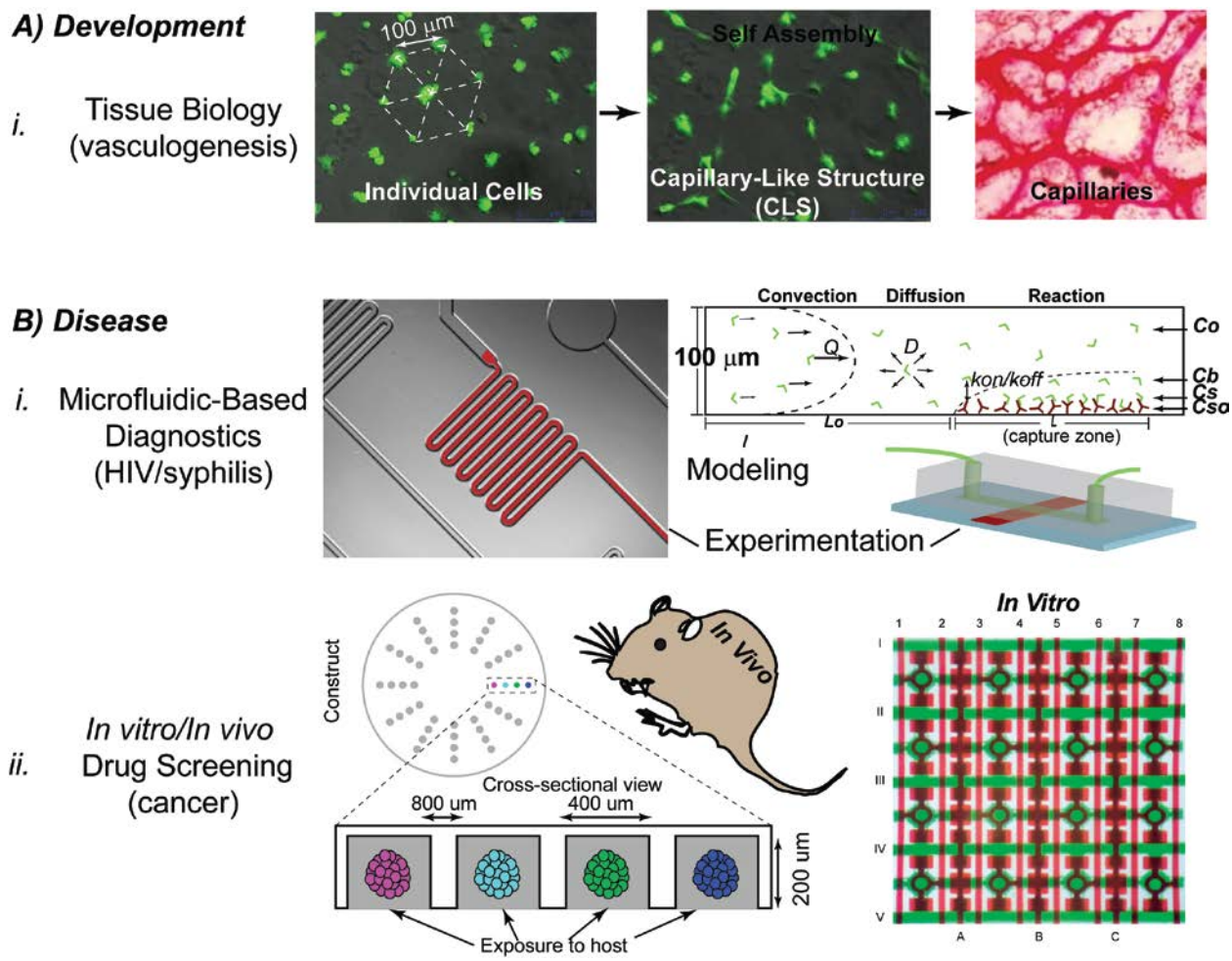

Figure 1-2: Microtechnologies and advanced computational algorithms (A) Development**:** i. Vasculogenesis **(B)** Disease: i. Microfluidic-based diagnostics and ii. *In vitro/in vivo* drug screening

The systematic study of developmental biology started with the morphological description of fixed structures; however, lack of appropriate tools to map the dynamics of cellular behavior within a multicellular community hindered the system-level analysis of tissue formation. Although, there are scattered efforts to model the emergent behavior of cells during tissue morphogenesis, due to segregation of experimentation and modeling, these models generally do not provide valuable insight into the role of individual cells in tissue formation; normally, the experimental results are under-analyzed or the proposed models are far from reality.

Formation of new capillaries, the smallest of the microvessels, can take place via vasculogenesis – the *de novo* formation of vascular networks from dispersed endothelial cells – mainly during prenatal development and also in adults. To address the daunting complexity of vasculogenesis arising from multiple phenotypic behaviors governed by multiple stimuli, numerous mathematical and computational approaches (e.g. continuum, discrete, deterministic and stochastic) at different levels (single-cell, multi cell and tissue) have been developed [3]. However, all these models share the common drawback of lacking extensive experimental data. Microtechnologies provide the opportunity to manipulate the microenvironment of endothelial cells and record their phenotypic behavior in a high-throughput fashion. As part of this thesis, while teasing out the underlying cues deriving vasculogenesis, we map the morphodynamic behavior of endothelial cells to understand the role of individual cells in the formation of emergent vascular patterns (Figure 1-2A). Ultimately, this could pave the way for vascularization of engineered tissues and re-establishing blood flow in ischemic tissues.

In the second half of this thesis, we demonstrate the capabilities of microtechnologies in tackling the challenging problems in disease: global health diagnostics and cancer drug screening.

First, we study the performance of microfluidic-based diagnostic as a large-scale complex system under real-world constraints (Figure 1-2Bi). One of the greatest challenges of science and technology is to develop technologies that could improve health in the world's poorest regions. One successful example is the development of diagnostic devices for infectious disease such as HIV/syphilis. Microtechonologies have a tremendous but unproven potential to improve the health of people in developing countries. Despite the much-touted potentials of microfluidic-based diagnostic devices, there is an incomplete understanding of how the performance of the

assay (sensitivity and specificity) under real-world constraints (limited sample and time), could change as design parameters (e.g. flow rate, geometry of the microchannels) change. Here using the combined experimental and computational approaches, we try to establish a framework to determine the sweet spot for these assays.

Then, we present the development of two microfluidic-based platforms to study the heterotypic interaction of cells in both a biomimetic *in vitro* and a realistic *in vivo* setting (Figure 1-2Bii). The World Health Organization lists cancer as the leading cause of global mortality, with an estimated 8 million deaths and 13 million new cases diagnosed each year [4]. Cancer is a large heterogeneous class of disease states comprising 200 different types. To capture the heterogeneity of this disease, the U.S. National Cancer Institute (NCI) established a platform of 60 human tumor cell lines in the late 1980s; this platform was primarily developed as an *in vitro* drug-discovery tool intended to supplant the use of transplantable animal tumors in anticancer drug screening [5]. Cancer heterogeneity, however, lies not only in the cancer cells but also in the stromal cells (e.g., endothelial cells, fibroblasts, macrophages, myeloid-derived suppressor cells, TIE2-expressing monocytes, and mesenchymal stem cells) and their interaction with cancer cells. The challenge is that using current techniques, where the *in vivo* testing of one genotype requires one host animal, it is extremely difficult to predict the *in vivo* efficacy of lead compounds across a large number of genotypes. As a result, only a very small number of genotypes of patient subpopulation is tested in the expensive Phases II and III, and otherwise promising lead compounds that pass Phase I can easily fail in Phase II and III trials. The end product is a non-ideal process where lead compounds with high safety and favorable ADME-Tox are discarded completely due to lack of “efficacy”, even though such compounds may in fact be effective for other cancer genotypes. Leveraging microtechnologies, we developed a platform

where compounds can be tested for efficacy against a large number of genotypes in an *in vivo* setting while the host tumor interaction could be quantified in a high-content and high-throughput fashion.

In some cases, however, we have to study cell-cell (host-tumor) interaction in a tightly-regulated microenvironment which is feasible in a biomimetic *in vitro* setting. The development of microfabricated systems for biological applications has resulted in methods that allow for exquisite control over cellular microenvironments. For example, cells can be spatially positioned to micron resolution, and chemicals can be delivered to cells to subcellular spatial resolution [6-8]. Using microtechnologies, we can impart real-time, dynamic control over the 3D environments of an array of cells while also incorporating the ability to study chamber-to-chamber communication of diffusible factors from one cell type (host) in one chamber to another cell type (tumor) in another. Hence, as part of this thesis we develop a microfluidic system with embedded microvalves to study cells in 3D environments in individually addressable chambers.

1.2 Organization

During the past two decades with the development of sophisticated microscopy techniques, image analysis algorithms and more importantly cloning of GFP and its variants, much of the difficulties to study the role of single cells in tissue formation have been overcome. In the first part of this thesis, and in light of achieving the first objective of the systems biology by focusing on vascular tissue formation, we study the behavior of individual endothelial cells during the process of capillary-like structure (CLS) formation.

Currently, efforts in the analysis and modeling of tissue formation are largely based on the bulk average behavior of cells. Bulk averaging is limiting in describing complex, multicomponent interactions in tissue formation. Considering single cells as the building block

of the tissues, analogies have been made with the soft materials (e.g. liquid foam). In this thesis, first we developed a methodology that facilitates the single cell analysis of CLS formation (Chapter 2); then we characterize single cell behavior and the extent of cell-to-cell variation (Chapter 3) and analyze the roles of ECM-mediated mechanical signals during the process of CLS formation (Chapter 4).

The complexity of the microscale phenomena is not limited to biological systems, but it could be found in many multicomponent/dimensional systems. The complexity level increases as the number of design parameters on the microscale system increases. As an example, there are at least 8 independent parameters [9] that determine the dynamics of analyte capture in microfluidic-based heterogeneous immunoassay (where analytes in solution are captured on a solid surface functionalized with a capture molecule). Despite the prevalence of these assays, there is incomplete understanding of how assay parameters affect their efficiency (optimal analyte capture). In the light of systems biology's second objective and due to the scarcity of combined experimental/computational study of these assays, we studied the analyte capture dynamics, both computationally and experimentally, under real-world constraints (Chapter 5). More importantly, we integrated the expertise of two largely distinct communities: those developing and employing these biotechnologies, and those who have developed and mastered techniques for understanding these physicochemical effects (albeit in the context of different systems).

In order for readers to easily digest the information and relate the different aspects of this thesis, the contents of this dissertation are organized in the following manner:

Chapter 2: Quantifying endothelial cell population dynamics during microvasculogenesis, through single-cell measurements.

We developed an experimental and computational methodology for the system level analysis of capillary like structure (CLS) formation. We quantified the previously qualitatively described process of plexus formation. In a broader term, we set the stage to quantify the process of tissue morphogenesis for those tissues with complex patterns of movement and deformation over time. This work has been published as part of: Parsa, H., Upadhyay, R., Sia, S. K., Uncovering the behaviors of individual cells within a multicellular microvascular community, ***Proc. Natl. Acad. Sci. (PNAS)***, 2011, 108, 5133-38.

Chapter 3: Discovering distinct morphodynamic patterns of individual cells within a multicellular microvascular community.

Following the developed methodology (as described in the previous chapter), we studied the behavior of individual endothelial cells during CLS formation and identified specific morphodynamic patterns. We specifically tried to understand (1) if the population averages are good representative of single cell behavior? (2) the extent of cell-to-cell variation across the population? and finally (3) the significance of a specific behavior of individual cells? This work has been published as part of: Parsa, H., Upadhyay, R., Sia, S. K., Uncovering the behaviors of individual cells within a multicellular microvascular community, ***Proc. Natl. Acad. Sci. (PNAS)***, 2011, 108, 5133-38.

Chapter 4: Deciphering the role of ECM-mediated strain propagation in microvascular tissue formation

Following the initial characterization of the cell-to-cell variation and identifying the dominant patterns of cell motility in the previous chapters, we seek to identify the underlying intercellular communication mode in deriving the process of CLS formation and creating distinct cellular behavior. We developed a methodology to decipher the roles of mechanical cues in

directing the migration of endothelial cells in the early stages of vasculogenesis. This method uses timelapse live-cell fluorescence microscopy followed by automated analysis of endothelial cells (ECs) migration and ECM deformation. We used particle image velocimetry (PIV) combined with finite element analysis (FEA) to measure/simulate the mechanical signals sensed by ECs. Inference of spatiotemporal relationship between mechanical cues and ECs migration could be easily drowned in low sample sizes or noisy population data. To increase the sample size and in order to ensure a uniform initial condition for all cells within the population, we patterned single cells on Matrigel via sedimentation through a non-adhesive PDMS stencil. The manuscript for this chapter is in preparation.

Chapter 5: Effect of volume- and time-based constraints on capture of analytes in microfluidic heterogeneous immunoassays under real-world constraint - alternative methods to surpass the inherent limitations of these conventional systems by: (A) Introduction of multiphase flow to enhance analyte transport. (B) Signal amplification with gold-silver development.

Despite the prevalence of microfluidic-based heterogeneous immunoassays, there is incomplete understanding of how assay parameters influence the amount of captured analytes. We studied the analyte capture under variations in both mass transfer and surface binding, constrained by real-world assay conditions of finite sample volume, assay time, and capture area. Following the study of analyte capture efficiency, in a traditional ELISA-based microfluidic assay under real-world constraints, we sought alternative methods to surpass the inherent constraints of this system, namely, transport limitation and signal strength. First, we studied the effect of creating a localized vortex-like flow to enhance the transport of analyte toward the binding sites. In the second section we to predicted the extent of silver formation under a range

of surface gold density and silver development time in order to minimize total assay time. This work has been published in: Parsa, H., Chin, C. D., Mongkolwisetwara, P., Lee, B. W., Wang, J. J., Sia, S. K., Effect of volume- and time-based constraints on capture of analytes in microfluidic heterogeneous immunoassays, ***Lab Chip*** 2008, 8, 2062-70 and Chin, C., Laksanasopin, T., Cheung, Y. C., Steinmiller, D., Linder, V., Parsa, H., Wang, J. J., Moore, H., Rouse, R., Mwamarangwe, L., Braunstein, S., Wijgert, J., Sahabo, R., Justman, J., El-Sadr, W., Sia, S. K., Microfluidics for global health: a miniaturized multi-step immunoassay for diagnosis of infectious diseases, ***Nature Medicine*** 2011, 17, 1015–19.

Appendix A: Real-time microfluidic system for studying mammalian cells in 3D microenvironments.

We developed a microfluidic system that can control, in real-time, the microenvironments of mammalian cells in naturally derived 3D extracellular matrix (ECM). This chip combines pneumatically-actuated valves with an individually addressable array of 3D cell-laden ECM; actuation of valves determines the pathways for delivering reagents through the chip and for exchanging diffusible factors between cell chambers. To promote rapid perfusion of reagents through 3D gels (with complete exchange of reagents within the gel in seconds), we created conduits above the gels for fluid flow, and microposts to stabilize the gels under high perfusion rates. As a biological demonstration, we studied spatially segregated mouse embryonic stem cells and mouse embryonic fibroblasts embedded in 3D Matrigel over days of culture. Overall, this system may be useful for high-throughput screening, single-cell analysis and studies of cell-cell communication, where rapid control of 3D cellular microenvironments is desired. This work has been published in: Lii, J., Hsu, W. J., Parsa, H., Das, A., Rouse, R., Sia, S. K., Real-time

microfluidic system for studying mammalian cells in 3D microenvironments**, *Anal Chem*** 2008, 80, 3640-7.

Appendix B: High-throughput screening platform for assessing the efficacy of a candidate drug across a genetically heterogeneous platform of tumor cells.

We developed a novel microfluidic system that allows us to create a cassette holding a large number of individually addressable chambers. The end result is a device similar to a 96-well or 386-well plate, except that the entire device is only millimeters in dimensions and thickness, so upon implantation into an animal host, it facilitates probing of cancer drugs across genetically heterogeneous platform of tumor cell lines in a physiologically more realistic *in vivo* setting. Firstly, we tried to rule out the possibility of cross-talk between the chambers of this construct, we performed *in vitro* control experiments by loading the chambers with only two tumor cell lines, HH ligand expressing (HT-29) and non-expressing (DLD-1) cell lines, and studied the effect of HH ligand secreted from the HT-29 cells on the stromal cells (10T1/2 fibroblast) associated with the DLD-1 cells. By optimizing the geometries, we can minimize the cross-talk effects between chambers. The main advantage of this platform, upon final development, is that all cells are screened in a single host, to minimize host-to-host variability, a significant source of variation in conventional animal host experiments.

Chapter 2 Characterizing population dynamics during microvasculogenesis

2.1 Introduction

Currently, programming the behaviors of individual cells is experimentally tractable and can be manipulated to produce emergent multicellular behavior [10, 11]; hence, information about native cellular behavior would be useful for tissue engineering and synthetic biology. However, this seems to be fairly far-reaching as the cellular morphodynamic behavior of individual cells during tissue formation is still largely unknown.

How the individual cell behavior leads to specific pattern is also an important open question in biology as functions of many tissues are dependent on the shape of their comprising cells; for example, hexagonal packing of the epithelial cells in the vertebrate lens minimizes light scattering from plasma membranes and increases transparency. Considerable effort has been devoted to understand the role of underlying molecular mechanism in cells and consequently tissue shape formation. For example, to understand how epithelial cells in Drosophila eye are organized as a hexagonal array of repeating multicellular units (ommatidia - Figure 2-1A left), Hilgenfeldt et al. studied native and mutant epithelial cells and showed that by only considering interfacial forces through cadherins and cell membrane elasticity, it is possible to recreate these patterns *in silico*; hence, they concluded that these two factors are the only determining factors in Dorsophila pupal retina pattern formation [12]. Such modeling efforts are formulated under quasi-static condition; however, individual and collective movement of cells have been shown to play a significant role in tissue pattern formation [13].

Hence, numerous studies tried to map the collective cellular movement during embryogenesis and adult tissue development, but they are either merely qualitative [13] or, in case they are quantitative, the scope of their application is very limited. For instance, almost all of the studies that tried to model the deformation of epithelial monolayer, considered tissue to be a continuum rather than collection of individual cells; they mainly rely on analogies of tissues to other materials such as liquid foams or granular materials and assumed that cell division or death are analogous to bubble formation and shrinkage in the liquid foam. As an example, the dynamic of tissue formation in Drosophila germband elongation is modeled as a continuum [13, 14]. Normally, these studies have emphasized on the role of adhesion molecules and actomyosin cortical tension in cell shaping and tissue patterning. These models predict some properties of epithelia at equilibrium or at steady states, such as liquid-like phase separation of mixed cells controlled by differential adhesion as well as topological and packing features, reflecting the balance of cortical elasticity and adhesion. Although, they might be effective to understand the simple case of epithelial monolayer tissue formation; they are incapable of modeling the complex morphodynamic behavior of more complicated tissues such as endothelial cells movement and shape change during capillary formation.

Lack of a comprehensive model that could explain complex tissue formation is partly due to the lack of accurate and high content microscopy data which is due to the challenges in live-cell imaging of tissue formation to single cell resolution. Some of these challenges are the need for high spatiotemporal resolution, ultralow photobleaching rates, excellent signal-to-noise ratio, and the ability to resolve single cells. Hence, we aim to directly track the behavior of every individual primary endothelial cell during the early stage of human microvascular tissue formation. Formation of microvessels is central to the etiology of many diseases [15] and critical

for vascularizing newly engineered tissues for regenerative medicine [16]. Formation of new capillaries, the smallest of the microvessels, can take place via vasculogenesis – the *de novo* formation of vascular networks from dispersed endothelial cells – during both prenatal development and in adults. For nearly three decades, microvasculogenesis has been studied using well-established *in vitro* models [17, 18]. In particular, starting with Folkman to recent studies [17, 19, 20], soft gels such as Matrigel have remained the most well-established *in vitro* system for controllably studying the initial steps of microvasculogenesis. Endothelial cells on Matrigel undergo tubule formation with mechanisms corresponding to those of native vascular plexus assembly [21, 22], and final structures emulating those observed *in vivo* [21-23].

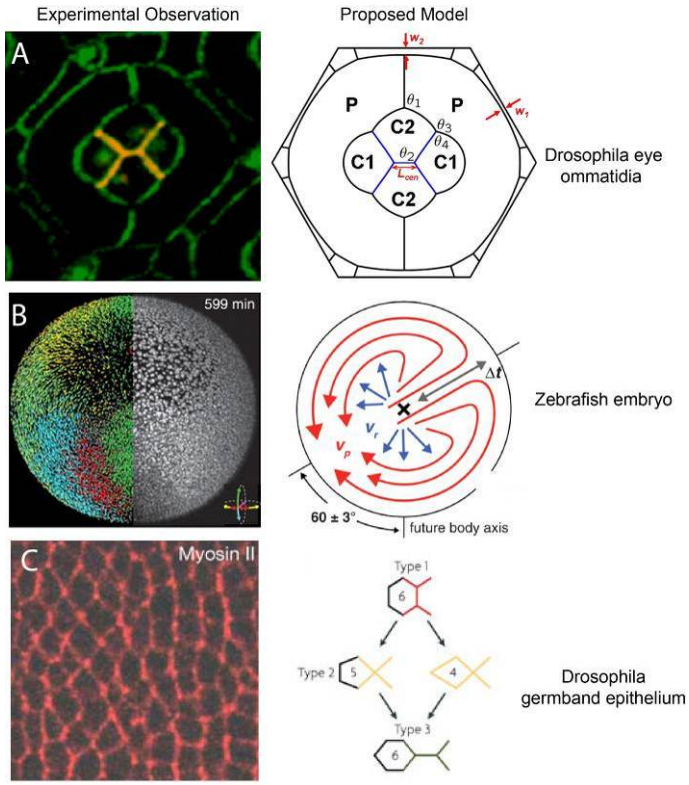

Figure 2-1: Background - Tissue formation analysis and modeling. (A) Left: Double-stained confocal fluorescence image at the AJ plane of a Dorsophila pupal retina (age, 48 h). Antibody staining highlights E-cadherin (green) and N-cadherin (red); Right: Nomenclature and geometry of the modeled ommatidium. Indicated are the C1 (anterior and posterior cone), C2 (equatorial and polar cone), and P (primary pigment) cells, and the angles for the upper-right quadrant. The edge between the two C2 cells has length Lcen, and the widths of the secondary pigment cells attached to one (w1) or two (w2) P cells are shown. All edges carry E cadherin, whereas the edges between C cells (blue) carry both E- and N-cadherin. **(B)** Left: Cell tracking in Zebrafish - Microscopy data (right half of

embryo: animal view, maximum projection) and digital embryo (left half of embryo) with color-encoded migration directions. Color code: dorsal migration (cyan), ventral migration (green), toward or away from body axis (red or yellow), toward yolk (pink morphologies of three cells over the time course of the assay. Right: Model of symmetry-breaking of the global cell division pattern. **(C)** Left: Antero-posterior elongation of the Drosophila melanogaster germband epithelium (red: Myosin II). Right: Models proposed for three patterns of cell deformation.

As such, numerous studies have used phase-contrast microscopy to visualize microvasculogenesis on Matrigel [20, 24]. These studies have provided valuable information on the collective behaviors of the cellular population, but the mechanistic knowledge has largely been qualitative: aggregation of endothelial cells or angioblasts, elongation of cells into cord-like structures, and organization of vascular segments into CLS [25]. Some of these studies have measured geometric properties of the CLS at fixed endpoints [20], including changes of the vascular plexus in response to angiogenic modulators, but such measurements were typically at a fixed end point and averaged across the whole cellular population, rather than following the dynamic behaviors of individual cells. Hence, there remain critical unanswered questions for understanding the mechanism of how individual endothelial cells evolve over time.

Fixed-time analyses could be misleading as they do not provide enough information to deduce the mechanism underneath. For instance looking at the three snapshots of capillary tissue, we cannot conclude that if these cell populations went through a same procedure to reach the final pattern or not (Figure 2-2)? Is this process reproducible or random? How important is the role of initial cell arrangement? In this chapter we aim to develop a methodology to specifically answer these questions.

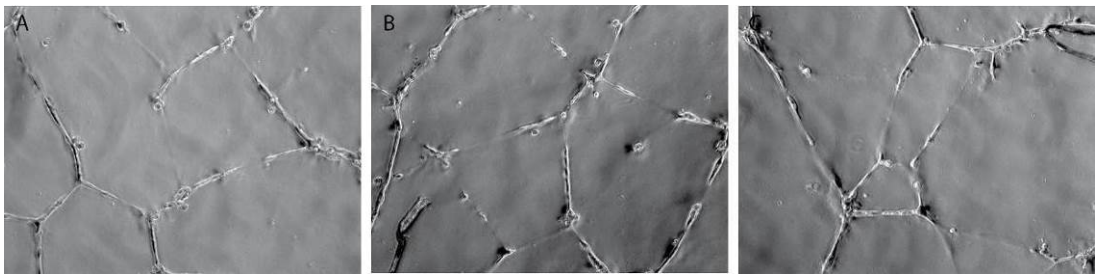

Figure 2-2: Snapshot of three different capillary-like structures (CLS)

2.2 Methods

We seeded primary HUVECs on a Matrigel (BD Biosciences) molded to form a flat-top surface, and we collected data with live-cell imaging. We performed quantitative analysis on images and extracted the morphology and motility phenotypes for every cell. One-way ANOVA showed that cellular behaviors across three independent trials were not significantly different. We adapted a correlation clustering algorithm based on pairwise comparisons to identify cells with similar temporal dynamics. Below we described the procedures in more details.

2.2.1 Preparation of Matrigel

Matrigel (BD, Franklin Lakes, NJ) was stored at -20°C and thawed at 4°C, 24 hours prior to usage. It was used at the original concentration from the bottle (8.2 mg/ml). Originally, we filled each well of a 96-well plate with Matrigel, but the hydrophobic walls of the wells caused the Matrigel to form a meniscus which caused the images to blur at the edge of the field of view. In order to avoid blurring of local regions over a relatively large field of view (1183 by 887 µm, using 10X objective), we seeded primary HUVECs (Promocell) on a Matrigel molded to form a flat top surface (as shown in Figure 2-3): We first placed a sterilized 1-mm thick ring-shaped piece of poly(dimethylsiloxane) (PDMS) (inner dia. = 11 mm) inside a 12-well plate culture dish (Figure 2-3, step 1) and then we poured liquid Matrigel inside the ring (Figure 2-3, step 2). Then we placed a slab of BSA-treated PDMS over the liquid solution (Figure 2-3, step 3). After

incubating the 12-well plate at room temperature for 15 min to gel the Matrigel (Figure 2-3, step 4), we removed the BSA-treated PDMS slab (Figure 2-3, step 5) to produce a gel with a flat top surface with no meniscus.

In order to compensate for slight shifts in the field of view due to repeated movements of the motorized stage (in case of multiwell imaging), we placed the Matrigel sample over a grid of fixed fiducial markers. We patterned a thin layer of PDMS with crosses which were 300 to 400 µm apart laterally, and placed this grid beneath the bottom of the dish (Figure 2-3, step 6). (Subsequently, in measurements of cell displacement, we used fiducial markers rather than the boundary of the acquired image as the reference points.)

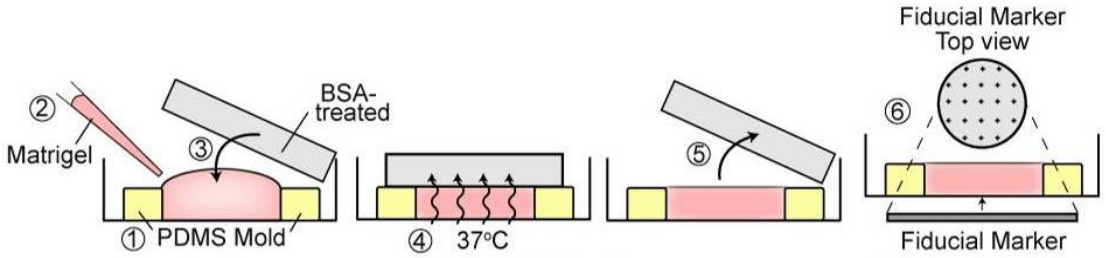

Figure 2-3: Experimental setup. Steps to prepare the microvasculogenesis setup included: 1) Preparation of PDMS mold, 2) Injection of Matrigel solution, 3) Capping of chamber with PDMS treated with bovine serum albumin, 4) Gelling of Matrigel by increasing temperature, 5) Removal of cap to produce gel with flat surface, and 6) Placement of sample on a grid of fiducial markers located on a different focal plane.

2.2.2 Cell labeling and delivery to Matrigel

We labeled cells with PKH (PKH67, green fluorescent dye and PKH26, red fluorescent dye, Sigma, St. Louis, MO) and CellVue® (claret, far red fluorescent dye Sigma, St. Louis, MO) dyes, which are both lipid intercalators. [We also tried a covalent protein tag CFSE (Sigma, St. Louis, MO), Cell Tracker, and Dil, DiO, DiD lipophilic tracers, (Invitrogen Inc, Carlsbad, CA), but these dyes exhibited higher cytotoxicity.] We stained the cells as an adherent monolayer cultured in a T25 flask, so that staining efficiency could be monitored easily; this method also improved cell viability compared to staining the cells in suspension. We adjusted the amount of

dye and incubation time to optimize the level of staining, and kept the cell cultures to about 70% confluent prior to staining. We used a staining condition for PKH67 of 5 µL of dye in 1 mL of Diluent C (Sigma, St. Louis, MO) and an incubation time of 5 minutes, while for PKH26 and CellVue®claret, cells were stained with 3 µL of dye in 1 mL of Diluent C for 5 minutes of incubation.

We suspended the cells in 2 mL of media (per well in a 12-well plate) and started imaging immediately. In order to investigate the effect of cell density on the geometry of the final plexus, we performed 5 different assays with different cell densities. Cell densities below 50 cells/mm^2 did not form a network. Above 200 cells/mm^2, cells did not participate in network formation, and excessive cells aggregated and formed a clump. A density of 150 cells/mm^2 produced a uniformly connected network of cells.

2.2.3 Data acquisition

Since microvasculogenesis takes place over many hours, we collected data over 22 hours, at intervals of 15 to 60 minutes, using a long-term live-cell setup with an environmental chamber (Leica live-cell imaging system). We acquired phase-contrast and fluorescent images using a Leica DMI6000B inverted microscope equipped with a Qimaging Retiga 2000R digital camera and commercial image acquisition software InVitro (Media Cybernetics Inc). We used Matlab® (Ver. 7.4.0.287, MathWorks Inc.) software's image processing toolbox along with commercially available Image-Pro Plus (tracking module, Media Cybernetics Inc) to extract the morphological parameters of the cells at each time point.

2.2.4 Image segmentation

In order to differentiate neighboring cells from each other, we used three separate dyes: PKH67, PKH26, and CellVue®claret. Also, by defining the primary colors of PKH26 as red, PKH67 as green and CellVue®claret as blue, we produced three additional secondary colors by staining each cell population by two different dyes at a time (i.e. yellow, cyan and magenta in addition to red, green and blue). As an example of our image segmentation, we show in the segmentation process for an image acquired at t=180 min (Figure 2-4, b). First, we imported composite images of three fluorescent channels into MATLAB as 1200x1600x3 RGB image arrays. The three matrices consisted of the red, green, and blue components of the image. We used a background subtraction routine to compensate for the non-uniform illumination on the raw fluorescent images. After converting the image into equivalent arrays in HSB colorspace (Figure 2-4, c-e), the boundaries of the cells were determined primarily by the brightness matrix (Figure 2-4, e) and cells' color defined primarily by hue matrix (Figure 2-4, c). By defining equal intervals centered around the expected color (0-30& 330-360 red, 30-90 yellow,90-150 green, 150-210 cyan, 210-270 blue and 270-330 magenta), each pixel was assigned a color (Figure 2-4, f-k). Knowing the specific color for each pixel and having the network pattern as binary image (from brightness matrix), six channels were derived (Figure 2-4, l-q). Overlaying these 6 distinct channels produced the final segmented image (Figure 2-4, r).

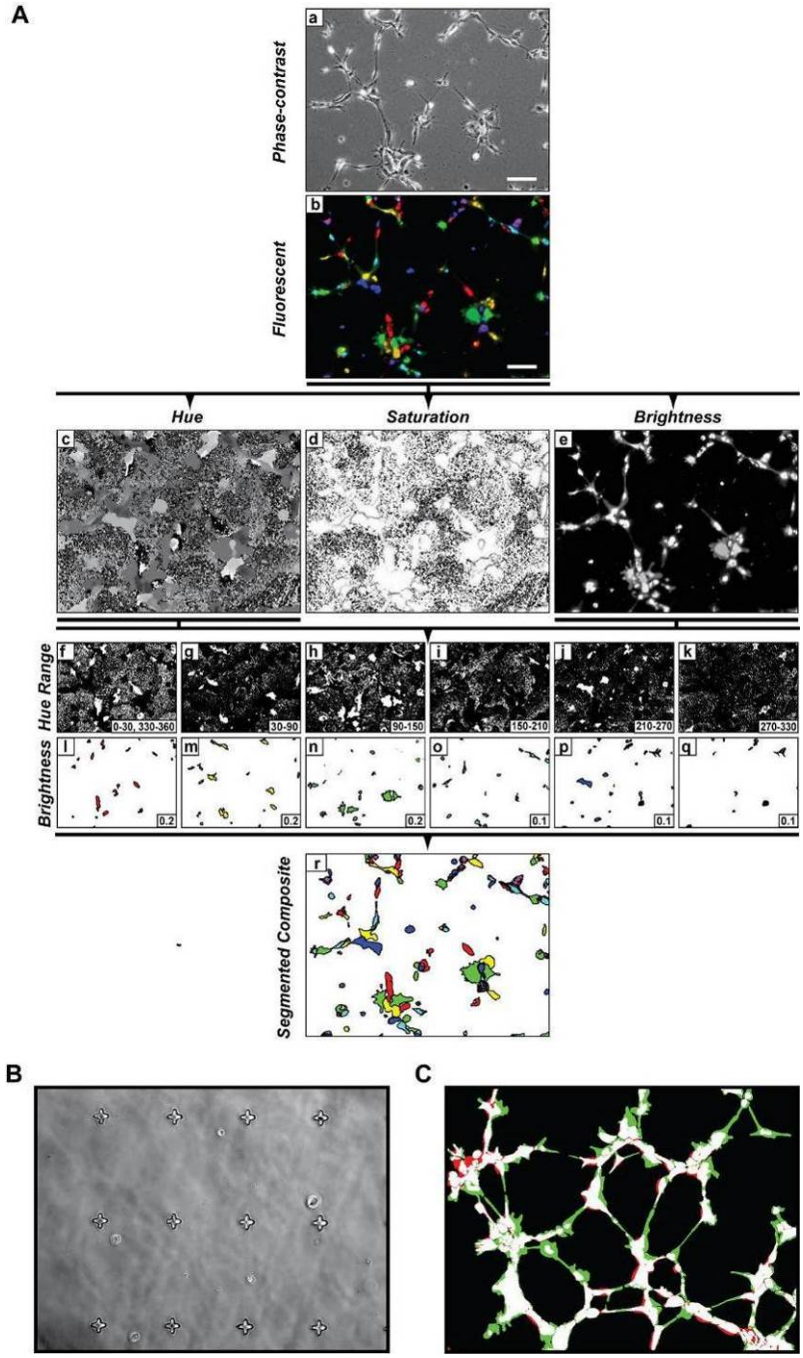

Figure 2-4: Data collection and image processing. (A) Flowchart of image processing algorithm. (a) Phase-contrast and (b) corresponding fluorescence images of HUVECs on Matrigel during microvasculogenesis. The fluorescence images were decomposed to (c) hue, (d) saturation, and (e) brightness. (f-k) Images of decomposed hue matrix based on equivalent intervals. (l-q) Images of decomposed color channels for red, yellow, green, cyan, blue and magenta. (r) Segmented composite image for t=180 min. Scale bar = 100 µm. **(B)** Phase-contrast image of fiducial markers, as described in Fig. 1A to correct for large-scale gel contraction or movement. **(C)** Example of segmented cells using automated algorithm vs. manual curation. White fill shows correctly segmented objects, while green fills show the mistakenly segmented and red fill shows mistakenly non-segmented objects

Since the automated process of segmentation described above was imperfect, we manually curated the images by comparing them with the phase-contrast images. In order to estimate the accuracy of the segmentation method above, we compared the segmented image (output of the algorithm) with the manually retouched image. As an example, Fig. S1C shows the comparison between an automatically segmented image and a manually curated segmented image. We found that the ratio of the cell area correctly segmented by the algorithm to the total cell area identified by manual curation was approximately 0.7 for all frames. Next, we tracked the paths of the cells over the course of the assay using the software ImagePro Analyzer (v.6.2.0.424, Media Cybernetics Inc.). We checked that all cells were tracked correctly, and in a small number of cases, we manually redefined the paths by comparing the segmented images with the phase-contrast images. With the paths of all cells located, we used the software ImagePro to measure all morphology and motility phenotypes (area, perimeter, box ratio, maximum radius, displacement, accumulative distance, displacement vector angle change, and even cell count).

We tracked four phenotypes that described cellular morphology: *area*, *perimeter*, *box ratio* (ratio of length and width of the smallest bounding rectangle of each cell, to indicate the extent to which the cell is elongated), and *maximum radius* (maximum distance between cell centroid and its boundary, to serve as a more sensitive measure of filopodia formation than box ratio), and another three phenotypes that described cellular motility: *displacement* (distance travelled relative to previous time point), *accumulative distance* (sum of displacements since t=0), and *displacement vector angle change* (direction of displacement). We also determined total *cell count* (which could change due to entrance and exit from the field of view; cell proliferation, as determined by new appearing cells that were not previously tracked, was small, accounting for <5% of cells).

Overall, we tracked the positions and morphologies of 125, 183, and 165 cells in datasets 1, 2, and 3, respectively, at 35 time points, and extracted the morphology and motility phenotypes (7 per cell) at 11 representative time points. This analysis produced a matrix of 36,421 array elements, where each element represented a quantifiable phenotype (either morphology or motility) for one cell at one time point. We obtained complete information (i.e. the cells were present in the field of view and were clearly segmented at all time-points) for 90, 112, and 132 cells, respectively, for the three data sets.

2.3 Results

We developed a method to track the positions and morphologies of individual primary human umbilical vein endothelial cells (HUVEC) during microvasculogenesis; this method used time-lapse live-cell fluorescence microscopy, followed by automated analysis and manual curation of images. Compared to other single-cell tracking studies [13, 14, 26], single-cell tracking for tissue morphogenesis posed a number of unique challenges).

2.3.1 Unique challenges in single-cell tracking of tissue morphogenesis

1) Hours-long imaging over cells on gels. The natural extracellular matrix for many tissues is soft gel rather than flat plastic surface. Over the time course of the experiment, our cell-seeded gels contracted ~200 μm vertically. To ensure collection of the clearest set of images, we molded the gel to create a flat surface to avoid blurring over a large field of view (here, a 1.2 by 0.9 mm field of view to capture sufficient numbers of cell for analysis), and manually focused the gel at each time point. 2) Accurate segmentation of cell-cell boundaries. Since tissue morphogenesis features a multitude of coordinated cell-cell contacts, cell-cell boundaries need to be carefully identified. We used intracellular dyes as a simple and effective method (another method being transfection) for tracking primary endothelial cells. To avoid photobleaching and

phototoxicity of the primary cells, we minimized the amount of dye and excitation volume while still acquiring sufficient signal. In addition, we used six different colors of dyes (three primary and three secondary by mixing the three primary-color dyes) to ensure that most cellular neighbors (more than 90%) will exhibit different colors. We used an automated algorithm for segmentation supplemented by manual curation for all cells (the algorithm was ~70% accurate, see Figure 2-4C). 3) Complexity of cellular behavior. Because of the plethora of cell-cell interactions (via paracrine factors, mechanotransduction, or direct contact), cellular migration follows a variety of complex trajectories, resulting in formation and breakage of cell-cell junctions. Hence, each cell needs to be carefully tracked (with new cells appearing and disappearing) from frame to frame. 4) Large data collection. To image processes that take place over tens of hours to single-cell resolution, we acquired 35 time points of wide-field data (requiring gigabytes of raw data) for each trial. While data collection and analysis at a systems level has been suggested for tissue morphogenesis (for example, our study corresponds to a 4-dimensional "xytp" experiment, where x and y denotes the planar dimensions, t denotes time and p denotes population), there have not been published studies, to our knowledge, for analyzing the formation of human tissue with single-cell resolution.

Traditionally, endothelial cells undergoing microvasculogenesis on Matrigel have been monitored using phase-contrast microscopy. Here, we tagged endothelial cells with different fluorescent dyes to enable single-cell tracking, such that the morphology and motility of each cell over every time point could be mapped into a numerical array. Analysis of this dataset revealed the collective behavior of all endothelial cells (i.e. at a population level) over time, as well as the variations in behaviors of each individual endothelial cell over time.

2.3.2 Multispectral fluorescence microscopy enables accurate single-cell tracking

Compared to phase-contrast imaging of CLS structures, we found that multispectral fluorescence imaging clearly delineated individual cell boundaries, even in dense cell clusters (Figure 2-5). We tracked four phenotypes that described cellular morphology: *area, perimeter, box ratio* (ratio of length and width of the smallest bounding rectangle of each cell, to indicate the extent to which the cell is elongated), and *maximum radius* (maximum distance between cell centroid and its boundary, to serve as a more sensitive measure of filopodia formation than box ratio). Cell morphology has been demonstrated to be a sensitive indicator for interactions by endothelial cells with the extracellular environment. For example, changes in the morphology of individual ECs are dramatically more sensitive to hypoxia than cell number or other common indicators of blood vessel phenotype [27, 28]. The specific parameters we use to measure cell morphology have also been used to characterize other cell types (e.g. area and box ratio for keratocytes) [29, 30].

We also tracked another three phenotypes that described cellular motility: *displacement* (distance travelled relative to previous time point), *accumulative distance* (sum of displacements since t=0), and *displacement vector angle change* (direction of displacement). Previous studies have established the importance of migration of endothelial cells in microvasculogenesis [31, 32].

Overall, we tracked 125, 183, and 165 cells (in three data sets) at 35 time points, and analyzed images from 11 time points (starting at t=0 and analyzing the image every 60 minutes afterwards). This analysis produced a matrix of 36,421 array elements, where each element represented a quantifiable phenotype for one cell at one time point.

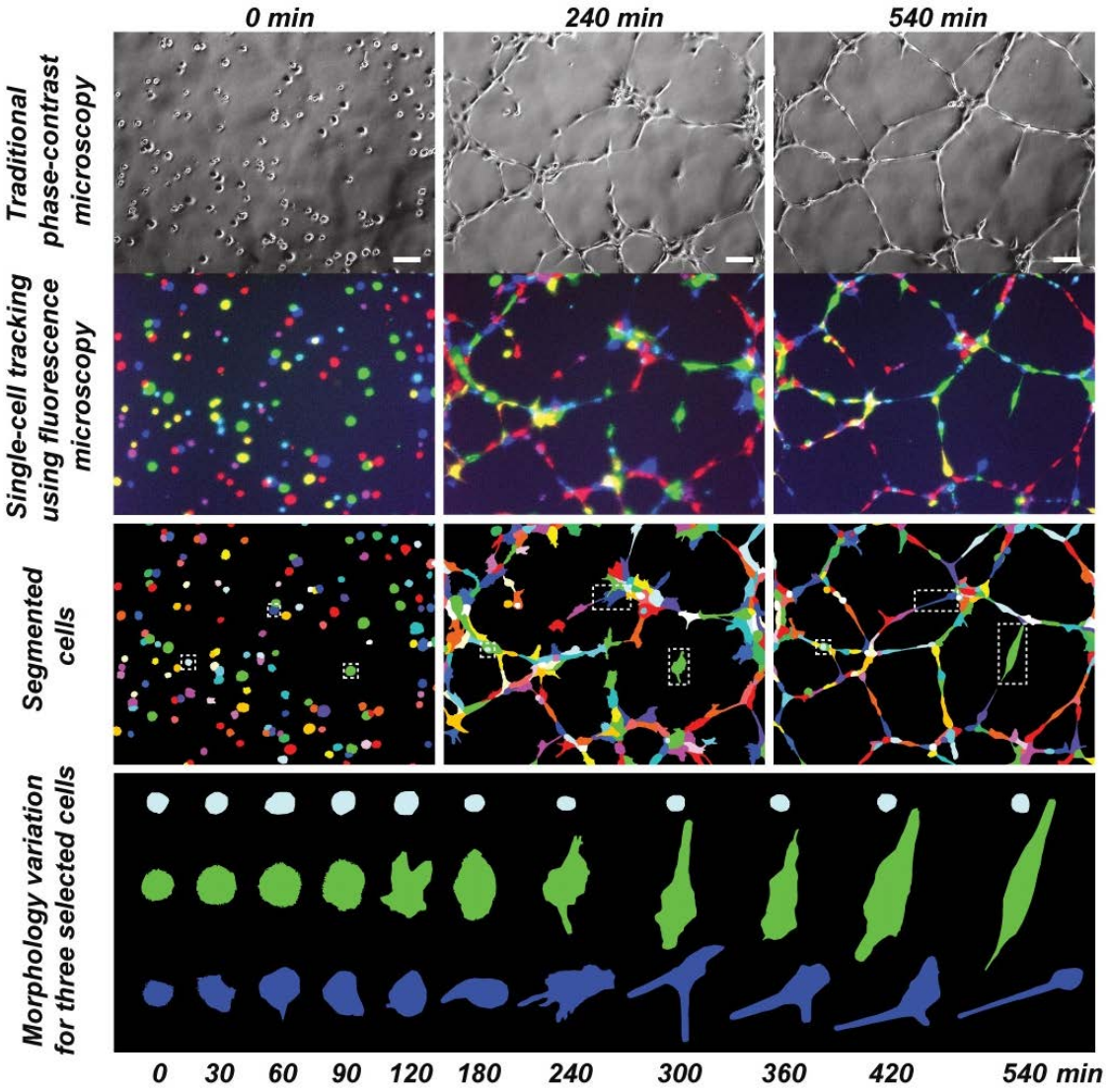

Figure 2-5: Imaging of microvasculogenesis. From top to bottom: (i) Time-lapse microscopy using conventional phase-contrast imaging. Scale bar = 100 µm. (ii) Corresponding time-lapse images of primary endothelial cells tagged with different fluorescent dyes such that individual cells and cell-boundaries could be discerned. Movies of the process are provided in Supporting Data (Movies S1 to S3). (iii) Segmented images of the fluorescence data set. (iv) Tracking of morphologies of three cells over the time course of the assay

2.3.3 Microvasculogenesis occurs in five distinct and reproducible phases according to quantitative analysis of collective multicellular behavior

While formation of CLS has been visualized qualitatively using methods such as phase-contrast microscopy, we hypothesized that quantitative analysis of the phenotypes could yield a more precise description of microvasculogenesis. Analysis of the progression of phenotypes revealed a carefully orchestrated series of events that has thus far not been discovered (Figure

2-6 shows four key parameters in normalized units, or N.U.: Normalized unites of zero and one corresponded to the lowest and highest values, respectively, attained by each parameter over all time points.

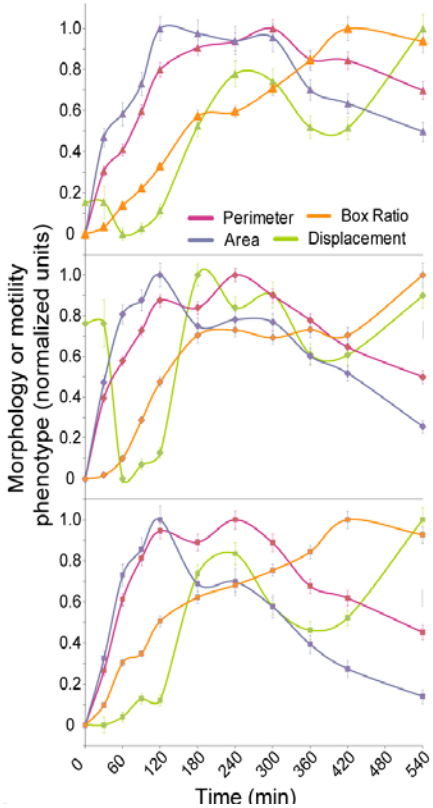

Figure 2-6: Dynamics of morphological and motility phenotypes during microvasculogenesis. Normalized population-averaged parameters for perimeter (red), box ratio (orange), area (purple), and displacement (green). Normalized units of zero and one corresponded to the lowest and highest values, respectively, attained by each parameter over all time points. The standard error is indicated for each data point (for n = 90, 112 and 132 cells which stayed in the field of view for the entire assay, respectively, for the three data sets

For the three data sets (top, middle, bottom), zero and one normalized units correspond to: 11 to 28, 9 to 26, and 13 to 23 µm (displacement); 103 to 189, 108 to 203, and 103 to 213 µm (perimeter), 738 to 1766, 666 to 1701, and 766 µm2 to 1849 µm2 (area), 1.29 to 2.44, 1.28 to 2.8, and 1.31 to 2.50 (box ratio)). While these trends were not obvious from visualization of the phase-contrast movies, they were reproducible among the three independent trials based on quantitative analysis (Figure 2-6).

Then, we asked what minimum number of cells is required to represent the behaviors of the full population. We randomly chose n cells and calculated the averaged behavior of these n cells for all time points (n-cell-average: n varies between 1 and 132). We then calculated the percentage error between the n-cell average and the population average. We repeated the process for four different groups of randomly chosen cells. The percentage error was less than 10% in all cases for n=40 cells.

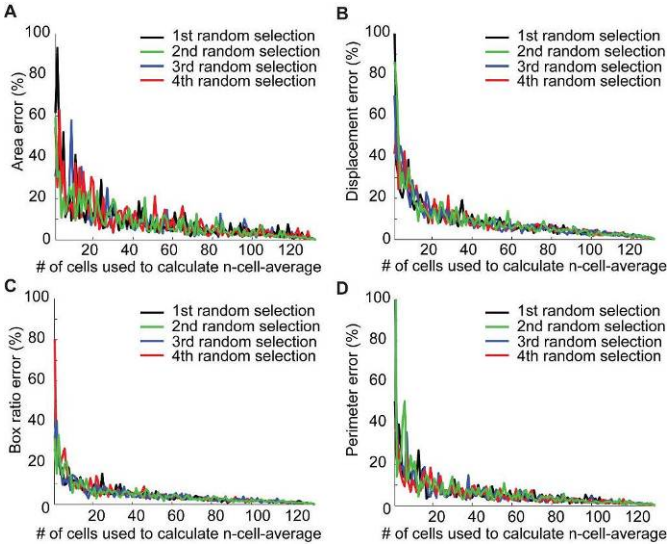

Figure 2-7: Deviation of n-cell-averaged behavior from population-averaged behavior. These plots show the error percentage of n-cell-average for **(A)** Area, **(B)** Displacement, **(C)** Box ratio, and **(D)** Perimeter.

Next, we investigated whether each dye produced different cell behavior. We plotted morphological and motility parameters for each staining group of red, green, blue, yellow, cyan and magenta (Figure 2-8 shows the case of perimeter). For none of the 3 data sets did any dye (~20 cells/each group) cause significant behavioral differences.

The following five phases of microvasculogenesis were identified from changes in slopes of the phenotypes when plotted against time (Figure 2-9). 1) Rearrangement and aggregation. Over this first phase, which lasted ~60 minutes, HUVECs migrated to attain spatial positions favorable for cell-cell networking. Cell displacement ranged from low (~0 N.U.) to high (~0.8

N.U.). As cells migrated, they also spread, leading to increases in cell area (from ~0 to 0.7 N.U.) and perimeter (from ~0 to 0.5 N.U.), while maintaining relatively round shapes (box ratio from ~0 to 0.2 N.U.). 2) Spreading. Over the second phase, which lasted for another ~60 minutes, cells stayed in similar positions but spread: displacement remained close to 0 N.U., while surface area, perimeter and box ratio increased constantly (from ~0.7 to 1 N.U., from ~0.5 to 0.9 N.U., and from ~0.2 to 0.5 N.U., respectively). 3) Elongation and formation of cell-cell contacts. The third phase lasted for ~2 hours. Interestingly, although cells were elongating, cell area decreased slightly. An increase in cell displacement (from ~0.1 to 0.8 N.U.) coupled with decrease in cell area (from ~1.0 to 0.8 N.U.) resulted in elongated protrusions, as illustrated by an increase in box ratio (from ~0.45 to 0.7 N.U.). 4) Plexus stabilization. In the fourth phase, area and perimeter decreased (from ~0.8 to 0.5 N.U., from ~1.0 to 0.75 N.U., respectively), consistent with an increase of thickness of cells (assuming no large changes in cell volumes; an increase in cell thickness was also confirmed by confocal imaging). The box ratio increased only slightly (from ~0.75 to 0.9 N.U.). Decrease in cell displacement (from ~0.85 to 0.6 N.U.) reflected stabilization of the plexus. 5) Plexus reorganization. After the initial structure of the plexus took shape, displacement exhibited a sharp increase to its maximum (1 N.U.), whereas perimeter and area decreased gradually. These changes reflected a re-organization of polygonal structures in the vascular plexus, and continued until the end of the assay. (Over extended periods of time, regression of the plexus is known to occur.)

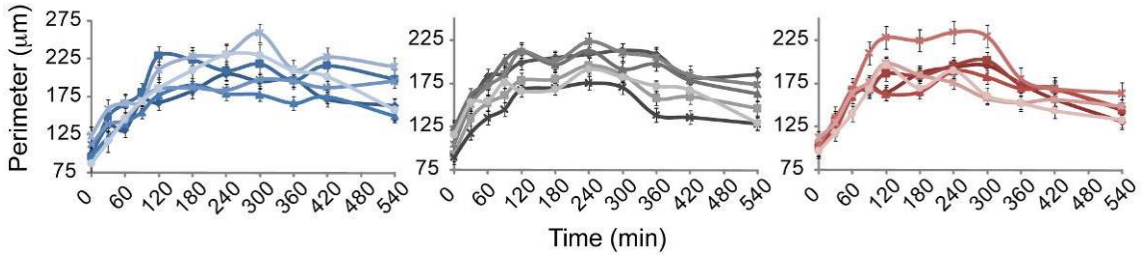

Figure 2-8: Staining group comparison for triplicate data. Morphological parameters for 6 groups of cells stained with 6 different fluorescent dyes for each data set (blue, black and red indicate first, second and third dataset respectively; perimeter is chosen for illustration purpose).

These population-level trends were quantitatively reproducible among the three independent trials.

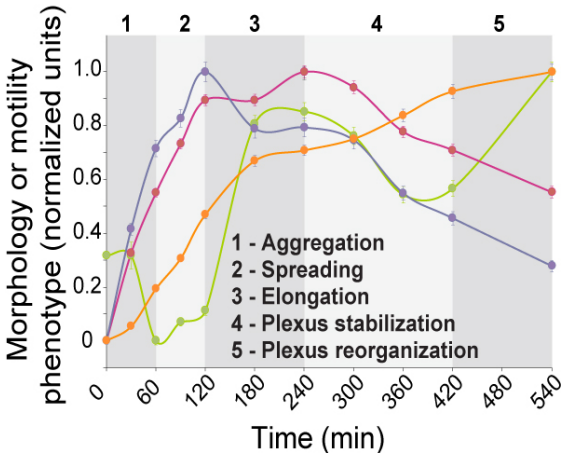

Figure 2-9: Dynamics of morphological and motility phenotypes during microvasculogenesis, based on averages across cell population. Averages of population-averaged phenotypes across three data sets, with the five distinct temporal phases (as identified by visual inspection of changes in the slopes of phenotypes) shaded in white and gray.

Based on these quantitative data we propose a model for CLS under the specific conditions of this experimental setup.

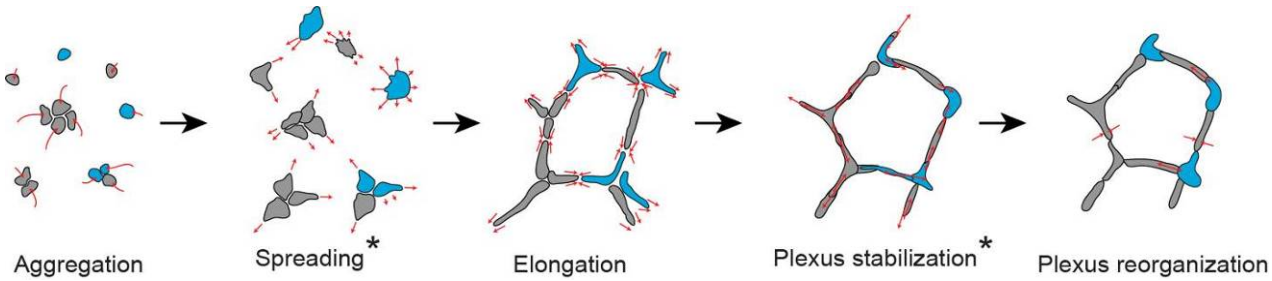

Figure 2-10: Schematic model of CLS formation. Red arrows show the distinct feature of the population behavior at each phase (e.g. aggregation in first phase). Light blue cells show a subpopulation of cells that form the nodes. Previously unidentified phases for microvasculogenesis are shown with asteriks.

2.4 Discussion

2.4.1 Mechanism of microvasculogenesis

In our initial application of this method to studying the mechanism of microvasculogenesis, this method has provided, at the population level, additional granularity about how a system of endothelial cells form microvessels [33]. For example, our observed sequence of events agrees with previous studies in which endothelial cells exhibited significant displacement before starting to elongate [24, 25]; in an *in vivo* study, endothelial cells also migrated into distinct spatial regions before undergoing morphological changes and vascular development [33]. Our analysis is also consistent with studies that identified a period where the vascular plexus underwent a slight deformation after formation [24]. On the other hand, the second observed phase of cell spreading (where the cells spread while exhibiting minimal movement, presumably forming filopodia and lamellipodia, before elongating to form cell-cell contacts) and the forth observed phase of plexus stabilization (a distinct period where the plexus stabilizes before it rearranges) have not been identified as discrete events to our knowledge [24, 25, 34, 35]. Moreover, not we can answer to the questions that we posed previously; we can say that this process is not random at all, although the structure of final plexus might imply so.

This high-resolution decomposition of phases could be useful for identifying unestablished mechanisms of key growth factors and angiogenic modulating drugs (such as VEGF and VEGF inhibitors). It may also facilitate the discovery of new clinically useful angiogenic modulatory agents (both pro- and anti-) since the effect on each specific phase could be differentially measured using the time-lapse imaging.

2.5 Conclusion

We have presented a method that tracks the morphologies and motilities of individual cells during the time course of forming a tissue on a three-dimensional gel. As a first biological system, we applied this method to studying how a community of endothelial cells forms the initial patterns of microvessels. At the population level, this method quantified how a system of cells evolves collectively over time, and led to the identification of previously unobserved phases.

Chapter 3 Uncovering the behaviors of individual cells within a multicellular microvascular community

3.1 Introduction

Variations in the behaviors of individual cells during the morphogenesis of human tissues are likely to be important in shaping the evolution of multicellular structures [36]. Knowledge of how individual cells behave and self-organize in native systems are also important in the design of synthetic systems, such as engineered tissues [36] and complex multicellular communities [10, 37]. By contrast, population-averaged measurements, while widely used, are the end results of a large number of possible underlying statistical distributions, and mask critical cell-to-cell variations [38]. For example, the same population-averaged measurement could reflect all cells behaving close to the average, or the sum of many unique cellular behaviors. For the morphogenesis of a human tissue, the extent of cell-to-cell variations has thus far not been systematically studied, and is currently largely unknown. In this chapter based on the methodology developed in previous section, we will study the motility and morphology patterns of individual cells and try to understand the functional significance of these patterns.

3.2 Methods

3.2.1 Clustering algorithm

To compare the trends of how phenotypes varied for different cells, we used a correlation clustering algorithm based on pairwise comparisons [39]. First, we identified a correlation in the behaviors of two cells if the Pearson's correlation coefficient between the two sets of data (with each set of data consisting of the phenotype values at different time points) exceeded 0.6 (Figure

3-1A). We represented the pairwise relations of cells in a graph G(V,E), in which the vertices (V) represented cells and edges(E) the existence of a correlation between two cells. The initial assignments of correlations for an illustrative example of 15 cells is shown in Figure 3-1B. Next, the goal was to identify clusters in which most pairwise vertices are connected (i.e. to transform the graph G(V,E) into a disjoint union of cliques by addition and deletion of minimum number of edges), adapting previous correlation clustering algorithms [40]. We postulated that two cells, even if their phenotype variations did not show a correlation coefficient above 0.6, could be correlated if they shared a large number of connected cells. For each pair of cells, we computed the number of such common neighbors (CN), as well as the number of uncommon neighbors (UN). Defining the index CRIT as CRIT=CN-UN, we added an edge for the vertex pair which was not already connected with the highest CRIT (e.g. vertex pair (4,6) in Figure 3-1B, initial step), and deleted an edge for the vertex pair which was connected with the lowest CRIT (e.g. vertex pair (1,15) in Figure 3-1B, initial step). In cases where m (out of n total) vertices formed a completely connected graph (i.e. via m(m-1)/2 edges), all m vertices were allocated to a cluster (e.g. vertices 1,4,6,11 in Figure 3-1B, second step). Considering the remaining cells in the graph, we repeated the sorting of CRIT values, addition and deletion of edges, and cluster extraction. This cycle was repeated in as many steps as needed until all vertices were extracted into clusters (in the example shown in Figure 3-1B, four cycles were needed, to produce clusters of <3>, 2,12 <10,13>, <7,9> 1,4,6,11 and <5,8,14,15>). We performed this clustering procedure on the third data set, which contained the highest number of cells (132 cells) with complete tracking information over the time course of formation of CLS.

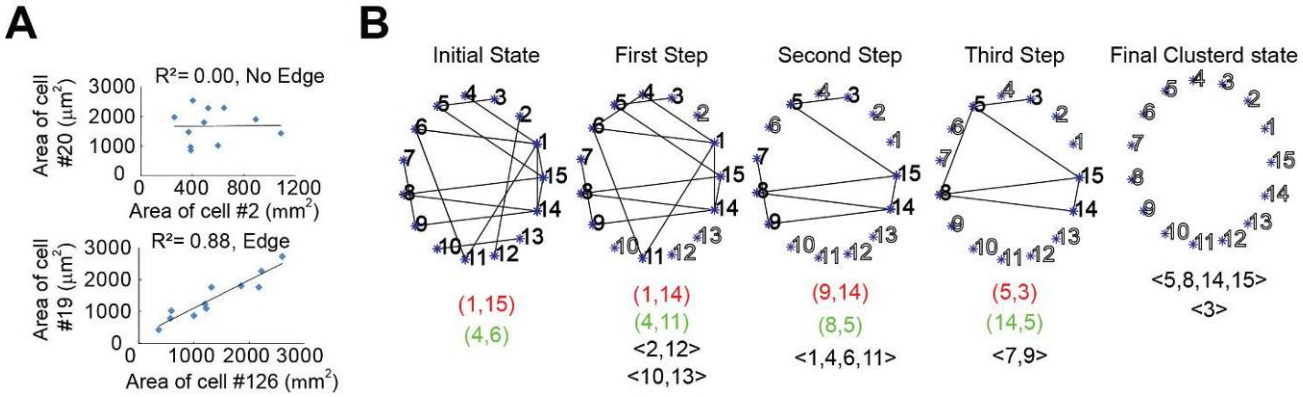

Figure 3-1: Clustering of cells with similar temporal variations in phenotypes. (A) Pairwise correlation coefficients determination **(B)** Clustering algorithm: Each graph shows the cells which are not clustered yet and their relative relation. (u,v) in red shows deleted pairs, (u,v) in green shows added pair, and <u,v,w> shows extracted clusters.

3.2.2 Initial inhibition of nonmuscle myosin II

We treated a group of ECs with 50 µM of blebbistatin (Sigma) and 60 µM of ROCK inhibitor Y-27632 (Sigma) for 1.5 hours, and changed the media to regular growth media. To assess the effectiveness of the drugs in inhibition of stress fiber formation, we conducted a standard assay [41] of fixing and staining treated cells for actin (phalloidin, Invitrogen) at different times (t=0,2,4,8,16 hours) after media change and measured the intensity of F-actin; the data showed loss of stress fiber and cell detachment over time, consistent with previous studies that showed these drugs to be effective hours after initial treatment before losing their effect .

We repeated Matrigel CLS formation assay with a 50:50 mixture of untreated cells and cells treated with nonmuscle myosin II inhibitors. The 50:50 mixture allowed us to study the behaviors of untreated cells and drug-treated cells side by side in the same experiment [42].

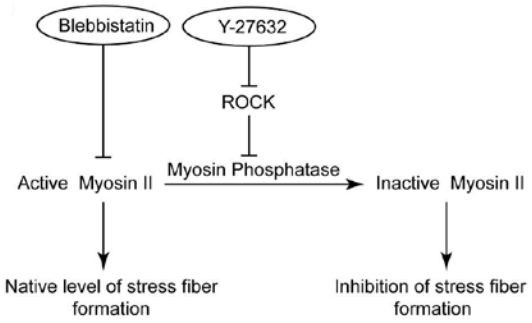

Figure 3-2: Schematic diagram of stress-fiber formation inhibition. direct inhibition (via blebbistatin) or through ROCK inhibition (via Y-27632).

3.2.3 Classification of cells as nodes or branches

In order to determine the positions of nodes on the CLS, we created an image skeleton of the CLS (Matlab® Image processing toolbox, Ver. 7.4.0.287, Mathworks Inc.). We then placed a representative circular cell (with an average cell area corresponding to what is observed) on each branching point. The cells which partly or totally overlapped with the representative circular cells were classified as nodes, whereas the ones which did not overlap were classified as branches (Figure 3-8A).

3.3 Results

3.3.1 Behaviors of most endothelial cells follow a handful of unique patterns

While useful, such dynamic bulk averages (reflecting the evolution of the multicellular population) can arise from a myriad of underlying distributions of individual cellular behaviors [38]. We examined next whether there existed subgroups of endothelial cells that exhibited similar behavioral dynamics, and how closely correlated such dynamics are to the population averages. We used a correlation clustering algorithm which determines membership in a cluster based on pairwise comparisons [43]; here, cells can be represented as vertices on a graph, with correlations (i.e. if Pearson's correlation coefficient of the phenotype values at different time

points for the first cell vs. those for the second cell exceeded 0.6) represented as edges (Figure 3-1).

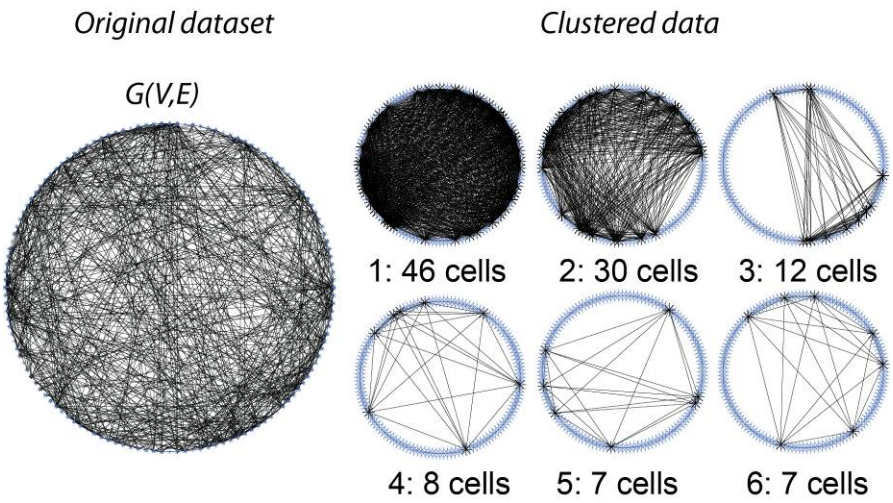

Figure 3-3: Clustering of cells with similar temporal variations in phenotypes. Unclustered and clustered graphical representations of the third dataset (with the corresponding number of cells) according to cell area.

We identified multiple dominant patterns of dynamic behavior for each phenotype, which were reproducible across different independent datasets. To investigate the reproducibility of the phenotype dynamics, we determined the cell clusters for all four phenotypes (displacement clusters shown in Figure 3-4) across three separate datasets (each dataset containing more than 100 cells). Remarkably, all independent datasets showed cell clusters with very similar dynamic patterns. Depending on the dataset, the cell counts in each cluster slightly varied. We could group ~60 to 70% of cells into only three distinct clusters of dynamic behavior with respect to cell area (Figure 3-5). Similarly, analysis of three other phenotypes (displacement, box ratio, and perimeter) also grouped 60 to 70% of cells into three major clusters of phenotypic behavior (Figure 3-4).

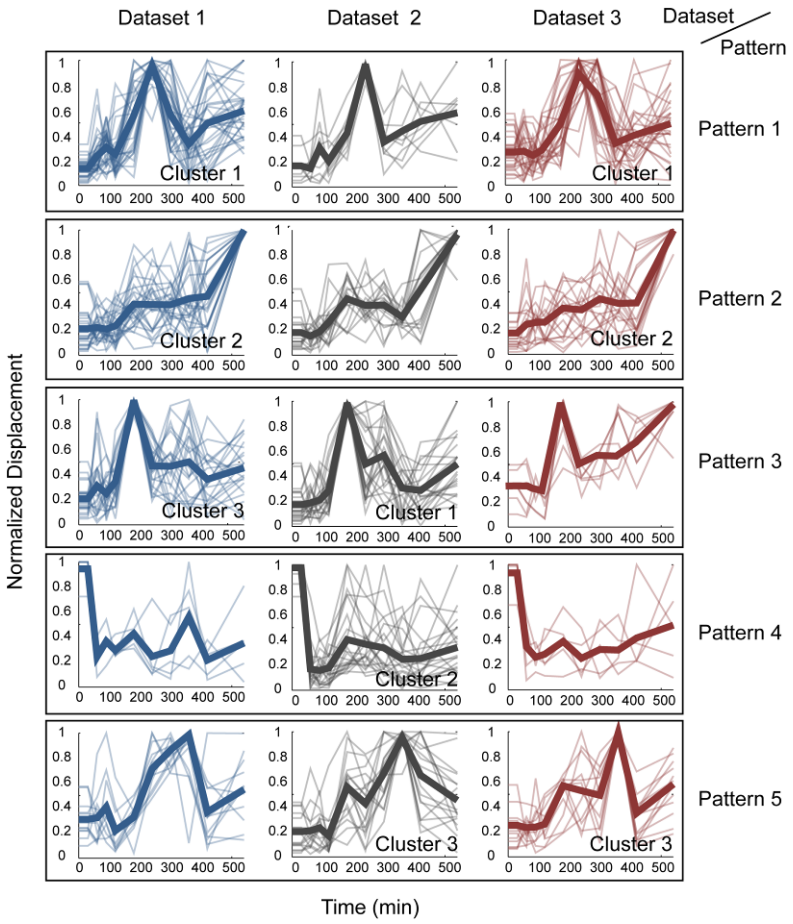

Figure 3-4: Five very similar patterns of displacement dynamics (clusters 1 to 5) were identified using an objective algorithm from three independent datasets. Pattern 1: Displacement peaks at t=240 min. Pattern 2: Displacement increases monotonously. Pattern 3: Displacement peaks at t=180 min. Pattern 4: Displacement has the maximum value at t=0 and decreases rapidly at t=30 min and keeps its minimum value for the rest of the assay. Pattern 5: Displacement peaks at t=360 min. For each dataset, the cluster numbering starts with the highest populated cluster (i.e. Cluster 1).

We could also identify four "classes" of morphological behaviors, where each class exhibited the same dynamic behaviors in *both* degree of cell spreading (cell area) and branching morphology (box ratio). The four classes represented the behaviors of over half (51%) of the cell population (Figure 3-5). Hence, considering a single phenotype, the dynamic behaviors of most endothelial cells followed a small number of distinct patterns. However, if we consider multiple phenotypes the whole cell population does not fall into handful of distinct classes

(Figure 3-5B). This has been shown previously shown for other cell types (fish Keratocytes) [30].

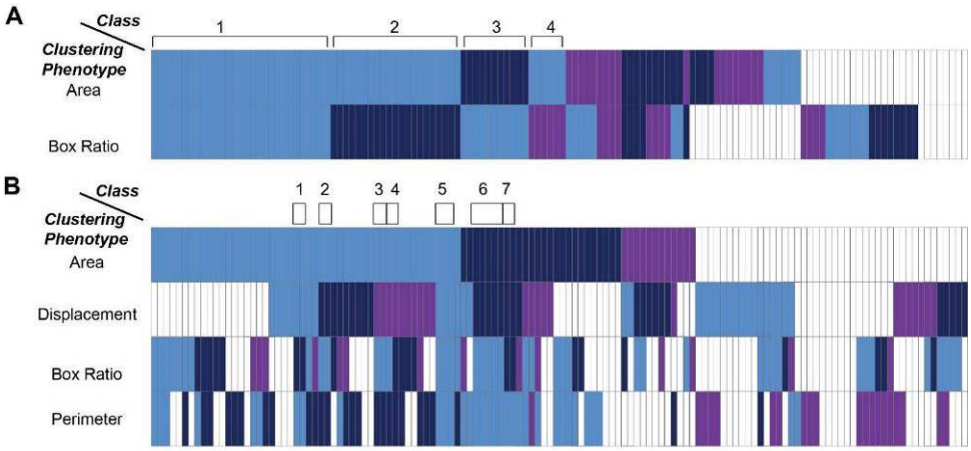

Figure 3-5: Classification of cells with similar temporal variations in phenotypes. (A) Grouping of cells, as represented by columns, into "classes", defined as groups of cells that exhibited a similar combination of 2 morphological clusters (area and box ratio). Cell area and box ratios are the most commonly used metrics to measure the degree of cell spreading and the branching of cell morphology, respectively. A class was identified if all cells shared an identical combination of 2 phenotypic clusters and only if the class contained at least 3 cells. Six "classes" were identified, with the 4 most populated classes (with 29, 21, 11 and 6 cells) comprising 65% of the cells. For each phenotype, the most to least populated clusters were colored light blue, dark blue, and purple (with white indicating unclustered cells). **(B)** Grouping of cells, as represented by columns, into "classes", defined as groups of cells that exhibited a similar combination of 4 phenotypic clusters (area, distance, perimeter and box ratio). A class was defined if all cells shared an identical combination of 4 phenotypic clusters and only if the class contained at least 2 cells, or 1.5% of the population. Seven "classes" were identified comprising only 13% of the population. For each phenotype, the most to least populated clusters were colored light blue, dark blue, and purple (with white indicating unclustered cells).

3.3.2 Population-averaged measurements mask the trends of most individual endothelial cells

Previous studies have suggested that population averages of biological properties could result from a myriad of underlying statistical distributions. To assess how closely the behaviors of subpopulations of cells correlated to the population averages, we compared the averages of all cells, of the three most populated cell clusters, and of cells that were not clustered, for each of the four phenotypes (Figure 3-6). Analysis of correlation coefficients showed that for each of the four phenotypes, the population average correlated most strongly to the highest populated cluster. The population averages, however, did not correlate to the averages of the second

highest populated clusters any more strongly than to those of unclustered cells, and in fact were less correlated to the averages of the third highest populated clusters than to those of unclustered cells. Hence, the relative trends of the population averages were dominated by the behavior of only ~30 to 40% of cells, and masked the behaviors of most cells in the population during tissue morphogenesis.

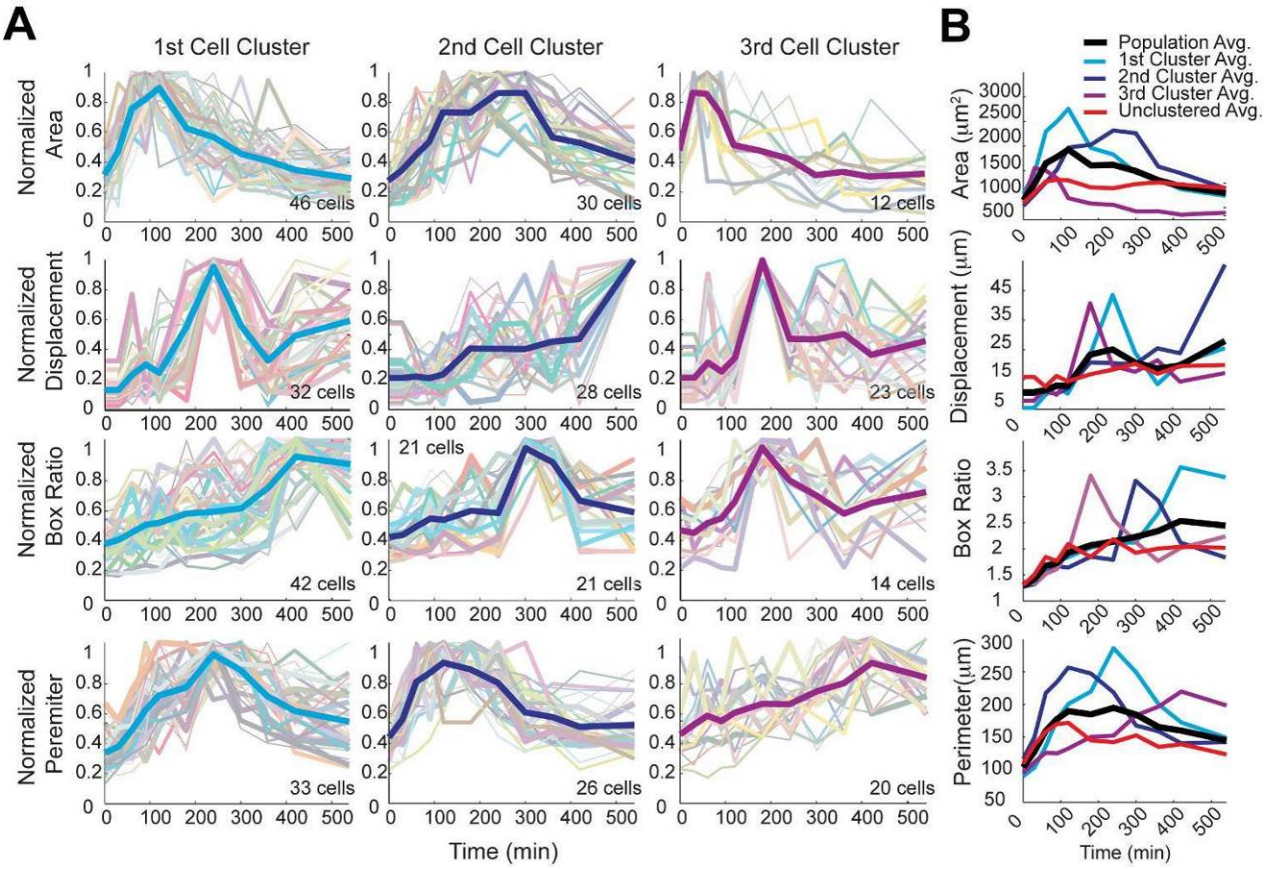

Figure 3-6: Behaviors of cell clusters relative to the population-averaged behavior. (A) Graphs showing temporal variations of normalized values of four phenotypes as exhibited by the three most abundantly populated cell clusters. Within each cluster, colored lines show the temporal variations of all individual cells that contribute to the cluster average (thick colored lines, with the most to least abundant clusters indicated by light blue, dark blue, and purple). Note that the compositions of cells in the three clusters are different across the four phenotypes. **(B)** Graphs showing temporal variations of the absolute values of four phenotypes. For each parameter, shown are population averages (thick black lines) and the averages of the three most populated clusters (thick colored lines). Note that the compositions of cells in the three clusters are different across the four phenotypes.

3.3.3 Cells in superficially similar microenvironments diverge in behaviors and fates

To interpret the significance of such dynamic patterns, we tracked the behaviors of these cell clusters in the movies over the time course of tissue morphogenesis. Through segmentation of images where cells were false-colored according to their cluster membership (Figure 3-7), the images showed how individual HUVECs, while appearing to reside initially in superficially similar microenvironments, diverged into distinct temporal patterns of cellular behaviors. The first and third most populated cell clusters, for example, all spread quickly but then shrunk in size; ultimately, in the final plexus structure, they assumed the structural role of connection points (nodes) for multiple CLS ((Figure 3-7). By contrast, cells in the second most populated cluster, which were generally the mid-range size cells in their immediate vicinity, typically formed the branches in the final plexus structure.

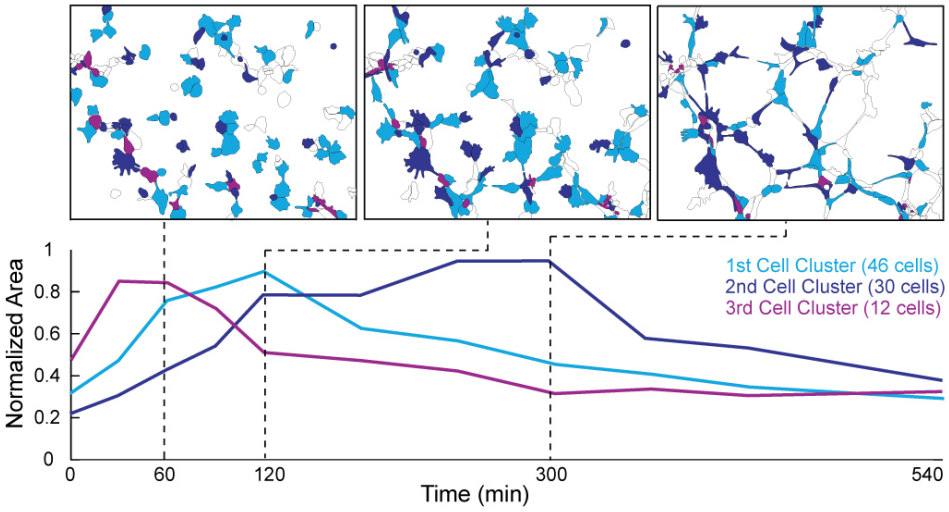

Figure 3-7: Clustering of cells with similar temporal variations in phenotypes. Segmented time-lapse images with cells false-colored according to their cell-area cluster (with three clusters of cells shown in purple, light blue and dark blue, and unclustered cells shown in white). The graph below shows the temporal progression of the cell areas for the three most abundant clusters, peaking at 60, 120 and 300 min, respectively.

We further characterized the relationship between the behavioral dynamics of each cell and their structural role in the CLS. We classified all endothelial cells in the final plexus structure as either nodes (38% of cells) or branches (62% of cells) (Figure 3-8A). The strongest correlation

was observed when clustered by changes in displacement. Here, 67% of the cells in the first cluster (whose displacements peaked at around *t*=240 min) formed nodes (Figure 3-8B); hence, the migratory dynamics of subpopulations of cells could be correlated to their structural role in the final plexus.

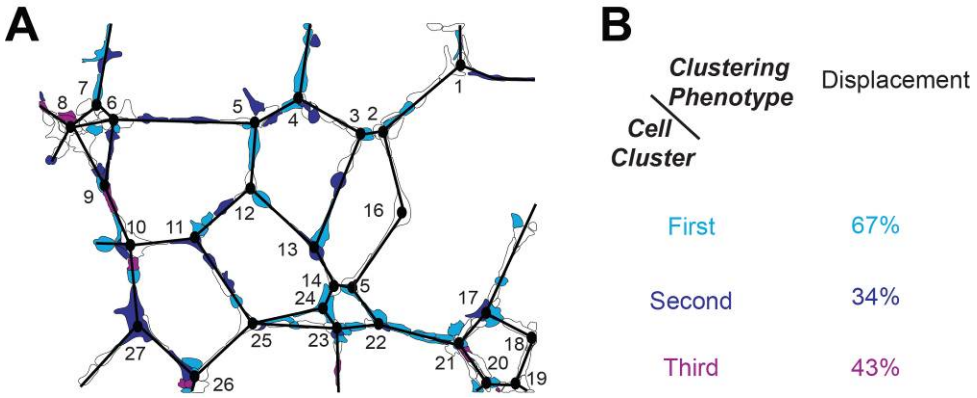

Figure 3-8: Correlation of migratory dynamics to structural role in final plexus. (A) Image of plexus at *t=540 min*, with cells at nodes and branches indicated. Black lines indicate branches and red circles the nodes. **(B)** Percentage of cells in each cluster forming node cells in the final plexus (%).

3.3.4 Initial inhibition of myosin II changed subsequent displacement dynamics and fates

In addition to the internal cytoskeletal machinery [44], endothelial cells can make use of other motility mechanisms such as coordinated movement through neighboring cells [45, 46]. We investigated whether individual cells can be biased towards one set of behavioral dynamics versus another set by initially limiting the role of active cytoskeletal machinery. We mixed together a population of untreated endothelial cells with endothelial cells whose ability to form stress fibers and/or focal adhesions was initially disrupted (via direct inhibition of active myosin II via blebbistatin as well as inhibition of ROCK via Y-27632). As observed previously [47], the drug-treated cells could still change cell shape by forming filopodia and lamellopodia. Like the native population (Figure 3-6A), a cell cluster emerged with a displacement curve peaks at around *t*=240 min (Figure 3-9, left). Interestingly, in this 50:50 mixture of drug-treated and

untreated cells, most cells in this cluster were drug-treated, and most cells with this migratory dynamics (~80% in this case) again formed nodes in the final plexus, just like the native population. We note that cell-cell connections were beginning to be formed already when these cells began migrating (i.e. displacement is increasing during the "elongation" phase identified from Figure 3-9); hence, coordinated movement was an available option for these cells. By contrast, another highly populated cell cluster that migrated quickly in the initial minutes consisted mainly of untreated cells, and subsequently formed mostly branch structures.

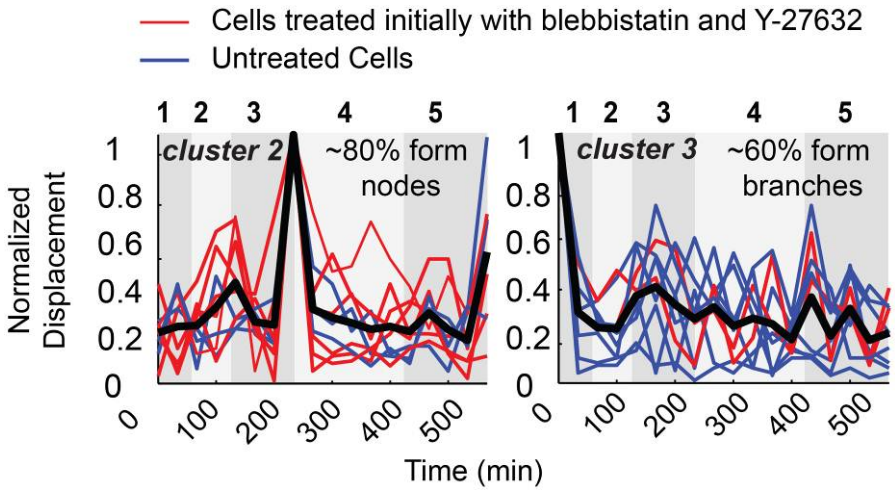

Figure 3-9: Correlation of migratory dynamics to structural role in final plexus. In a 50:50 mixture of untreated cells and cells treated with myosin II inhibitors, the second-most populated cell cluster (left subfigure, of which 70% were drug-treated cells) showed maximum displacement at t=240 min, with most of these cells forming nodes. The third most populated cluster (right subfigure, of which 75% were untreated cells) showed maximum displacement at t=0 min, with most of these cells forming branch structures.

3.3.5 Cellular behavior can exhibit large variations with different types of distributions

The variations observed for some phenotypes (which ranged from 20 and 120% relative to mean values, Figure 3-10A) are higher than those observed in other biological processes, such as gene expression (which exhibited up to ~60% variation relative to average population behavior [48]). This comparison possibly reflects the complexity of cell-cell interactions and the diversity of phenotypic behaviors needed to form a multicellular tissue. The extent of variations also

fluctuated over time: over the first phase of microvasculogenesis (aggregation), variations in displacement were large but rapidly decreased, as most HUVECs settled into position for cell-cell networking. For other phenotypes (such as box ratio and perimeter), initial fluctuations among the cell population were relatively small, but increased over the ~60 minutes of the aggregation phase.

Different underlying distributions of phenotypes can give rise to the observed variability. We plotted how two different phenotypes describing cell morphology were distributed across the population. For example, histograms enumerating cells with different cell areas showed that the endothelial cells tended to spread over time and then retract, maintaining either relatively unimodal or uniform distributions at all times (Figure 3-10C, left). By contrast, histograms of box ratio values showed initially Poisson-type distribution, then relatively uniform distribution at t=120 min, and finally bimodal distribution at the end of the assay (Figure 3-10C, right). Although both phenotypes were derived from cellular morphology, they exhibited different statistical distributions throughout the time course.

Studies on other cell types have indicated that individual cellular variability over time is often less than the variability in the population [30]. To examine how much a given cell varies during the process of microvasculogenesis, we examined the variability of individual cell areas across all time points (Figure 3-6B). We found that for cell area, most cells varied less over time than the population variability. (We obtained similar results for perimeter and displacement.) We also observed that some cells tend to exhibit very similar behavior over all time points (e.g. cell #104 exhibiting a small cell area), others vary within a range, whereas others adopt entirely different sets of behavior (e.g. cell #126 being quite round or very elongated) depending on the stage of microvasculogenesis (Figure 3-10D). These trends reflect the different types of

variability that can take place, as some cells exhibited changes within a range of bounded values, whereas others transitioned among different states altogether.

Finally, we note that the trends of the population averages were dominated by the behavior of only ~30 to 40% of cells, and masked the behaviors of most cells in the population (Fig. 2-6).

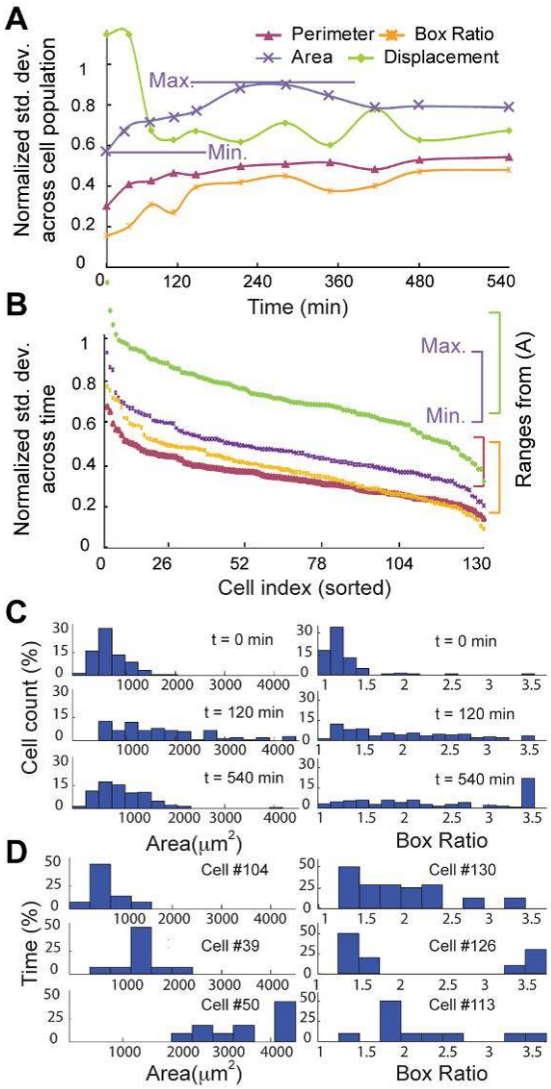

Figure 3-10: Variations in behavior from cell to cell. (A) Normalized standard deviations across the cellular population for perimeter (red), box ratio (orange), area (purple), and displacement (green), at a given time point. The plot shows the degree of variability of each phenotype across the cellular population at different time points. **(B)** Histograms of percentage of cells vs. value of phenotype (cell area and box ratio) at three different time points. Although both phenotypes were derived from cellular morphology, they exhibited different statistical distributions throughout the time course. **(C)** Normalized standard deviations of cell perimeter (red), box ratio (orange), area (purple), and displacement (green) for a given cell across all time points. The plot shows how much a given cell varies during the process of microvasculogenesis. For comparison, square brackets indicate the range of variability for a cell population at a fixed time (for the indicated parameter as obtained from part A). **(D)** Percentage of time

points within indicated values of cell area or box ratio, for three different cells that represented a range of distributions observed. A single cell can exhibit very similar behavior over all time points (e.g. cell #104 exhibiting a small cell area), or adopt two sets of very different behavior (e.g. cell #126 being quite round or very elongated). **(E)** Normalized standard deviations of how a given cell varies in box ratio, perimeter, and displacement across all time points. The gray zone indicates the range of variability for the cell population at a fixed time (obtained from part A).

3.4 Discussion

3.4.1 Mechanism of microvasculogenesis

This study also provided quantitative details on how *individual* endothelial cells vary from one another in behavior. Heterogeneity in the phenotypes of endothelial cells have been identified in some cases, such as the distinct behavior of tip vs. stalk cells in angiogenesis [49], as well as in endothelial cells from different sites of human microvasculature [50]. This study helps to reveal how heterogeneity in cellular behaviors is manifested within a single plexus of presumably clonal capillary precursors on the same gel, in the absence of hemodynamically induced remodeling. For example, there existed a subpopulation of cells that exhibited similar displacement dynamics (with migration peaking at t=240 min) and were biased towards forming nodes in the final plexus (Figure 3-9). Moreover, we observed that upon initial inhibition of myosin II, most cells in the t=240 min cluster were drug-treated while most cells in the t=0 min cluster were untreated, even though the cells in the general population were evenly divided into drug-treated and untreated groups. Hence, the initial inhibition of cytoskeletal machinery appeared to bias the cells' migration behavior away from peaking at t=0 min, and towards peaking at t=240 min. Again, in this 50:50 mixture of drug-treated and untreated cells, most cells with maximum migration at t=240 min served as nodes in the final plexus, while cells that migrated strongly initially mostly formed branch structures. One interpretation is that if active migration was available, endothelial cells may prefer to form branch cells structures in the final

plexus; otherwise, they may migrate later (when cell-cell connections will have formed to enable coordinated movement) and ultimately form node structures.

The sources that drive the differences in cellular behaviors could be stochastic, as have been observed to drive biological variations in other systems [48]. Differences in the microenvironments around the endothelial cells could also drive different behaviors: for example, differences in local gradients or concentrations of VEGF (a growth factor that endothelial cells themselves secrete) have been shown to induce chemotaxis [24], and local differences in stiffness of the substrate (as little as 100 Pa) can result in differences in gene expression (such as VEGFR2) and subsequent vascular development [51]. Clonal endothelial cells have also been shown to exhibit epigenetic variations [52]. We also note that *in vivo* (which show similar behavior of microvasculogenesis as some studies of HUVECs in soft gels [53]), there exist additional sources of cell-to-cell variations due to variations in types and densities of neighboring cells (such as pericytes), compositions of local extracellular matrix, and vascular or interstitial flow.

3.4.2 Means and variations of cellular phenotypes

We observed a handful of distinct behaviors exhibited by most, but not all, cells. Interestingly, cells that exhibited a defined behavioral pattern in one phenotype (e.g. cell area) did not necessarily share the same dynamics for other phenotypes (e.g. box ratio). This result can be interpreted with previous findings that different gross morphological phenotypes are the results of varying and complex sets of molecular mechanisms [30]; for example, although actin distribution has been shown to account for the cell radius and aspect ratio, it does not necessarily account for other observed morphological parameters [30]. Therefore, if some but not all

molecular mechanisms match, some cells could correlate with each other based on one gross phenotype, but not necessarily across all phenotypes.

The manner in which phenotypes are distributed across a cellular population, or in a single cell across time, provided some interesting insights. Histograms of phenotypes across a population or across time (Fig. 2-10) showed that variation resulted from either a widening of a Gaussian-like distribution or multimodal behavior where multiple distinct behaviors (but not the intermediate phenotypes) were being populated. The latter case may reflect the cells undergoing occupation of distinct states (for example, in switching from a round motile state to an elongated state).

This study could also help quantitate the expected cell-to-cell variations within commonly used population-wide measurements, including bulk analytical measurements (such as protein expression) and morphological parameters such as average branch length, number of branches, number of nodes, or CLS area [34] for Matrigel assays. Moreover, since genetic knockdowns or pharmacological agents are often applied broadly across a cell population, this study will aid the interpretation of such perturbations by establishing the native cell-to-cell variations in behavior.

3.5 Conclusion

We applied the developed method in previous chapter to study the extent of cell-to-cell variation in a community of endothelial cells forming microvessels. Dominant dynamic patterns for each phenotype is discovered and correlated with the cell's final structural role in the tissue. In the future, improved understanding of how individual cells behave relative to the population-averaged behaviors could lead to improved engineering and synthesis of multicellular tissues and communities.

Chapter 4 Role of ECM-mediated strain propagation in microvascular tissue formation

4.1 Introduction

Most cells in body have the ability to change their locations during physiologic and pathologic events such as tissue morphogenesis [54] inflammation, wound healing [55], or cancer [56]. Tracks of isolated cell migration are persistent random walk [57], yet to achieve the desired physiologic outcome cells must collectively migrate in specific directions guided by local stimuli. A host of different stimuli ranging from chemical, mechanical [58], even electrical, or magnetic [59] cues have been implicated in the modulation and direction of cell locomotion. Among these stimuli, migratory patterns in response to chemical and mechanical cues have been widely studied (chemotaxis and mechanotaxis).

Directed migration of cells toward sources of cue chemicals is known as chemotaxis, and it requires linking the sensing of chemicals through receptors on the surfaces of the cells to the directional activation of the motility apparatus inside the cells. Mechanotaxis refers to the directed cell motility via mechanical cues. Cellular mechanotransduction systems can then transduce the physical signals into biochemical responses.

The migration of vascular endothelial cells (ECs) is critical in vascular formation and remodeling [60]. Moreover, understanding how cells could accomplish such complex tasks might reveal new ways to control cell motility for therapeutic purposes in inflammatory and degenerative diseases or cancer. Locomotion of isolated cells under influence of mechanical stimuli has been extensively studied [61]; substrate-mediated interaction of a cell pair [62] and a confluent monolayer of cells, show the significant role of extracellular matrix (ECM) in directing

cell migration, yet, ECM-mediated intercellular mechanical communication in a community of cells in the context of tissue morphogenesis has not been studied. The primary objective of this chapter is to understand how closely individual endothelial cells follow the guidance of mechanical cues (migrate in the direction of mechanical cues) during the process of CLS formation.

4.2 Methods

4.2.1 Preparation of fluorescent bead-laden Matrigel layer for PIV

Matrigel (9.8 mg/ml, growth factor reduced (GFR), phenol red-free; BD Biosciences) was stored at −20 °C and thawed at 4 °C at 24 h before use. 2% solid, 200 nm Fluorescent far red polystyrene beads (Invitrogen) were diluted (0.4µl in 500 µL) in cell culture medium, which was then mixed with Matrigel, to produce fluorescent bead-laden Matrigel. The embedded fluorescent beads would allow for visualization of ECM deformation during microvasculogenesis. A thin layer of Matrigel was casted in a 1.5 mm * 6 mm * 300 µm PDMS mold bonded to a Lab-Tek chamber slide dish (ThermoFisher Scientific). To ensure a flat surface, we flowed liquid Matrigel into the mold, and while a slab of BSA-treated PDMS placed over the mold. The Matrigel was allowed to gel at room temperature for 15 min. Once gelled, the BSA-treated PDMS slab was removed.

4.2.2 Single-cell patterning using non-adherent PDMS stencil

Using soft lithography techniques, an array of snowflake-shaped SU8 posts with the width of 8 µm, height of ~200 µm and 150 µm spacing between was patterned onto a silicon master (In order to achieve the pillar height of ~200 µm, SU8 3050 is spun at 900 rpm for 30s). Using replica molding, a membrane of polydimethylsiloxane (PDMS; Dow-Corning) was created by

spin-coating a thin layer of 1:7 (base: curing agent) PDMS at 2000 rpm for 30 sec The PDMS was allowed to cure at 70 ^{o}C for 30 min, then manually lifted from the master so that through-holes of the desired size and spacing were produced in the 130 µm thick membrane. The membranes were then attached to a thicker ring of PDMS to allow for easy handling and treated with oxygen plasma for 2 minutes to render the surface hydrophilic. A solution of 0.1 mM PLL-g-PEG (SUSOS, Switzerland) in pH 7.4 HEPES buffer was used to cover the membrane and ring assemblage for 1 hour to allow for full passivation of the PDMS surfaces, which rendered them non-adhesive to cells. After 1 hour, the PLL-g-PEG solution was removed and the PDMS assemblages were washed for 2 minutes each first in 1X PBS, and then in deionized water to remove excess PLL-g-PEG.

Early Passage (Passage 3), primary human umbilical vein endothelial cells (HUVECs) expressing GFP/RFP (GFP/RFP lentiviral particle transfected, puromycin resistant, stable) and human VEGFR2 shRNA stable transfected HUVECs were purchased from Angio-Proteomie (Boston, MA). Cells were expanded by endothelial cell growth medium supplemented with 2% fetal calf serum, 5 ng/mL EGF, 10 ng/ml BFGF, 10 ng/mL basic FGF, 20 ng/ml IGF, 0.5 ng/ml VEGF, 1 µg/ml ascorbic acid, 0.2 µg/mL hydrocortisone, and 22.5 µg/ml heparin at 37 °C, in a humidified and 5% CO_2-balanced atmosphere.

After locating the passivated PDMS stencil on top of the prepared Matrigel, we detached and seeded the GFP/RFP HUVECs at the density of 90 cell/mm^2 on top of the stencil and waited for 30 min to ensure that cells are transferred to the gel. Then by addition of media we cause the stencil to detach from the Matrigel and float up to the surface of media, where it is removed from the Lab-Tek dish. Now the patterned cells on top of fluorescent bead-laden gel is ready for imaging.

4.2.3 Image Acquisition

We collected data for 3 h, at 2 min interval, by using a long-term live-cell setup with an environmental chamber (Leica live-cell imaging system). We acquired phase contrast and fluorescent images (in two channels - red for the embedded fluorescent beads and green for cells) with a Leica DMI6000B inverted microscope equipped with a Leica DFC360 FX digital camera and Leica application suite advanced fluorescence (LAS AF) software.

4.2.4 Image Processing and Data Acquisition and Processing

The image processing and data analysis workflow is summarized in Figure 4-4. The image sequences of GFP endothelial cell migration and of embedded far red fluorescent beads are analyzed separately and in parallel. The final angle between cell displacement and gel strain vectors (from experimental and simulated model analysis respectively) calculated by dot product.

i. Cell Segmentation and Tracking

Due to the complexity of the endothelial cell behavior, processing (segmentation and tracking) of vascular tissue formation is an extremely challenging task and simple thresholding (for segmentation) and nearest neighbor method (for tracking) is not efficient enough to be used as a high-throughput method. We are adapting a new algorithm which uses model evolution approach [63]. In this algorithm level sets are chosen for the model because of their ability to segment objects of varying intensity and shape, to handle topological changes naturally, and to deal with both 2D and 3D image sequences. In this algorithm, each level-set function represents one object (cell), and the evolution equation for each level-set function is derived using the variational approach (energy function). The initial position of the level-set function in any frame is its final position in the previous frame. In the first frame, the initial position is found via segmentation with one level-set function and splitting the function according to the number of

connected components. Since this step is crucial for further tracking, and the single-level-set approach tends to lump closely positioned cells together, a watershed transform is applied to refine the results. To improve the separation of level-set functions corresponding to closely positioned cells, a Radon transform is applied, which "decouples" the active surfaces by means of separating planes, making it possible to apply the stopping criterion to each level-set function separately.

ii. Quantifying Cell Migration and Deformation

To determine localized directions of cell migration, cross correlation of the time-lapse image sequence was performed. Since single cells could not be considered as rigid bodies, cross correlation analysis was used to generate a field of displacement vectors at various points within the cell, instead of singly calculating centroid displacement. The image sequence was pre-processed by masking the background with the cell masks (generated through segmentation and tracking) to reduce noise.

A normalized cross-correlation algorithm was used to track 16x16 pixel subregions of each image with a center-to-center spacing of 2 pixels against the original image with a zero-order approach using the Image Processing Toolbox in MATLAB 7.12 (The Mathworks, Natick, MA). The displacements fields were then smoothed and differentiated using a 5x5 2D Savitsky-Golay bilinear least squares filter [64]. Points within 2 pixels of the edges of the cell were discarded from the analysis due to the square filtering process used. This analysis was performed across the time-lapse sequence on two consecutive images 2 min apart, resulting in vector representations of cell migration at each point in space and time.

iii. Particle Image Velocimetry

To determine the strain field created by cells in Matrigel, the frame to frame displacement of embedded fluorescent beads were obtained through Particle Image Velocimetry (PIVlab plugin; MATLAB). Selected pairs of consecutive time points (i.e. frames 4-5, 5-6, 6-7) in the desired time range were analyzed by PIV to generate displacement fields. The PIV algorithm output consisted of a strain vector field at each experimental time point, with respect to the previous time point. These vectors are then used as boundary conditions in the finite element simulation detailed below.

iv. Finite Element Analysis

To simulate the transmission of displacement through ECM, a 3D finite-element model was developed comprised of three major components: 1-Material properties of the Matrigel 2-Geometry derived mesh 3-displacement boundary conditions derived from the PIV data.

In order to simulate the nonlinear mechanical properties of the Matrigel, we chose the hyperelastic material. Most biopolymers show hyperelasticity under excessive strain [65]. We tested multiple material models (viscoelastic and hyperelastic: Yeoh and Mooney-Rivlin); Moneey-Rivlin model fit the data with minimal error. This model is a hyperelastic material model where the strain energy density function (W) is a linear combination of two invariants of the left Cauchy–Green deformation tensor. The strain energy density function for an incompressible Mooney–Rivlin material is given by:

$$W = C_1(\bar{I}_1 - 3) + C_2(\bar{I}_2 - 3)$$

Where C_1 and C_2 are empirically determined material constants, and $\bar{I}_1$ and $\bar{I}_2$ are the first and the second invariant of the unimodular component of the left Cauchy–Green deformation

tensor. In order to find the C_1 and C_2 constants, we simulated the model for the whole field of view, and imported the displacement boundary conditions for all cells. We extracted the displacement data at the locations where we did not define as boundary condition and compared it to the PIV data. We then used dot product to calculate the error between the simulated displacement field and the experimental PIV data. In order to minimize the error and find the optimal values of the C_1 and C_2 constants, we used the *patternsearch* function in the global optimization toolbox of MATLAB 7.12 (The Mathworks, Natick, MA).

Having found the optimal material properties, we defined a 500 µm by 500 µm by 300 µm block (representing Matrigel) around the cell of interest. The mesh size within this geometry is 0.1 µm. In order to only simulate Matrigel displacement as the result of the emitter cells (the arbitrarily defined group of surrounding cells that send the mechanical signals) and ECM traction, and to exclude the cell/ECM traction for the cell of interest (the central cell which is receiving the mechanical cues), we imported the PIV displacement data, as boundary conditions, only at the position of the emitter cells at the top of the block (i.e. For each pixel within the outline of the emitter cells, we imported one displacement vector) . The bottom of the block is set as zero-displacement boundary condition and the sides of the blocks are defined as free. We solved the model under quasi-static condition in COMSOL (COMSOL AB) using direct solver and extracted the strain field at the location of the cell of interest (We then repeated the simulation for all cells at all time-points).

v. Comparison of Experimental Migration and Simulated Model Strain Vectors

To understand the influence of mechanical cues on the direction of cell migration, the experimental migration vector field (from cross-correlation analysis) was overlaid with the simulated strain vectors (determined from finite element simulation). At each location, the

migration vector was compared with the corresponding simulated strain vector. The dot product was used to determine θ_m, the angle between the directions of migration and mechanical cues. The distributions of θ_m were visualized by heat maps and histograms at each time point to determine how closely the migration direction followed simulated mechanical cues.

4.3 Results

We developed a methodology to decipher the roles of mechanical cues in directing the migration of endothelial cells in the early stages of vasculogenesis. This method uses timelapse live-cell fluorescence microscopy followed by automated analysis of cell movement and ECM deformation. We used Particle Image Velocimetry (PIV) combined with Finite Element Analysis (FEA) to measure/simulate the mechanical signals sensed by ECs. We studied the transmission of mechanical cues from the arbitrarily defined group of "*emitter*" cells (outlined in black, Figure 4-1) to a single "*receiver*" cell (outlined in white, Figure 4-1). Black vectors show the cell-ECM traction, generated by the emitter cells, while the white vector "mc" show the resultant simulated displacement at the location of the receiver cell; this represents the mechanical cues sensed by this cell. We determined the angle between the cue vector "mc" and the direction of migration of the receiver cell (shown as vector "v" in Figure 4-1) to calculate θ_m ("m" for mechanotaxis). The smaller the absolute value of θ_m is (with the minimum of 0°), the closer the cell is following the mechanical cues and the larger the absolute value of the angle is (with the maximum of 180°), the less the cells are following those signals.

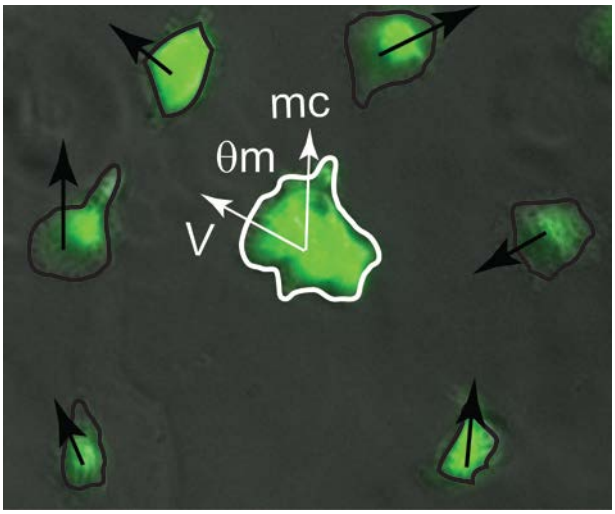

Figure 4-1: Intercellular mechanical signaling. "*Emitter*" cells are outlined in black while the "*receiver*" cell is outlined in white. Black vectors show the cell-ECM traction, generated by the *emitter* cells, while the white vector "mc" show the resultant simulated displacement at the location of the *receiver* cell. The angle between the cue vector "mc" and the direction of migration of the receiver cell "v" shown as θ_m ("m" for mechanotaxis).

Inference of spatiotemporal relationship between mechanical cues and ECs migration could be easily drowned in low sample sizes or noisy population data. To increase the sample size and in order to ensure a uniform initial condition for all cells within the population, we patterned single cells on Matrigel via sedimentation through a non-adhesive PDMS stencil.

4.3.1 Patterning an array of single-cells on Matrigel

Previously, we have shown that random seeding of the endothelial cells on Matrigel results in a significantly different initial migratory behavior [66]. Moreover, the aggregation of multiple cells imposes numerous challenges on the segmentation and tracking of cells. In order to ensure a uniform initial condition for all cells within the population, we patterned single cells on Matrigel via sedimentation through a non-adhesive PDMS stencil. This technique allows for tight control over initial cell-to-cell spacing, which is an important parameter in determining the cell-to-cell transmission of cues during the early stages of microvascular formation. In studying the population-level behavior of individual cells, it is critically important to ensure that initial

conditions are as uniform as possible. Using standard soft-lithography techniques, we fabricated a thin layer of PDMS membrane (130 µm thick) having an array of snowflake-shaped through-holes (letting a single cell to pass through). Prior to patterning the cells on Matrigel, we passivated this membrane with non-adhesive PLL-g-PEG and used it as a stencil to pattern cells (Figure 4-2).

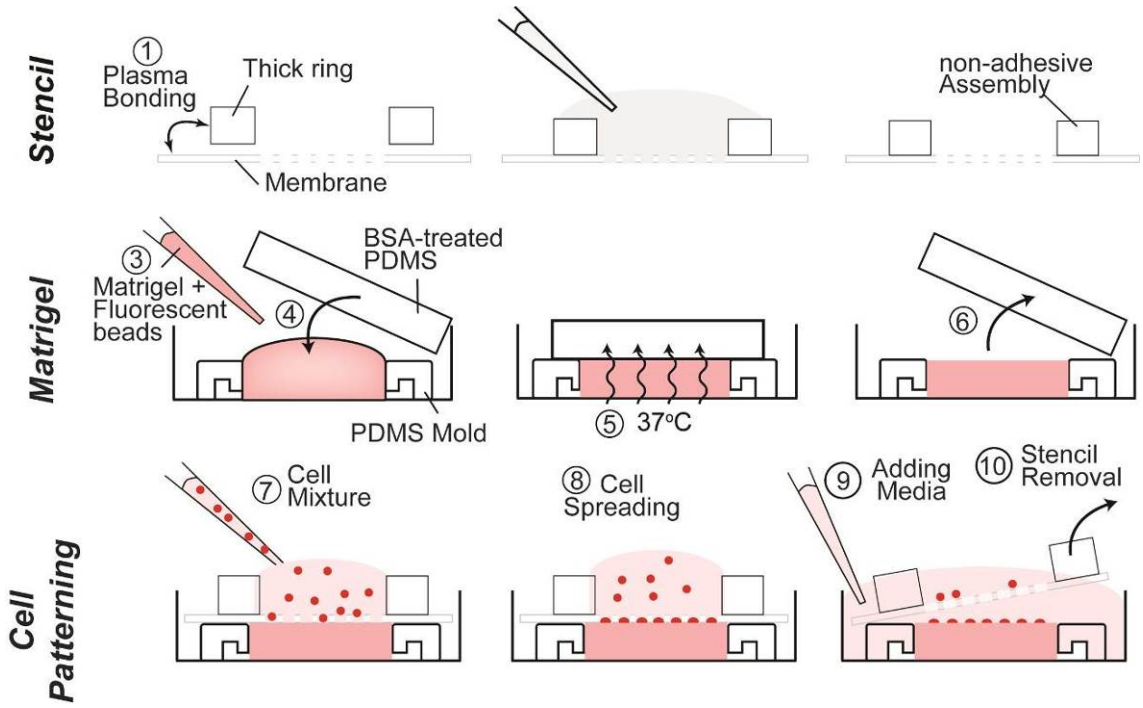

Figure 4-2: Setup preparation. (1) Bonding of poly(dimethylsiloxane) (PDMS) membrane and thick ring to make stencil (2) PLL-g-PEG passivation of the assembly (3) Addition of fluorescent-bead-laden Matrigel in the chamber (4) Placing BSA-treated PDMS cap to ensure a flat surface (5) Gelling of Matrigel at room temperature (6) Removal of PDMS cap (7) Placement of stencil on top of the flat surface of matrigel and loading the cells (9) Addition of media to float stencil (10) Removal of stencil

This single-cell patterning technique led to distributed strain field generation through the ECM, which helped to delineate the contributions of individual cells. Analysis of the strain field between randomly-seeded cells by Particle Image Velocimetry (PIV) revealed large strains generated by clusters of cells which masked the smaller strains in the intermediate zones. To the contrary, when patterned, cells are generating relatively uniform strain, easily traceable (Figure 4-3).

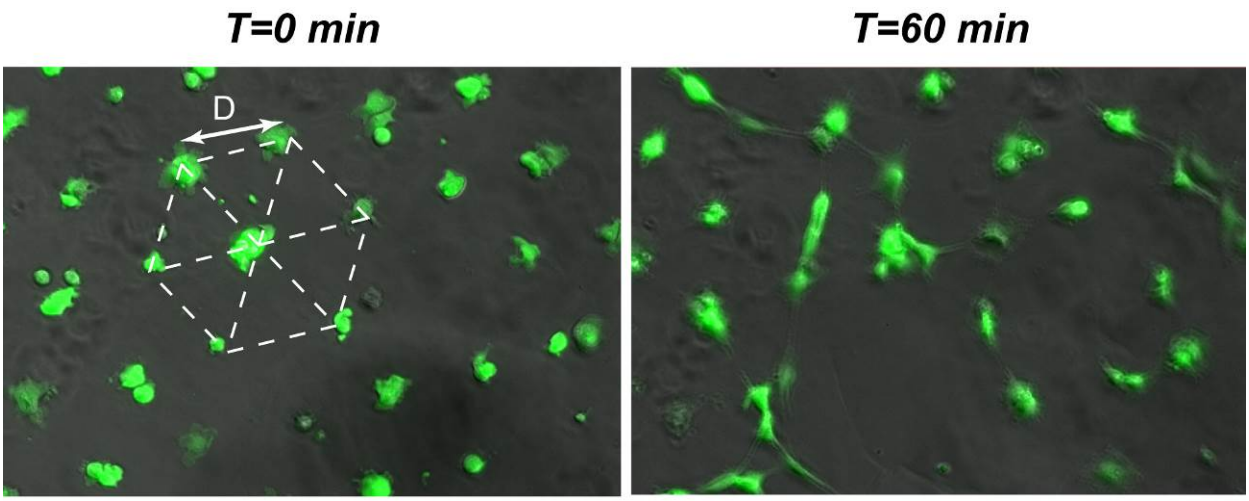

Figure 4-3: Single-cell patterning on Matrigel. Native GFP-expressing HUVECs patterned on Matrigel immediately after stencil removal (left) and self-assembly after one hour (right). Cell-to-cell separation distance (D) is 150 µm.

4.3.2 Particle Image Velocimetry (PIV), and Finite Element Analysis (FEA) capture the cell-to-cell transmission of mechanical signals in real-time

Numerous techniques have been developed to study mechano- sensing and transduction: cell-generated force measurement (e.g. deformable substrates), external application of force (laser tweezers), and rigidity manipulation (e.g. polyacrylamide gels). Yet, none of these techniques are suitable to study cell-cell communication via mechanical signaling in the context of tissue morphogenesis. Here, by combining PIV and FEA we studied the mechanical signals transmitted from the arbitrarily defined group of *"emitter"* cells to a single *"receiver"* cell. We used PIV to quantify the cell-ECM traction and derived the displacement field in the ECM generated by the *emitter* cells (Figure 4-4B right, white-outlined cells). By mixing nanometer-sized polystyrene fluorescent beads within Matrigel (ECM), we characterized cell mediated ECM deformation. Importing these data as the boundary conditions to the finite element model, we simulated the transmitted signal through the ECM towards the *receiver* cell (Figure 4-4B right, the cell outlined in red). Also, we measured the migration and deformation of the *receiver* cell, so that we can calculate the angle between these two.

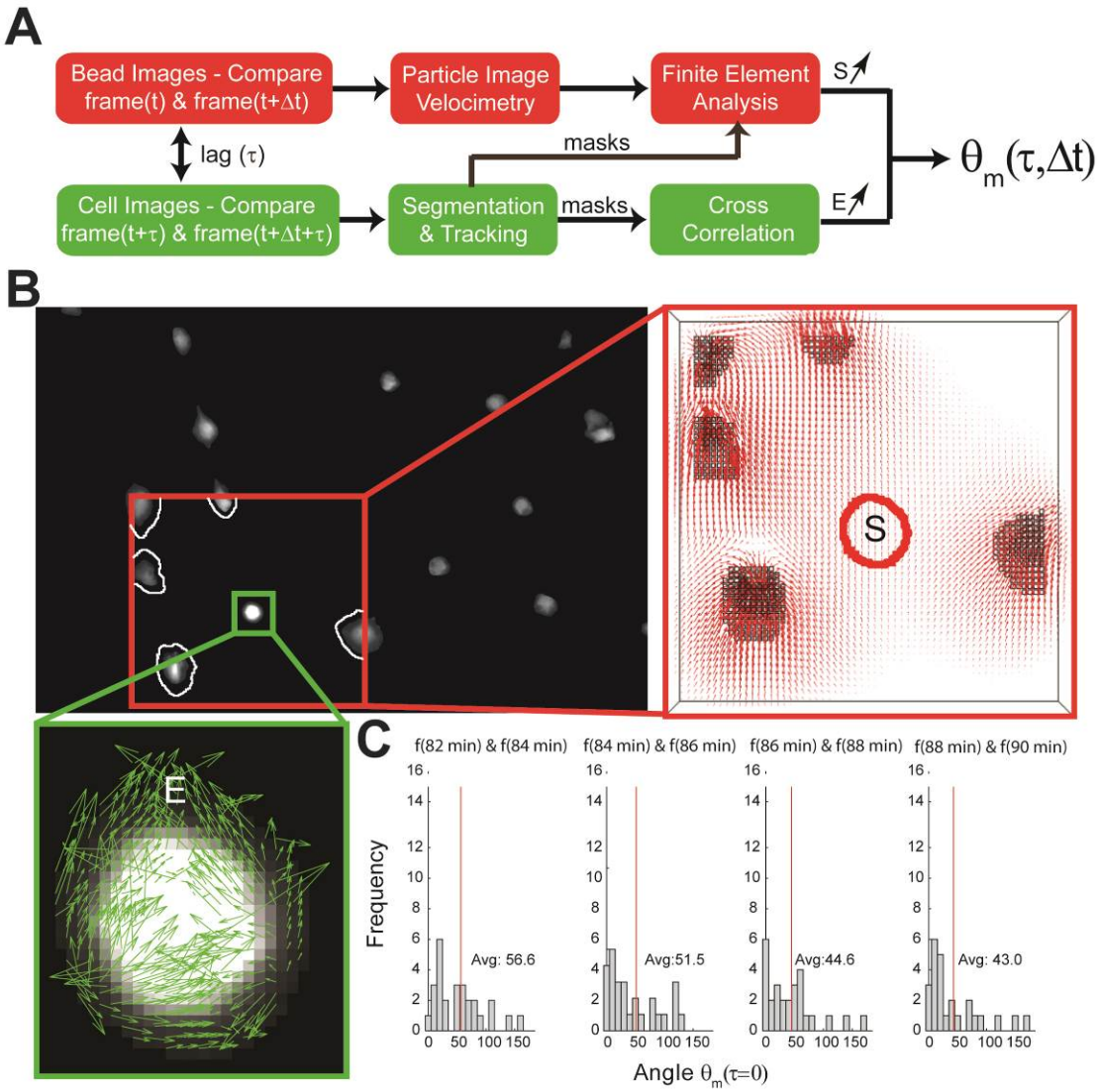

Figure 4-4: Mechanically-guided cell movement. Flowchart showing the steps to extract the local cues around the cell of interest. **(A)** From L to R: Two raw image sequences of GFP HUVECs and far red fluorescent beads are processed in parallel. Image pairs with corresponding time is analyzed for both sequences (frame(t) and frame(t+Δt)). A lag factor (τ) is defined for the case of characterizing the delayed effects of mechanical cues on migration. Particle Image Velocimetry (PIV) is performed to generate a displacement vector field which is then used to simulated transmitted mechanical signals (S). Cross-correlation is used to measure cell displacement vector field (E) **(B)** Segmentation and tracking of cells in the corresponding frames of the cell image sequence is performed, generating masks for each cell (B, top-left). Using the cell masks and the displacement vector field as boundary conditions, finite element simulation (FEA) is performed the surrounding cells while excluding the cell of interest using (red outline in B, top right). FEA generates a strain vector field felt by the cell of interest, red arrows within the red outline (S) show the direction of mechanical signals transmitted to the receiver cell (B, top right). Cross-correlation is performed on the noise-reduced (via cell masking) frames of the cell sequence, generating a displacement vector field with vectors (E, green arrows) representing migration of the cell at each point (B, bottom-left). **(C)** Comparison of vector fields E and S for the whole population. A dot product between these vectors is taken to determine the angle θ_m, which encodes how well cell migration follows the mechanical cues transmitted from neighboring cells. Distributions of θ_m for the central cell is shown over t=82 to t=90 min with a lag τ=0.

Figure 4-4C shows the distribution of angle θ_m for the population of endothelial cells. The average of the angle distribution is decreasing with time which indicates that the cell is more closely following the mechanical cues.

4.4 Discussion

The transmission, sensing and translation of mechanical signals to biochemical signals are being extensively studied. Analysis of ECM-mediated strain propagation allows us to study the first step in this process: mechanical signal transmission. By combining our technique in the analysis of single-cell migratory behavior, as described in the previous chapters, with the characterization of ECM deformation, we studied the role of mechanical signaling in microvascular formation. We used particle image velocimetry algorithm (applied to the images of bead-laden gels) to measure the strain field throughout the gel. However, unlike the previous studies, we dissected the effect of transmitted strain by the "*emitter*" cells and the strain generated by the "*receiver*" cell itself via finite element analysis. The population-wide decrease in the angle between the transmitted mechanical signals and the direction of cell migration shows that mechanical signals play a more important role in the later stages of CLS formation. Studies show that ECs reorganize the fibrillar structure of hydrogels (e.g. collagen) as they form microvascular tissue [67]. Remodeling of the ECM could potentially facilitate and enhance the transmission of mechanical signals. Matrigel coated on hydrophilic surfaces is shown to form a fibrillar structure which lends support to the idea of strain transmission enhancement at later time points via ECM remodeling [68].

The common drawback in the previous studies of ECM-mediated intercellular mechanical signaling is the small number of cells studied [62]. Our single-cell patterning technique combined with the advanced computational algorithms allows the high-throughput study of

ECM-mediated mechanical signaling. Moreover, we could easily incorporate other stimuli (e.g. biochemical factors) that derive tissue morphogenesis. Biochemical factors could be introduced to this setup as a uniform gradient or as a point source using growth factor laden microspheres.

4.5 Future work

This platform is amenable to the incorporation of other stimuli (e.g. biochemical factors) that derive tissue morphogenesis. Using similar methodology, we can study how cellular migration follows the biochemical signals such as growth factors (Figure 4-5).

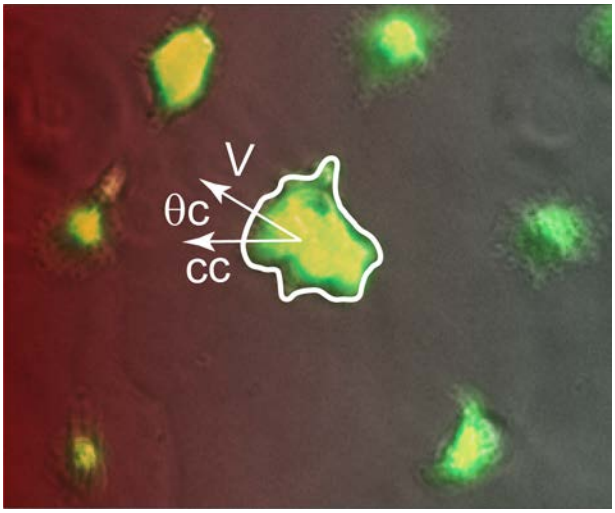

Figure 4-5: Biochemical stimuli. Schematic of growth factor gradient (in red) with the direction of maximum gradient shown as vector "cc" in white. The angle between the cue vector "cc" and the direction of migration of the *receiver* cell "v" is shown as θ_c ("c" for chemotaxis).

We are currently testing a microfluidic device capable of establishing a stable gradient of growth factor (VEGF) across Matrigel (Figure 4-6A). By altering the relative concentration of VEGF (in source and sink tubes), we are able to create the desired gradient. In order to minimize the disruption of VEGF gradient via convection in media, we placed an agarose slab on top of Matrigel leaving a gap in between such that ECs could freely migrate. We verified the establishment of a stable gradient using a fluorescently-tagged 40 kDa dextran, serving as the surrogate for VEGF (Figure 4-6B).

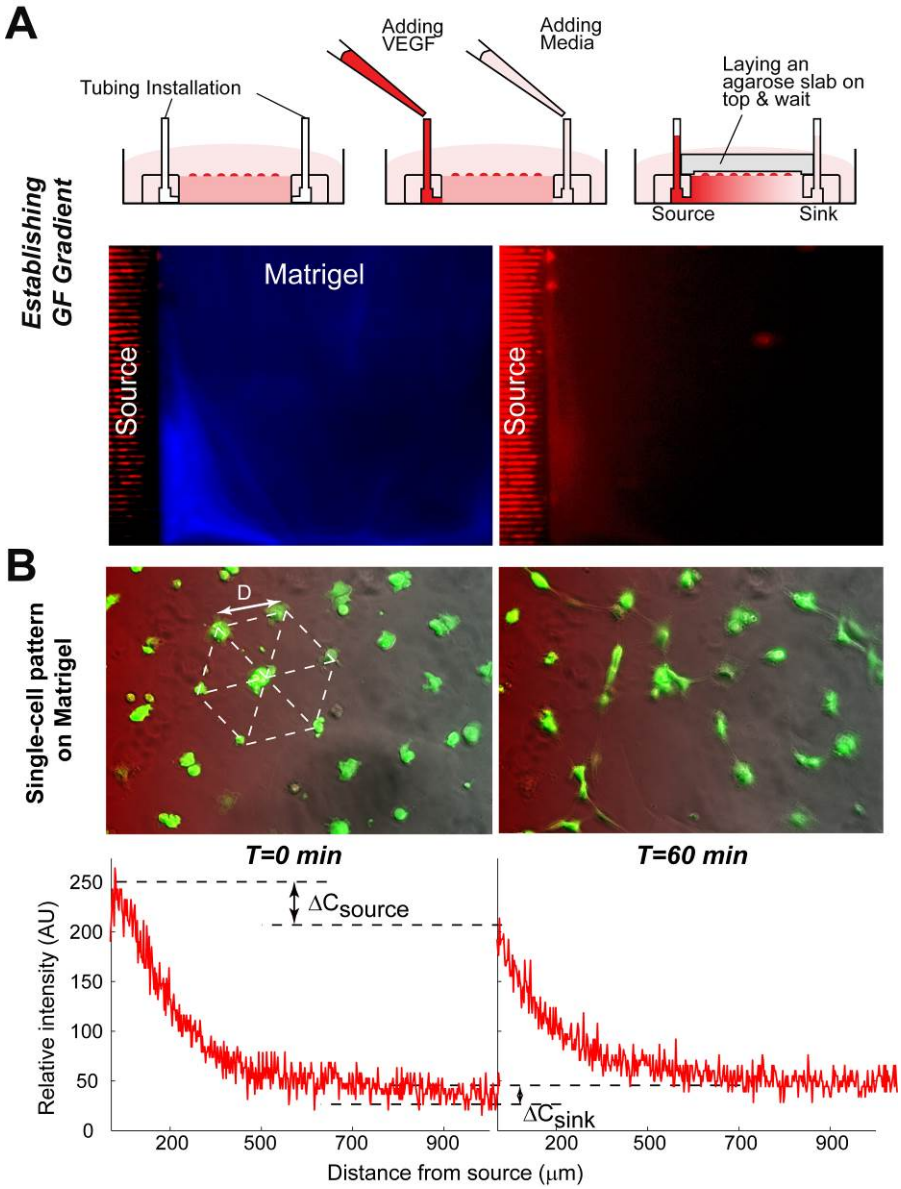

Figure 4-6: Establishing growth factor gradient. (A) Setup preparation, top from left to right: Punching of hole through wells on PDMS mold and installation of the tubing. Addition of basal media to one tube (sink) and VEGF-enriched media to other tube (source) to create VEGF gradient followed by placement of agarose on top of Matrigel and 30 minute wait. Bottom left: Loading of Matrigel in chamber (blue) and fluorescently-tagged 40 kDa dextran (red), serving as surrogates for VEGF165 bottom right: diffusion of dextran through the gel and establishing a stable gradient **(B)** Gradient of growth factor across the Matrigel at t=0 (left) and after 1 hr (right).

By comparing the direction of migration of the individual cells with the direction of VEGF gradient, we can decide on the significance of the chemical cues in directing the migration of ECs in the process of capillary-like structure (CLS) formation.

We can extend our analysis to decouple the role of mechanical and chemical cues responsible for guiding the process of CLS formation. We will compare the migratory behavior of endothelial cells to both chemical and mechanical cues present in the microenvironment. Using the microfluidic setup we established a stable gradient of VEGF with known direction and magnitude in the Matrigel substrate. Both Native HUVECs and VEGFR2 knocked-down HUVECs (which are not attracted toward the gradient of VEGF – as negative control) will be patterned separately onto Matrigel with embedded fluorescent beads, then imaged over a 3 hour period at 2 min intervals. To determine cell migration/deformation vector field with subcellular resolution, we will run the digital image correlation algorithm on all pairs of consecutive frames. For each cell at each time point, we will use these vectors to determine the angle between the direction of migration and A) the known direction of VEGF gradient: θ_c ("c" for chemotaxis) and B) the reconstructed mechanical signals θ_m ("m" for mechanotaxis) from PIV and FEA. The smaller the absolute value of θ_c or θ_m are (with the minimum of 0°), the closer the cell is following the chemical or mechanical cues and the larger the absolute value of the angle is (with the maximum of 180°), the less the cells are following those signals. A θ_c or θ_m value of 0° indicates complete alignment of the cell migration with the chemotactic or mechanotactic cues respectively, while the value of 180° could indicate that cells travel in the opposite direction. We will aggregate the values of θ_c or θ_m into a population distribution for native and knockdown HUVECs (Figure 4-7).

The distributions for θ_c and θ_m are compared across both cell types (native vs. knockdown HUVECs) to elucidate the dependence (or lack thereof) of CLS formation on mechanical and chemical cues (Figure 4-7).

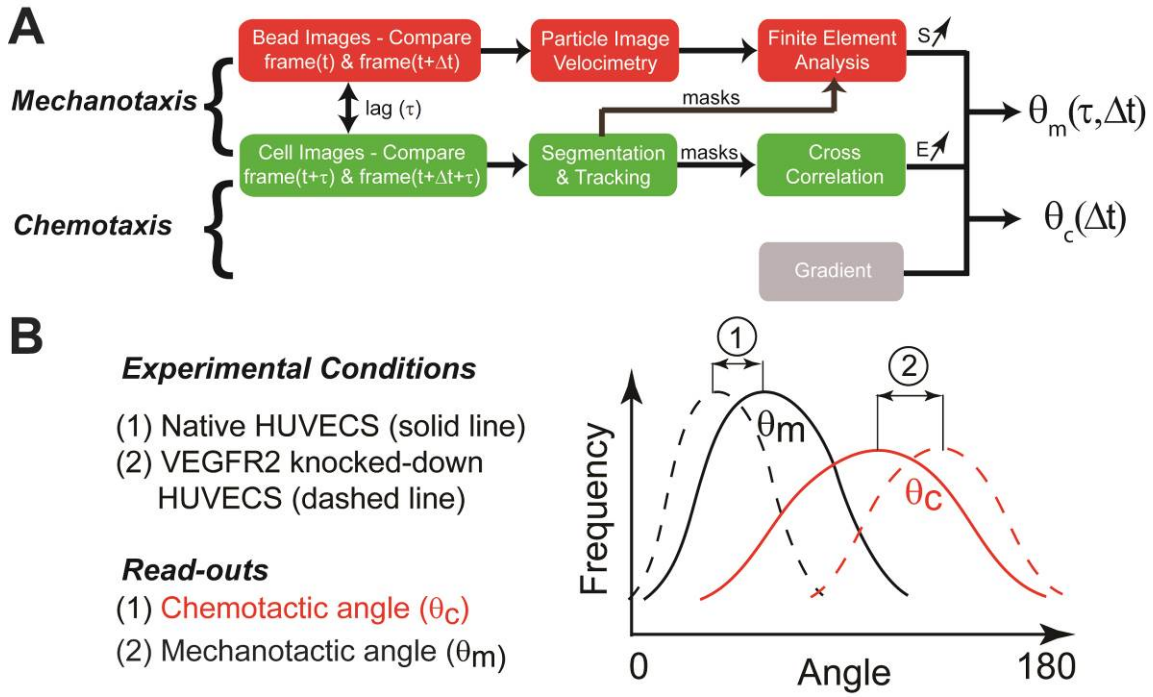

Figure 4-7: Deciphering the role of mechanical versus chemical stimuli in microvascular formation. (A) updated flowchart for Analysis and extraction of local mechanical and chemical cues as θ_c and θ_m **(B)** comparison of θ_c and θ_m distributions at each time point for native cells and VEGFR2 knocked down control cells

Chapter 5 Modeling analyte capture and enhancement strategies in microfluidic heterogeneous immunoassays under real-world constraints

5.1 Introduction

Microfluidic technologies have tremendous potential for creating portable health diagnostic devices for resource-poor settings due to advantages in size, volume requirement, and time to analysis [69-74]. In particular, hetereogeneous immunoassays [75], in which analytes from a sample solution bind to capture molecules immobilized on solid surfaces (such that analytes not bound to the capture molecules are removed), are well positioned to leverage efficient mass transfer to form a clinically useful class of laboratory tests, including point-of-care tests [76]. Despite the prevalence of microfluidic-based heterogeneous immunoassays [77-87], there is incomplete understanding of how assay parameters can influence the amount of captured analytes. For example, seemingly simple (but in practice, important) questions such as the optimal flow rate to use in an assay, or whether to pass a small plug of concentrated reagents through *vs.* a large plug of dilute sample, are typically optimized empirically, with only a limited theoretical consideration of the underlying physical process. An improved understanding and optimization of these physical processes, especially under true "real-world" constraints (such as finite reagent or sample volume, assay time, and capture area) may be particularly beneficial for the design of point-of-care assays, where volumes of reagents and available samples are limited (microliters of blood from a finger prick *vs.* milliliters from venipuncture), and the desired time-to-result short (minutes at the point of care *vs.* hours in a bench-top setting).

In multiwell plates, the rate of capture of protein analytes on functionalized solid surfaces is usually limited by the diffusion of analytes from the bulk phase to the boundary layer [75]. Under flow in microchannels, this transport process is thought to be kinetically rapid due to the proximity of the analytes to the surface [88], and the rapid replenishment of depleted analytes in the boundary layer by convective flow [89]. Previous studies have built general theoretical models that couple convective flow to surface binding for heterogeneous immunoassays [90-92] and surface plasmon resonance [93]. Under real-world assay conditions, however, it remains unclear what the optimal assay parameters (such as flow rate or concentration of patterned capture molecule) should be. Moreover, oft-cited advantages of microfluidics for analytical applications can lead to contradictory predictions for optimizing assay parameters: for example, a high flow rate in microchannels can speed up an assay and also enhance the final signal (by quickly replenishing depleted analytes in the boundary layer with a fresh bulk layer), but at the same time diminish the advantage of low reagent consumption.

Here, we use computational analysis (based on finite-element models) to studying the dynamics of the analyte-capture process in microfluidic-based heterogeneous immunoassays under real-world limitations and the strategies to mitigate these limitations. We, experimentally (based on the surface capture of fluorescent antibodies) validated our numerical findings. We aim to examine the effect of varying assay parameters (such as flow rate and concentration of capture molecules) on the final amount of captured analytes.

Afterwards, we separately investigate signal enhancement, an important step in increasing the sensitivity of microfluidic heterogeneous immunoassays. Specifically, we look at gold-catalyzed reduction of silver, proposing a reaction model and performing experimental assays under a range of surface gold density and silver development time in order to minimize total

assay time. Also, we investigated the possibility of the introduction of multiphase flow to enhance analyte transport.

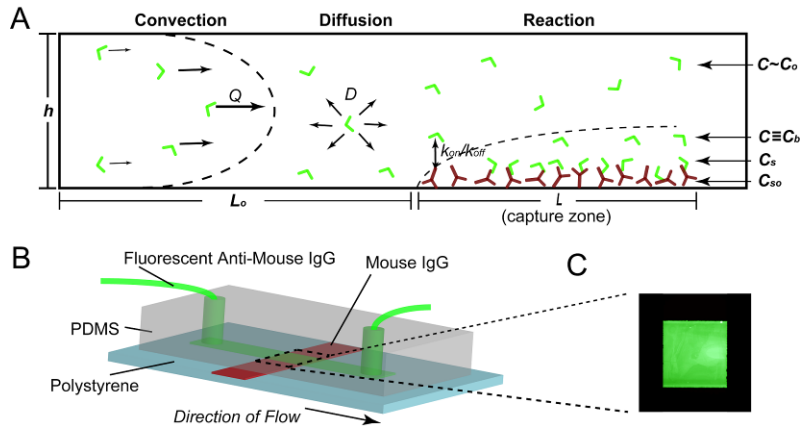

Figure 5-1: Schematic diagram of the physical processes and experimental setup of a microfluidic-based heterogeneous immunoassay. (A) Schematic diagram of the three central physical-chemical processes (convection, diffusion, and surface binding), and key parameters in this study. The parameters h, L, and L0 define the microfluidic geometry (with L defining the length of the capture zone, over which surface-bound capture molecules have been patterned). Capture molecules are shown in brown, and the analytes in green. The parameters Q define flow rate, D diffusion coefficient of the analyte, and kon/koff the rate constants for surface association and dissociation. The analyte concentration in solution C is a function of the spatial position, with the C in the bulk layer approximately equal to C0 (the analyte concentration at the microfluidic inlet) and C at a layer 1 µm above the capture zone defined as the boundary layer concentration Cb. On the surface, the surface concentration of captured analytes Cs and surface-bound capture molecules Cso are considered explicitly in the model. **(B)** Schematic diagram of the PDMS-based microfluidic immunoassay performed in this study. A fluorescent anti-mouse IgG is used as the analyte, and mouse IgG as the surface-bound capture molecule. **(C)** Fluorescence image of analytes captured by the surface-bound molecules.

5.2 Methods

5.2.1 Theoretical background and numerical simulation of analyte capture process

A shows the three major physical processes considered in our computational model: 1) convection along the microchannel, the principal mass transport process along the axis of the microchannel; 2) diffusion (in which analytes move in all directions), the principal process for transporting an analyte from the bulk layer to the boundary layer; 3) surface reaction, the binding of an analyte in the boundary layer to the solid surface (which is functionalized, over a "capture zone", with capture molecules that specifically recognize the analyte). We considered the following governing equations:

(1) $\frac{\partial C}{\partial t} + \vec{u}\nabla C = D\nabla^2 C$ Convection-Diffusion equation

(2) $\rho\left(\frac{\partial u}{\partial t} + \vec{u}\cdot\nabla u\right) = -\nabla p$ Navier-Stokes equation

(3) $\frac{\partial C_S}{\partial t} = D_S\nabla^2 C_S + k_o C\theta - k_o C_S$ Surface binding reaction: $C + \theta \xleftrightarrow{k_{on},\ k_{off}} C_S$

where C is the volume concentration of the analyte (mol/m^3), D is diffusivity of the analyte in the bulk (m^2/s), ρ is fluid density (kg/m^3), $\vec{u}$ is flow velocity (m/s), P is pressure (Pa), C_s is the concentration of surface-bound or captured analytes (mol/m^2), $\theta = C_{so} - C_s$ is available binding sites (where C_{so} is the surface bound antibody concentration) (mol/m^2), D_s is surface diffusivity of the analyte (m^2/s), and k_{on} (m^3/mol-s) and k_{off} (1/s) are the association and dissociation rate constants respectively.

We used the multi-physics capability of the software COMSOL (COMSOL AB, Stockholm, Sweden) to solve the partial differential equations for convection-diffusion and surface reaction. We solved the convection-diffusion partial differential equation (PDE) over the entire domain to determine the concentration of analyte in bulk flow (*i.e.* C), and simultaneously solved the surface binding reaction PDE over the capture zone for C_s based on C derived from the convection-diffusion PDE, to determine the change in the concentration of the captured analyte (*i.e.* C_s). (Since the width of the channel is much greater than the height in our model and the flow is laminar, the velocity profile at each cross-sectional plane could also be replaced by a parabolic function rather than being derived from equation 2.) The first term accounts for spatial variation of C_s along the patch, and second and third terms account for the on and off reactions, respectively, in the surface reaction. Simulation times were defined by user-imposed real-world constraints, such as fixed sample volume or finite assay time.

The three physical phenomena (diffusion, convection, and surface binding) are governed by the following assay parameters:

- geometrical parameters (channel width (w), height (h), binding surface or patch length (L), pre-patch length (L_0))
- reaction constants of the receptor-ligand pair (association constant (k_{on}), dissociation constant (k_{off}))
- microfluidic operating conditions (pressure (P), flow rate (Q), time of assay (t), surface-bound antibody concentration (C_{so}))
- molecular properties (analyte concentration (C_o), solute diffusivity (D), surface diffusivity (D_s))

5.2.2 Extension of current computational framework to study analyte-capture in two-phase flow

To simulate immiscible fluid flow, volume of fluid (VOF) method is normally used. This function finds the fluids interface by solving the level-set PDE (4) simultaneously with Navier-Stokes (2).

$$(4)\quad \rho\left(\frac{\partial\phi}{\partial t}+\vec{u}\cdot\nabla\phi\right)=-\gamma\nabla\cdot\left[\varepsilon\nabla\phi-\phi(1-\phi)\frac{\nabla\phi}{|\nabla\phi|}\right]$$

Where φ determines fluids interface (φ = 0.5), $\vec{u}$ is flow velocity vector (m/s), ε is interface thickness (ε = h/2, where h is the characteristic mesh size in the region passed by the interface) and γ parameter determines the amount of reinitialization. We simulated bubble flow in a T-junction microchannel by simultaneous solution of level set function and Navier-Stocks. Then

the solution (velocity field) is exported to be used for solving convection-diffusion (1) and reaction (3) PDE simultaneously.

5.2.3 Device design and fabrication

We used standard soft lithography to fabricate parallel microfluidic channels [8]. Briefly, we spin-coated a 50-μm layer of epoxy-based photoresist SU-8 2050 (MicroChem, Newton MA) onto a Si wafer (Silicon Sense, Nashua NH), exposed it to 365-nm light through a transparency photomask using a Karl Suss MJB3 contact mask aligner (Garching, Germany), and developed the features with propylene glycol monomethyl ether acetate (Sigma-Aldrich, St. Louis MO). After replica molding the masters with polydimethylsiloxane (PDMS) (Sylgard 184 Silicone Elastomer Kit, Dow Corning, Midland MI), we punched holes through the PDMS molds using a flattened 16G1$^{1}/_{2}$ needle (Becton Dickinson, Franklin Lakes NJ) to create inlets and outlets.

5.2.4 Heterogeneous immunoassay for analyte capture

To prepare the device for an immunoassay, we patterned a 500-μm wide stripe of mouse IgG antibody onto treated NUNC polystyrene plates (NUNC, Rochester NY) by conformally sealing a PDMS mold with a single microchannel, filling it with 200 μg/ml (~1.3 μM) of mouse IgG suspended in PBS (Invitrogen, Carlsbad CA), and allowing the antibody to physically adsorb onto the surfaces for 1.5 hours at room temperature. After adsorption, we washed the microchannel three times with PBS, and peeled the PDMS mold off the plate to reveal an antibody stripe. We washed the plate with deionized water, and dried it with nitrogen gas to remove dust and dirt. Next, we conformally sealed a PDMS mold containing parallel microchannels - each 500 μm wide by 60 μm tall by 3 cm long - in an orientation orthogonal to the patterned antibody stripe. We blocked the microchannels with 1% BSA (in PBS) for 2 hours

to prevent nonspecific protein adhesion to surfaces, and then washed the channels three times with 0.1% Tween-20 (in PBS). To perform an assay, we loaded a plug of AlexaFluor-488 conjugated goat anti-mouse $F(ab')_2$ antibody (Invitrogen) – which acted as our analyte – followed by a long plug of 0.1% Tween-20/PBS in PE-60 polyethyelene tubing (Intramedic; ID 0.03”). We varied the goat antibody in volume (5 to 50 μL) and concentration (10 to 100 nM), and injected it into the microchannel using a syringe pump (model Orion M362, Thermo Electron Corporation) that was set at various flow rates (0.015 to 100 μL/min). (We found that an important parameter to control is slight differences in the measurement of analyte volumes in the PE tubing, which can significantly affect analyte capture. We also minimized non-specific adsorption by using a short section of tubing to load the reagents.) After the analyte passed through the channel, we washed the channel with the PBS/Tween plug for 1 minute at 10 μL/min. Next, we filled the channels with distilled water, and measured the fluorescence intensity of captured goat antibodies using an epifluorescence microscope (model DMI6000B, Leica Microsystems) under full intensity and wide field diaphragm at 10x magnification, with exposure times set at 1000 ms. We quantified the fluorescence intensities using the software ImageJ (NIH, Bethesda MD). To approximate conditions without flow (i.e. “static” conditions), we injected a plug containing the analyte into the microchannel, and left it incubating overnight. We then flushed out the analyte, washed the channel three times with 0.1% Tween (in PBS), and imaged the fluorescence as described. In “finite time” experimental assays, for assays with run times exceeding the time limit (such as assays with diluted samples at low flow rates), we stopped the assay at two hours, increased the flow rate to 10 μL/min to clear the microchannel of sample, and washed for 1 minute with 0.1% Tween (in PBS) as described above.

5.2.5 Immunoassays for kinetics of gold-silver enhancement

To guide model development (in forming a general mechanism and determining best-fit values of kinetic parameters *e.g.* rate constants), we first studied a simplified experimental system of physisorbing different amounts of capture antibody to produce a range of surface gold density. (We controlled the amount of anti-goat antibody physisorbed to the surface by adding varying amounts of BSA as a competitor). We used the procedure described previously to functionalize one meandering detection zone per channel with a particular ratio of anti-goat IgG antibody:BSA. We loaded all tubes with the following sequence of reagents: one lead wash buffer plug (~ 1.3 μL), one plug (~ 11.2 μL) of gold nanoparticle-conjugated goat anti-human IgG antibody, two small plugs (~ 1.3 μL each) of washing buffer, and four small plugs (~ 1.3 μL each) of distilled water (*i.e.* a reagent sequence which lacked patient sample and trailing buffer washes). We collected a transmittance reading of the target zone every second during silver development to generate absorbance curves over time.

5.3 Results

5.3.1 Basic description of theoretical model

Our computational model featured the simultaneous solution of two nonlinear partial differential equations: convection-diffusion and surface reaction (equations 1 and 3), while solving for the velocity field in the Navier-Stokes equation. These equations account for the three basic physical processes of convection, diffusion, and surface reaction in our analyte-capture process (Figure 5-1A). To render the computational problem tractable, we modeled the microfluidic system as a two-dimensional cross-section along the major axis of the channel; we believe this approximation still captures the essence of a three-dimensional microfluidic system because there is minimal exchange of molecules across fluid streams due to laminar flow (with

the Reynolds number of our computational and experimental systems in the range of 10^{-3} to 0.7, which corresponds to the Stokes regime). Our computational model focuses on pressure-driven flow, with a parabolic velocity profile and no slip at the surface (as imposed by a boundary condition). We used a finite-element method to numerically solve the coupled equations, due to the lack of an analytical model that is valid throughout the range of operational parameters that we wish to investigate. In the model, we used values of immunoassay parameters (microchannel dimensions, k_{on}, k_{off}, D, C_{so} and C_o) that resemble those of real-world conditions (see Materials and Methods for values of the parameters). Overall, our basic computational approach is conceptually similar to those of some previous finite-element studies [90] (rather than simplified two-compartment models [94]). We considered four different concentrations: three for the analyte (C_o in the bulk layer, C in the boundary layer, and C_s for analytes captured on the solid surface) and one for the surface-bound capture molecule (C_{so}) (Figure 5-1A).

In general, we used the surface concentration of captured analytes at the end of the assay (C_s) as a primary indicator of the performance of the assay, because it is directly related to the experimentally observed signal (such as fluorescence intensity). Since the concentration of captured analytes is highest at the beginning of the capture zone (as verified in our computational models), the C_s values we report are an average value over the capture zone. The performance of the assay can also be assessed in terms of saturation time, sample consumption [90], and capture fraction [92]; we will examine some of these parameters in our analysis, while focusing on C_s as the major criterion.

5.3.2 Modeling of capture of analytes without real-world constraints

In our first simulations, we examined how a change in flow rate Q would affect the amount of captured analyte C_s, under three sets of idealized operating conditions:

Under the first set of conditions, we simulated an assay with *unlimited supply of sample* and *unlimited time*, by fixing a constant concentration of analytes in the bulk layer (C_0 ~ 3.5×10^{-3} mol/m^3 and a long simulated time of assay (t ~10 hours). Under these operating conditions, changing the flow rate by four orders of magnitude (from 0.01 µL/min to 100 µL/min) resulted in no change in the final concentration of captured analytes (Figure 5-2A), as the surface-bound capture antibodies were saturated with analytes under all tested flow rates.

Next, we examined the operating condition of *unlimited supply of reagent* *within a fixed time interval* (t = 5 min) and with a *large capture zone* (L = 1.5 mm; in surface plasmon resonance assays, capture lengths of 2 or 3 mm are not uncommon). Increasing flow rate under these operating conditions increased the amount of analytes in contact with the capture zone; since the surface-bound capture antibodies was not saturated with analytes, increasing the flow rate also increased the final amount of captured analytes (Figure 5-2B).

In a third scenario, we simulated an assay where the *volume of sample is limited*, with *unlimited time* for the assay (i.e. the time of the assay is as long as necessary for the entire volume to be passed through the channel). Hence, the time of the assay is inversely proportional to the flow rate. Here, a slow flow rate resulted in high capture of analytes (Figure 5-2C), due to a high residence time for the analytes to be captured on the surface. In practice, however, one cannot run an assay at arbitrarily low flow rates, which correspond to long assay times, and may be construed to contradict an advantage in microfluidics that flow speeds up an assay and replenishes the boundary layer with fresh analytes [70, 92].

These finite-element simulations demonstrate three different and conflicting trends of amount of captured analytes as a function of flow rate, obtained under three different scenarios for operating a microfluidic-based heterogeneous assay (but with identical underlying physics).

These trends suggest that modeling of microfluidic heterogeneous immunoassays without a careful consideration of realistic operating conditions (as well as consideration of generic microfluidic advantages without proper consideration of the specific assay parameters) would likely fail to produce proper guidance for assay development and operation under real-world conditions.

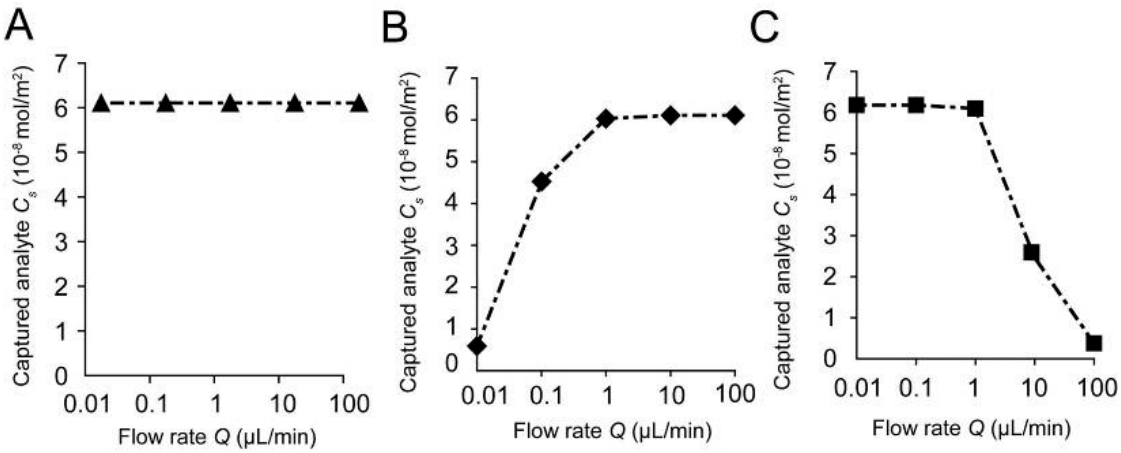

Figure 5-2: Captured analytes predicted by finite-element models as a function of flow rate, under three operating scenarios without real-world constraints. (A) Predicted trend with unlimited sample and unlimited time. The assay parameters were: L = 100 µm, L0 =100 µm, t = 60,000 seconds (to approximate unlimited time), C_{so} = 7x10^{-8} mol/m^2, Co = 10-5 mol/m^3 (10 nM), k_{on} = 240 m3/mol.s, koff = 3.5x10-3 s-1. **(B)** Predicted trend with an unlimited supply of sample within a fixed time (filled diamonds (◆) t = 3600 s) interval and large capture zone. The assay parameters were: L = 1500 µm, L_0 =100 µm, C_{so} = 7x10^{-8} mol/m^2, Co = 10 nM, kon = 240 m3/mol.s, koff =3.5x10^{-3} s^{-1}. **(C)** Predicted trend with finite sample volume (filled squares (■) V=15 mL) and unlimited time for the assay. The assay parameters were: L = 100 µm, L_0 =100 µm, t = up to 30,000 seconds (depending on the volume), C_{so} = 7x10^{-8} mol/m2, C_o = 10 nM, k_{on} = 240 m^3/mol.s, koff =3.5x10^{-3} s^{-1}.

5.3.3 Physical regimes of analyte-capture process

In microfluidic heterogeneous immunoassays, the analyte-capture process is typically viewed as "reaction-limited" (or "kinetically controlled")[88], whereas in multiwell plates – in which most analytes are very far from the capture zone, and replenishment of depleted analytes in the boundary layer relies on diffusion – analyte capture is viewed as "transport-limited" (or "mass transfer-controlled"). If the analyte-capture process is indeed reaction-limited, one would expect that flow rate has no effect except as it determines the incubation time, consistent with the

previous modeling results (Figure 5-2A and C). In a transport-limited case, the analyte-capture process is accelerated with increased convective flow, as confirmed by the previous finite-element simulations (Figure 5-2B).

Although the trends of Cs vs. Q are suggestive, how does one directly identify which physical regimes correspond to which operational parameters? We present a molecular perspective to identify the assay conditions that lead to different physical regimes. We note that operation of an assay in a transport-limited regime creates a boundary layer on the surface in which the concentration of analytes (Cb) is lower than the concentration of analytes in the bulk layer (Co), due to depletion of analytes in the boundary layer that are not being replenished by mass transport. By contrast, in a reaction-limited regime, Cb is close (and almost equal) to Co. Hence, by comparing the analyte concentration in the boundary layer Cb to Co, it is possible to identify if the assay is operating in the reaction-limited regime. In particular, we define Cb < 0.95Co as transport-limited, and Cb >0.95Co as reaction-limited. (Some studies have imposed boundary conditions where zero analyte concentration at surface is the condition for transport-limited regime 29, but we believe this condition is too restrictive for our system since mass transport would begin to limit the analyte-capture process well before the analytes in the boundary layer are completely depleted.) Hence, based on boundary conditions and constants defined by the user-defined assay parameters, one could solve the partial differential equations to identify the physical regime of operation.

The finite-element simulations provided snapshots of the concentration profiles inside the microchannel during the analyte-capture process (Figure 5-3A). The profile reveals, at each time point, the variation in concentration in solution occurs mainly occurs in the boundary layer (C_b) rather than in the bulk analyte (C0), as expected. In addition, two concentrations at the surface

are of note: concentration of captured analytes (C_s, in mol/m^2) and concentration of surface-bound capture molecules (C_{so}, in mol/m^2; this value is defined by the operator in the initial patterning of the molecules). Because the stoichiometry of binding between the capture molecule and analyte is fixed, the concentration of capture molecules Cso determines the maximum possible value of captured analytes Cs, and hence an upper bound for the signal in an assay.

We analyzed the ratio C_b/C_o for different values of C_{so} (Figure 5-3B). At low C_{so}, any depletion of analytes from the boundary layer due to capture of analyte on the surface is quickly balanced by transport of analyte from the bulk solution; hence C_b quickly reaches a concentration that approaches the bulk concentration C_o. In this regime, where C_b/C_o is close to 1, the analyte-capture process is limited by the surface reaction rather than transport of analytes from the bulk solution to the boundary layer, i.e. the operating regime is reaction-limited. For a larger number of surface-bound capture molecules (i.e. large C_{so}), saturation of the binding would require a larger number of analytes to move from the boundary layer to the surface, and hence higher transport of analytes from the bulk solution to the boundary layer; as a result, the choice of a large C_{so} by the operator of the assay would bias the analyte-capture process towards a transport-limited regime. At a critically large value of C_{so}, the analyte-capture process is no longer limited by the surface reaction, but rather by the transport of analytes from the bulk solution to the boundary layer, i.e. the operating regime is transport-limited. We define C_{so}* (red line in Figure 5-3B) as the upper C_{so} value at which $C_b/C_o > 0.95$. Below C_{so}*, we define analyte-capture process as reaction-limited ($C_b/C_o > 0.95$), and above Cso*, we define the process as transport-limited ($C_b/C_o < 0.95$). (The 95% cutoff is arbitrary and can be adjusted; also, there is likely an intermediate regime close to the boundary.) Hence, the C_{so}* value defines the boundary (i.e. the

limiting value of C_{so}) between reaction-limited and transport-limited regimes, as well as the maximum possible signal of the assay.

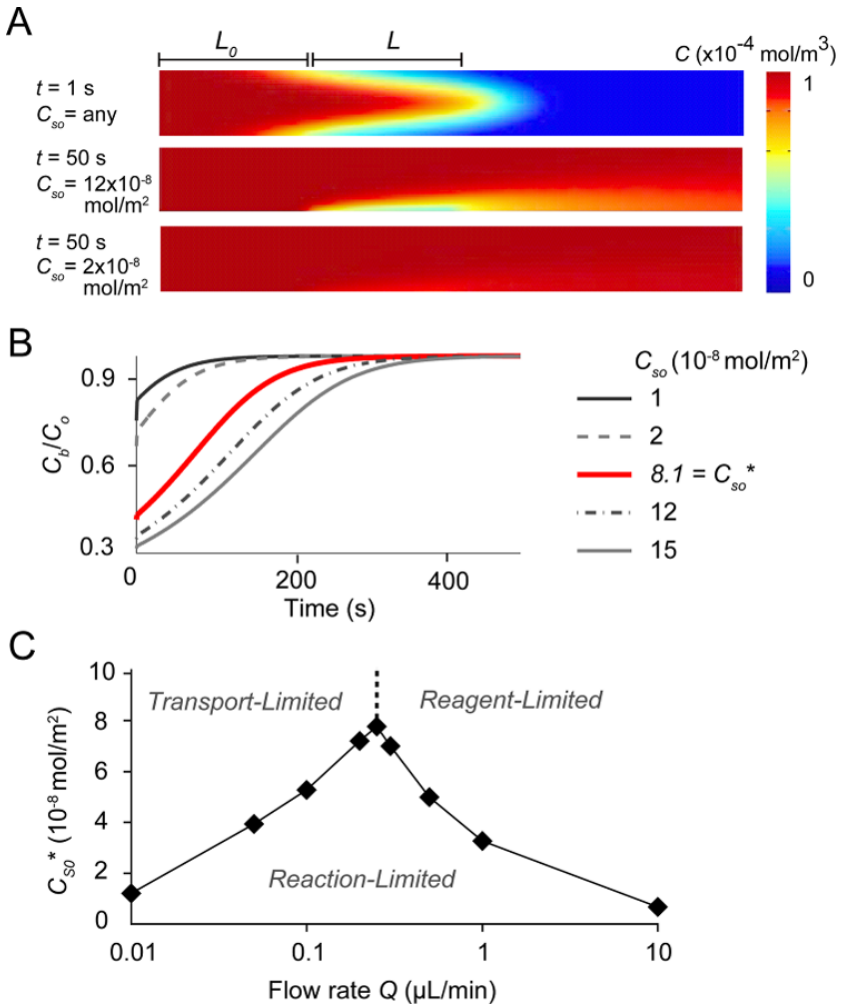

Figure 5-3: Identification of physical regimes in microfluidic heterogeneous immunoassays. (A) Concentration profiles of microchannels at the beginning of an assay, for case 1: Cso = 2x10^{-8} mol/m^2, and case2: C_{so} = 12x10^{-8} mol/m^2, for both cases the rest of the conditions are the same : Q = 0.25 µL/min, Co = 10^{-4} mol/m^3, kon = 240 m^3/mol.s, koff = 3.5x10^{-3} s-1. The capture zone is indicated as L. **(B)** Plot of C_b/C_o over time to determine C_{so}* value, which is the maximum C_{so} at which the time-averaged C_b/C_o is greater than or equal to 0.95. The time of the assay is set to a maximum of 20 minutes, or shorter if the entire volume (5 µL) of sample has passed through (i.e. at high flow rates). Shown here is a flow rate of 0.25 µL/min. **(C)** Plot of the limiting values of surface-bound antibody concentration (C_{so}*), an indicator of a reaction-limited regime, for various flow rates. The three physical regimes of transport-limited regime, reaction-limited regime, and reagent-limited regime are indicated. The peak of the graph is defined by the real-world constraints of fixed volume and finite time, e.g. here, at a flow rate of 5 µL of sample volume / maximum assay time of 20 mins = 0.25 µL/min.

Because increasing the flow rate Q increases convective flow and can help replenish any depleted analytes in the boundary layer, a high Q can increase the maximum amount of analytes that can be captured on the surface (C_{so}*). Thus, we examined C_{so}* as a function of Q (Figure 5-3C). In addition to the real-world constraint of "finite volume", we also imposed a "finite time" limitation (in our simulations, a maximum of 20 minutes). (A scenario of finite volume but unlimited time is unrealistic: the assay has a long time to reach saturation at very low flow rates, as the assay operates in a transport-limited regime for a long time but eventually reaches a reaction-limited regime, see Supplementary Information.) The finite-element simulations show an initial increase in C_{so}* as Q increases, followed by a decrease in C_{so}* for very high Q (Figure 5-3C). This result stands in contrast to the expected relationship for models under idealized operating conditions (e.g. with an unlimited volume and amount), where C_{so}* increases monotonically and indefinitely as Q increases (increasing Q would always increase mass transport of analytes to the boundary layer, which would permit indefinitely higher C_{so}* values). Instead, under real-world constraints of finite sample, volume and amount, we identify a third regime – the reagent-limited regime, which exists at high flow rates and only under a finite volume constraint (Figure 5-3C). Given finite sample volume, assays at high flow rates are completed very quickly, such that the capture of analytes is limited neither by the rate of transport (since $C_b/C_o \sim 1$) nor the rate of reaction at the surface, but rather by the availability of reagents.

5.3.4 Simulation under real-world constraints: finite volume and time

Next, we investigated the effect of varying assay parameters on the capture of analytes C_s under the real-world constraint of finite volume of sample. (To satisfy the condition of finite assay time, we used a C_o of 100 nM to speed up analyte capture. All simulated assays here take

place in less than 20 minutes, except for Q=0.01 μL/min). The finite-element simulations show that the captured analyte C_s plateau at low Q and decrease at high Q: at low Q, the long assay time provides enough time for the analyte to diffuse to the surface to saturate binding to the surface, and at high Q, the assay operates in a reagent-limited regime which limits the maximum signal (Figure 5-4A). In practical terms, these results suggest that for low C_{so}, the assay can be run at a higher Q (and hence achieve a faster assay) and still occupy large percentage of the binding sites; for high C_{so}, the flow rate needs to be lowered (and hence slower assay) to saturate the surface. Hence, this graph suggests that one should operate the assay at a flow rate Q^* (around 0.5 μL/min in our models), where Q^* is the maximum flow rate that results in saturation of the surface, in order to achieve the maximum signal with the fastest possible time. Below Q^*, one is not gaining any appreciable signal while slowing down the assay, and above Q^*, the assay will not reach the maximum signal but will run faster. Hence, above Q^*, the operator makes an informed decision in trading off signal with time.

5.3.5 Effect of dilution into larger plug volume: fixed amount

In many diagnostic assays (including point-of-care assays), a sample is often diluted before it is introduced into the test (for example, to reduce its viscosity, or to introduce the analytes into a controlled buffer environment [76, 95]). Which type of sample would result in a larger amount of captured analytes – a short concentrated plug or a long dilute plug? According to the metric of concentration × time, which is valid for initial binding events with first-order kinetics and where the off-rate is negligible (i.e. the integrated form of $dC_s/dt = k_{on}C$), the two types of samples should achieve identical signals in the assay because the amounts of analytes passing over the capture zone are equal.

Under real-world conditions, however, dissociation of captured analytes is important, and *C* changes significantly depending on the conditions of finite sample volume and finite assay time. Interestingly, the finite-element results reveal that the short concentrated plug (5 µL of 100 nM) results in more captured analytes than a long dilute plug (50 µL of 10 nM) (Figure 5-4C): therefore, the larger volume of the plug does not appear to fully compensate for the decreased concentration in terms of promoting binding of analytes to the functionalized surface. Moreover, we found that if the interaction between the analyte and capture molecule is very strong (i.e. k_{off} is considerably smaller than $Co \times k_{on}$), the signal at the end of the assay for both dilute and concentrated plugs reach the same maximum value. Even in these cases, however, since dilute samples take longer to run, it is more advantageous to use concentrated samples.

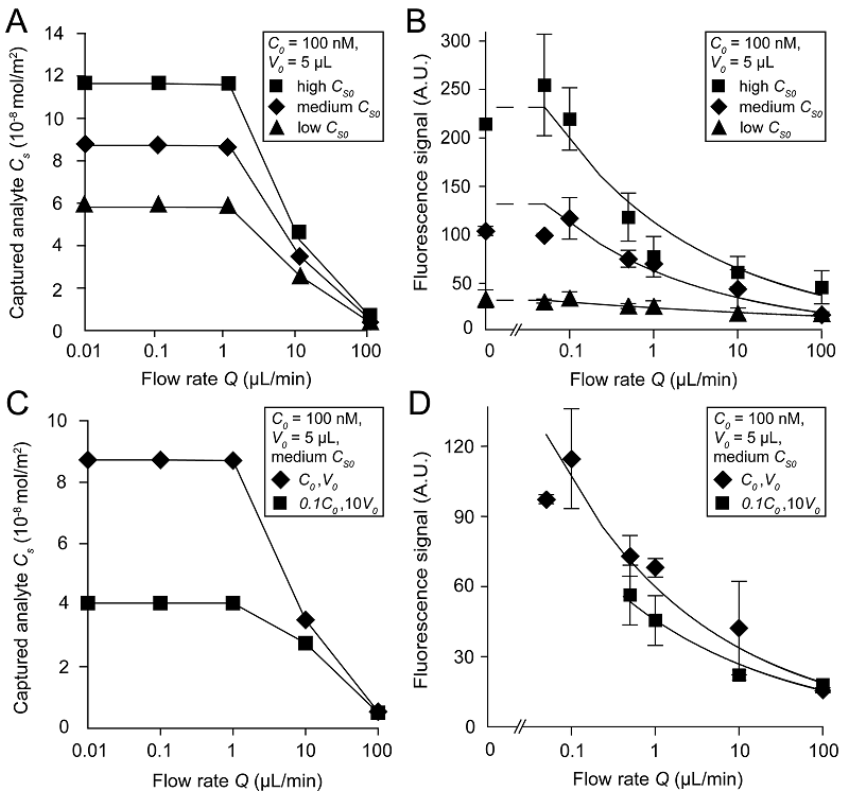

Figure 5-4: Concentration of captured analytes C_s predicted by FEM and also experimental microfluidic binding assays as a function of flow rate Q, under the real-world constraints of finite volume (5 mL). At the simulated flow rates in this figure (except for Q=0.01 mL/min), the actual time of the assay is less, since the entire plug of sample passes through the channel before the maximum allowable assay time (20 min). (A) Plot

of C_s as a function of Q, at high, medium, and low C_{so} values ((■) 1.33 x 10^{-7}; (◆)10^{-7}; (▲) 0.67 x 10^{-7} mol/m^2), as obtained by finite-element analysis. **(B)** Corresponding experimental results of fluorescence signal (arbitrary units) of captured analytes as a function of Q, at different relative values of C_{so} (described in relative terms according to incubations in solution concentrations of 133 nM, 1.3 μM, and 13 μM and incubation times of 1.5 hours for low and medium, and overnight for high). **(C)** Plot of C_s as a function of Q for a short concentrated sample plug vs. a large dilute sample plug, i.e. a "fixed amount" simulation. The case of a relatively large k_{off} is shown here. Values of C_o are: 100 nM (◆), 10 nM (■), and 1 nM (▲). **(D)** Corresponding experimental results of fluorescence signal (arbitrary units) of captured analytes as a function of Q, under the real-world condition of fixed amount but different concentrations and volumes (*e.g.* 5 μL of 100 nM or 50 μL of 10 nM analyte). Fitting of the experimental results in (B) and (D) contain: 1) best-fit lines (solid) describing assays run under continuous flow; these interpolations take the form $y = a^{-bx}$, where a and b are constants, x is flow rate (in μL/min), and y is fluorescence signal (in A.U.); 2) fluorescence signals from assays performed at conditions that approach static flow (*i.e.* zero flow rate); 3) interpolations (dashed lines) to the static flow data points.

5.3.6 Experimental Microfluidic Binding Assays

We first studied the effect of flow rate Q on the concentration of captured analytes C_s (which is directly proportional to the fluorescence signal). To determine whether differences between groups were statistically significant, we performed one-way ANOVA on data sets obtained by varying C_{so} or Q (Figure 5-4B). Using an α value of 0.05, the analysis confirmed that the differences in fluorescence intensities at different Q were statistically significant for low C_{so} (p-value = 1.2×10^{-3}), medium C_{so} (p-value = 6.4×10^{-5}), and high C_{so} (p-value = 2.4×10^{-7}), and the differences in fluorescence intensities between assays run with different C_{so} were statistically significant at all flow rates of 0.05 μL/min (p-value = 1.3×10^{-5}), 0.1 μL/min (p-value = 4.6×10^{-6}), 0.5 μL/min (p-value = 1.6×10^{-3}), 1 μL/min (p-value = 4.9×10^{-3}), 10 μL/min (p-value = 3.4×10^{-2}), and 100 μL/min (p-value = 4.9×10^{-2}). Consistent with the interpretation of the finite-element simulations, the experimental binding assays suggest that to achieve the maximum signal under fastest possible time, one should operate the assay at a critical flow rate Q^*, and one can run the assay even faster by increasing Q but at the expense of signal, since the fluorescence signal decreased at high flow rates (Figure 5-4B).

We observed a greater variance in signal for assays run with high C_{so} (Figure 5-4B). One explanation may be that the coating conditions at high C_{so} led to greater heterogeneity in

coverage of surface-bound antibodies, possibly due to formation of local clusters and multilayers [75, 96]. In addition, we observed a greater variance in signal for assays run at low flow rates (Figure 5-4B). This variation likely arose in part from limitations in operating the syringe pump reproducibly at low flow rates, as we also observed that the measured flow rates agreed less with their set flow rates at lower speeds than at higher speeds (data not shown).

Next, we studied the effect of diluting the sample plug into a proportionally larger volume (*e.g.* from 5 μL at 100 nM, to 50 μL at 10 nM) on the amount of captured analyte. Consistent with the finite-element simulations (Figure 5-4C), we observed a decrease in fluorescence signals for the diluted samples across all flow rates (Figure 5-4D). The differences in fluorescence intensities between the two dilutions were statistically significant for runs at a flow rate of 1 μL/min (p-value = 1.4×10^{-2}), but not at other flow rates. (Although we expect, from the simulations, clear difference in signals between the sample dilutions at lower flow rates, there is experimental error in controlling low flow rates, as explained above. Additional sources of experimental errors include variations in C_{so}, and possible nonlinearities in fluorescence signal vs. concentration of captured analyte.) Also, ANOVA confirmed that the differences in observed fluorescence intensities for assays run with different Q were statistically significant (p-value = 6.5×10^{-3}), as predicted by the simulations. Overall, these results are consistent with the predictions of sample dilutions from finite-element modeling results, and suggest that a short concentrated plug of sample produces a higher signal than a long dilute plug.

Finally, we note that from finite-element simulations under a "finite time" constraint that ends the assay before the entire volume of the sample has passed through (Figure 5-4), that assays at low flow rates will spend large amounts of time in a transport-limited regime. In the experimental assays, when we imposed a finite assay time, cases of dilute samples which did not

pass completely through the channel at the set flow rate (*i.e.* below 0.5 μL/min, which require a long assay time for the entire sample volume to pass through) showed a decrease in signal compared to dilute samples which passed completely through at the set flow rate (*i.e.* at or above 0.5 μL/min), consistent with the finite-element simulations.

5.3.7 Inherent transport limitation in conventional microfluidic: vortex-like flow as a remedy

Laminar flow in microfluidic systems hinders the mass transport of analytes from the bulk solution to the surfaces of microchannels; hence, slowing down the analyte capture in heterogeneous immunoassays. Numerous, techniques have been proposed to enhance mass transport to the surface of microchannels (e.g. applying electric, magnetic or centrifugal force). Yet, due to the implementation complexities and other fundamental setbacks (e.g. interference with mass action law), these techniques are not widely used. We hypothesized that creating a localized vortex-like flow will enhance the transport of analyte toward the binding sites, increasing analyte capture significantly. An effective method is introduction of immiscible fluid vesicle (e.g. air bubble) to the microchannel. Air bubble disrupts the laminar flow locally and creates the desired vortex-like flow. Relatively simple integration of bubble generators with the existing microfluidic-based diagnostic systems and extensive characterization of these systems (e.g. T-junction bubble generator) highlight this approach as an effective candidate to address analyte transport problem.

Finite element method is used to simulate two-phase flow as described in the Methods.

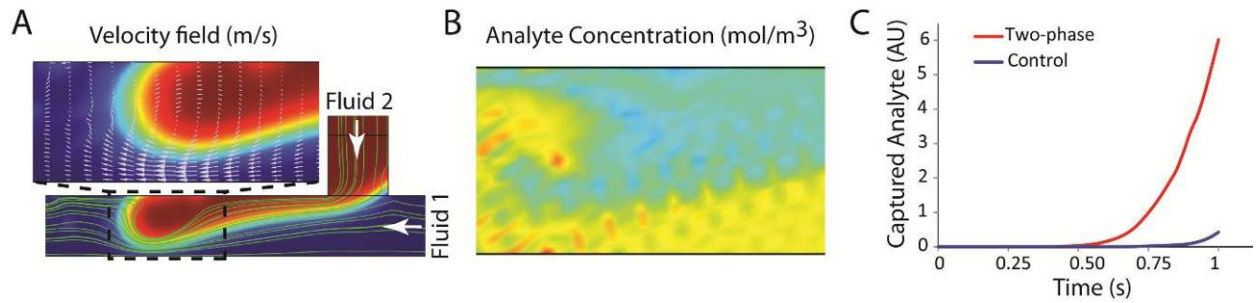

Figure 5-5: Two-phase flow. (A) Velocity field indicates enhanced transport closer to the surface (larger vector) which enhances analyte transport to the binding sites. **(B)** Uniform and increased analyte concentration close to the boundary **(C)** amount of captured analyte vs time for the two cases of two –phase and control flow

We simulated bubble flow in a T-junction microchannel by simultaneous solution of level set function and Navier-Stocks. Figure 5-5A shows two immiscible fluids interface and the resulting tortuous streamlines. A closer look shows a dramatic velocity increase at the tip of the bubble compared to the bulk of the flow. This causes the excessive analyte replenishment on the capture area. Then the result of simulation (velocity field) is used to solve the convection-diffusion and reaction simultaneously. The mixing caused by vortex-like flow cause the analyte concentration to be replenished more effectively close to the binding area; hence, creating a more homogenous analyte concentration diminishing the boundary layer height (Figure 5-5B).

To study the effect of this flow pattern, we compared the capture efficiency of two cases, two-phase (bubble) flow and control (bubble-free) flow. Figure 5-5C shows the amount of captured analyte vs. time for the two cases of two –phase and control flow. The amount of captured analyte dramatically increased with the introduction of the bubbles into the system. We specifically focused on the initial period of the assay, since the transport-limited regime mainly happens at this time period (straight line in the sigmoidal curve [97]).

5.3.8 Gold-silver signal enhancement

We also analyzed the kinetics of gold-silver signal enhancement under a range of surface gold density and silver development time in order to minimize total assay time in immunoassays developed and evaluated *on-the-field*. The kinetics of silver reduction reveal a sigmoid-shaped response, with the presence of an induction period followed by rapid growth of signal and termination of signal growth (Figure 5-6d). For curve fitting, we used a variation of the four parameter logistic equation,

$$OD = OD_{min} + \frac{OD_{max} - OD_{min}}{1 + e^{a*(t_{OD,mid} - t)}}$$

where OD, OD_{min}, OD_{max} are the optical density, minimum and maximum values respectively, t is time of silver reduction and $t_{OD,mid}$ is the time at point of inflection, and a is a curvature parameter (Figure 5-6b). (Curve fitting was performed using GraphPad Prism software for nonlinear regressions; see Fig. 6a for parameter values). R-squared values for best-fit curves were 0.92 (anti-goat IgG Ab only), 0.99 (1:1 anti-goat IgG Ab:BSA), 0.99 (1:2), 0.96 (1:4), 0.96 (1:8), and 0.71 (BSA only).

a

	anti-goat Ab : BSA physisorbed ratio					
	1:8	1:4	1:2	1:1	Ab only	BSA only
t_OD,mid (min)	11.0	7.2	6.8	5.8	4.3	11.0
a	0.315	0.455	0.528	0.570	0.813	0.656
OD,max	0.324	0.307	0.356	0.360	0.351	0.145
OD,min	-0.013	-0.016	-0.014	-0.018	-0.014	0.002
OD,mid	0.156	0.145	0.171	0.171	0.169	0.074
t_n (min)	**5.7**	**3.7**	**3.6**	**3.0**	**2.2**	**8.0**
f_anti-goat Ab (%)	**11**	**20**	**33**	**50**	**100**	**0**
S_Au,i (10^-8 mol NP / m^2)	**0.37**	**0.66**	**1.10**	**1.65**	**3.30**	**0.00**

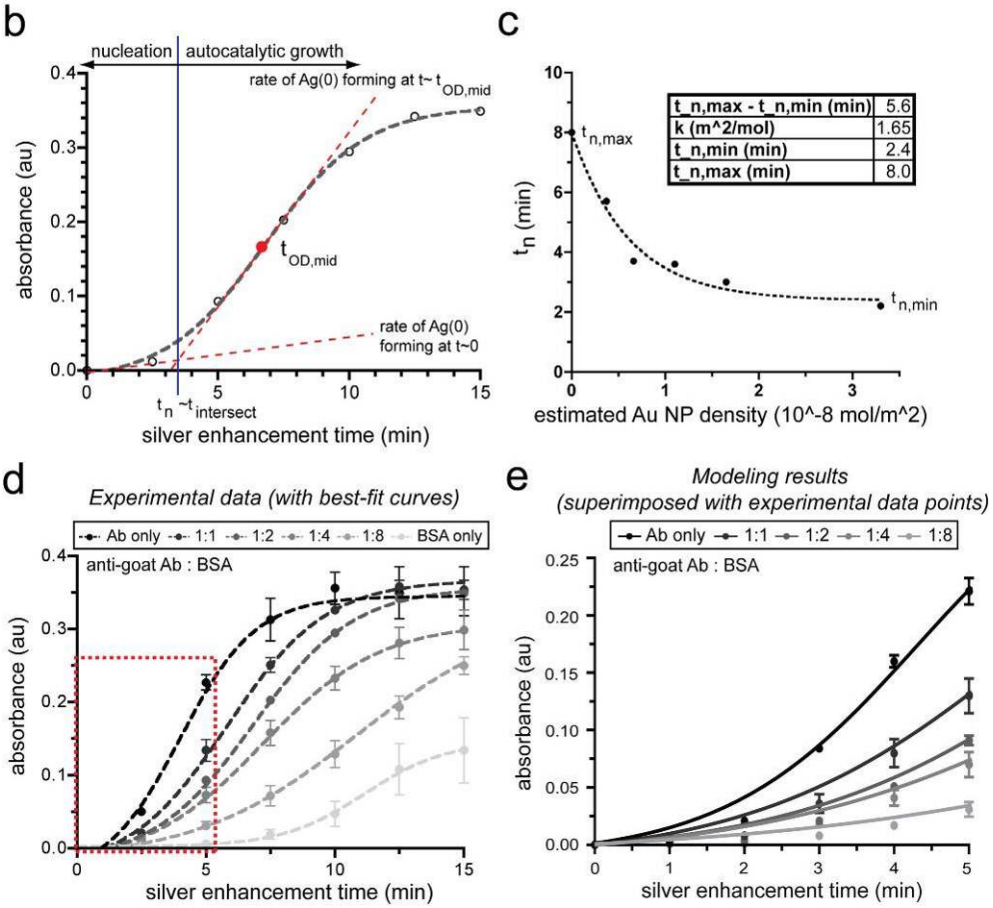

Figure 5-6: Modeling of silver development. a, Parameters for modeling silver reduction. tOD,mid, a, ODmid, ODmin, ODmax and tn are determined from best-fit curves from experimental data; fragAb and SAu,I are estimates based on literature. b, Silver enhancement of zone functionalized with 1:2 anti-goat Ab:BSA physisorption ratio. Data points are mean absorbance values, and dashed line is best-fit curve (four parameter logistic equation). Parameters are indicated accordingly. c, Dependence of tn on gold nanoparticle density captured on the surface, with best-fit curve (exponential decay) as dashed line and best-fit parameters listed in adjacent table. d, Experimental kinetic data of silver enhancement for various anti-goat IgG Ab:BSA physisorption ratio. Data points indicate mean values, error bars indicate one s.d. Dashed lines are best-fit curves. e, Computational modeling results (solid lines) superimposed with experimental data points. The difference (expressed as normalized objective function) between the model and experiment is 9.2%.

Together with the development of silver precipitates (established by AFM [79, 98] and SEM [99] in related systems), the silver reduction is believed to start similarly with the catalytic formation of *in situ* silver nanoclusters around gold particles [100, 101] and undergo a general mechanism involving a nucleation step followed by a autocatalytic surface-growth step [102, 103]:

$$\mathrm{Ag(I)} \xrightarrow[\text{Au, reductant}]{k_1} \mathrm{Ag(0)} \qquad \text{nucleation}$$

$$\mathrm{Ag(I) + Ag(0)} \xrightarrow[\text{reductant}]{k_2} \mathrm{2Ag(0)} \qquad \text{autocatalytic growth}$$

(The mechanism for the termination of signal growth may be due to non-linearity between absorbance and silver at high silver density, or reduced silver deposition due to agglomeration of nanoclusters to catalytically-inactive bulk metallic silver [102, 103].)

We focused on the first 5 minutes of silver reduction, during which sufficient signal is generated and where nucleation and autocatalytic growth are prominent (Figure 5-6d, *box outlined in red*). We assume excess reducing agent (*e.g.* hydroquinone), irreversible reactions, fast adsorption of reactants onto gold surface, even distribution of gold density across the detection zone, and negligible silver precipitate desorption. Based on this reaction mechanism we formed the following rate of silver formation:

$$\frac{d}{dt}[Ag(0)] = k_1 S_{Au}[Ag(I)] + k_2 [Ag(I)][Ag(0)] \qquad (19)$$

with rate constant of nucleation (k_1), rate constant of growth (k_2), concentration ([ ]), and active surface density of gold catalyst S_{Au} (in units of moles of gold nanoparticles per square meter of substrate surface). Due to attachment of silver precipitate around gold nanoparticles,

the number of active catalytic sites on the gold nanoparticles diminishes as the reaction progresses. We therefore express S_{Au} as a function of initial gold surface density bound ($S_{Au,i}$) and the extent of nucleation reaction, ξ

$$S_{Au} = S_{Au,i}(1-\xi)$$

To estimate $S_{Au,i}$, we assumed (1) equal rates of physisorption between anti-goat IgG antibody and BSA, (2) a surface density of 0.5 μg/cm^2 of anti-goat IgG antibody (with molecular weight 150 kDa) for the antibody-only experimental condition [104], (3) a 1:1 capture ratio of anti-goat IgG antibody to gold-conjugated goat-anti-human IgG antibody, (4) a 1:1 labeling ratio of gold nanoparticle to goat-anti-human IgG antibody conjugate. Values of $S_{Au,i}$ for each experimental condition are given in Figure 5-6a. To relate the amount of captured antibody with $S_{Au,i}$, we used an average gold nanoparticle diameter of 10 nm:

$$S_{Au,i} = f_{ragAb} * 3.3x10^{-8}$$

where f_{ragAb} is the percentage of anti-goat antibody (relative to total protein) in the physisorption solution, and $S_{Au,i}$ is expressed.

For estimating ξ, we define a time t_n, beyond which negligible silver is formed from nucleation on gold nanoparticles (i.e. since all the surfaces of gold nanoparticles are already covered by reduced silver), by finding the intersection between lines tangent to best-fit curve of reduced silver formation at $t_{OD,mid}$ and t~0 (Figure 5-6b). We then express active catalyst surface area as

$$S_{Au} = S_{Au,i}\left(1-\frac{t}{t_n}\right)$$

The dependence of t_n on gold nanoparticle density captured on the surface is shown in Figure Figure 5-6c; we generalize the relationship with an exponential decay fit

$$t_n = (t_{n,\max} - t_{n,\min})e^{-k*S_{Axi}} + t_{n,\min}$$

where $t_{n,\,max}$, $t_{n,min}$ are t_n at 100% and 0% of anti-goat antibody surface coverage and k is a curvature parameter. R-squared value is 0.97.

We modeled the effect of flow parameters on the kinetic of reduction, by coupling the convection/diffusion equation with the rate of silver formation at the boundary layer using weak-form formulation (and assuming a parabolic velocity profile in the microchannel):

$$\frac{\partial}{\partial t}[Ag(I)] + \nabla \cdot (-D_{Ag(I)}\nabla[Ag(I)] + [Ag(I)]u) = -\frac{d}{dt}[Ag(0)]$$

$$u = u_0\left(1 - \left(\frac{y - 0.5}{0.5}\right)^2\right)$$

with diffusion constant $D_{Ag(I)}$ (1 x 10^{-10} m^2-s^{-1}), flow rate Q (5 x 10^{-11} m^3-s^{-1}), channel height h (50 x 10^{-6} m), channel width w (100 x 10^{-6} m), velocity u and max velocity u_0 (= 3*Q/(2*h*w)), and initial concentration of Ag(I) (0.01 mol-m^{-3}).

We then tuned the parameters by comparing the model output with the experimental data for 5 different gold concentrations. Nucleation rate constant (k_1) and autocatalytic rate constant (k_2) were determined according to minimization of the model error. There are several optimization algorithms available to minimize the magnitude of an objective function (*e.g.* the sum of the errors between the model output and the experimental data over time and over the five different gold concentrations). We chose "*pattern search algorithm*" (Direct search toolbox, Matlab) since it handles the constrained nonlinear optimization problems in a reasonable timeframe and does not require the function to be differentiable and continuous. Minimizing the objective function,

we determined the nucleation rate constant (k_1) and autocatalytic rate constant (k_2) to be 10^{-6} s^{-1} and 20 $m^3mol^{-1}s^{-1}$ respectively. (We converted silver surface density to optical density by assuming a linear relationship with scaling factor of $\frac{OD_{t=5min}}{[Au(0)]_{t=5min}}$).

Figure Figure 5-6d-e compares modeling results (after optimization of rate constants; *solid lines*) with experimental results (*filled circles*; error bars indicate one standard deviation) for silver enhancement over five minutes at different surface densities of captured gold nanoparticles. To determine the goodness of fit between model and experiment, we normalized the objective function by the total integral of the experimental curves over the five gold concentrations. The difference (expressed as normalized objective function) between the model and experiment is 9.2%.

5.4 Discussion

Previous modeling studies on microfluidic heterogeneous immunoassays have investigated the effect of flow rate, analyte-antibody binding constant, and analyte concentration on capture fraction [90], the effect of microfluidic channel geometry on capture fraction [91], and limiting physical regimes [92]. In this study, we use finite-element analysis to computationally solve three partial differential equations that describe the three central physical processes. We found that simulations under real-world constraints led to different results than simulations under idealized conditions, with the key findings confirmed in trends and magnitudes by experimental binding assays. In applying the results to providing practical considerations for designing and operating a microfluidic immunoassay (summarized in Conclusion), we noted that attempts to simultaneously apply all microfluidic advantages (such as fast assay, low sample consumption, and large signal-to-noise) can obscure the desired optimal assay parameters.

In this study, we focused on finite sample availability and finite assay time as the relevant constraints imposed by real-world conditions of operating microfluidic immunoassays. Additional real-world constraints exist: for example, h or L can be optimized for analyte capture, but they can increase fluidic resistance to impractical levels for pressure-driven flow.

Limitations of this study include: 1) The study focuses on pressure-driven flow, although some of the results may be relevant for microfluidic heterogeneous immunoassays using electrokinetic flow or for other heterogeneous assays such as surface plasmon resonance [93]; 2) The amount and binding activity of passively adsorbed capture antibodies were not directly verified; 3) Non-specific binding was not explicitly taken into account.

5.5 Conclusion

Using theoretical modeling and experimental binding assays, we examined the effect of varying assay parameters on the capture of analytes in microfluidic-based heterogeneous immunoassays under real-world operating conditions, and we also analyzed the kinetics of signal enhancement from gold-catalyzed reduction of silver. The finite-element and experimental results were consistent, and the study on analyte capture process revealed trends that are not necessarily intuitive according to generic considerations of microfluidic advantages. For the operator of microfluidic-based heterogeneous immunoassays, some conclusions (based on the real-world constraint of finite sample volume and finite assay time) include:

1) Which flow rate? One should operate at or above the critical flow rate Q^* (e.g. 0.1 to 1 μL/min under our assay conditions) needed to maximize the signal. Below Q^*, one is running a longer assay but is not gaining any signal. Above Q^*, the user can make an informed choice in trading signal *vs.* time, in that a higher flow rate (i.e. faster assay) will result in lower signal (due to being in a reagent-limited regime).

2) What sample concentration? To achieve maximium signal, one should use a short concentrated plug rather than a long dilute plug (e.g. 5 µL of 100 nM, vs. 50 µL of 10 nM).

Moreover, we studied the effect of integrating two-phase flow in the conventional microfluidic system to overcome its inherent transport limitation due to laminar flow. We found that vortex-like flow enhances transport at the proximity of the binding sites; hence, increasing analyte capture. The simplicity of integrating bubble generator with the conventional microfluidic systems, makes it an interesting alternative for increasing binding efficiency.

Chapter 6 Conclusion

Studying interaction of biological elements at the microscale is critical in understanding emergent properties of biological systems at the macroscale. Microtechnologies, which emerged out of semiconductor industry, hold great promise for manipulating biological species and their environment in a high-throughput fashion at micron scale precision. In this thesis, by leveraging microtechnologies, we studied the complex interaction of micron-sized biological elements in development and disease.

In the first half of this thesis, we studied the development (morphogenesis) of vascular tissue (vasculogenesis - the *de novo* formation of vascular networks from dispersed endothelial cells). Using microtechnologies, we developed a methodology to pattern an array of equally-spaced individual endothelial cells on a naturally derived ECM (Matrigel) to study their self-assembly into capillary-like structures (CLS). We tracked the morphologies and motilities of ~300 human endothelial cells, distilling the dynamics of tissue morphogenesis into an array of ~36,000 numerical phenotypes. Quantitative analysis of population averages revealed that vasculogenesis happens in five distinct and reproducible phases, two of which were previously unknown: *Spreading* in which the cells spread before forming connections with neighboring cells and *plexus stabilization* where the microvascular plexus stabilized before spatially reorganizing (Chapter 2). Analysis at the single-cell level showed that in contrast to the population-averaged behavior, most cells followed distinct temporal patterns that were not reflected in the bulk average. Interestingly, some of these behavioral patterns correlated to the cells' final structural role within the plexus (Chapter 3). Following the initial characterization of the cell-to-cell variation and identifying the dominant patterns of cell motility, we sought to identify the

underlying intercellular communication mode in deriving the process of CLS formation and creating distinct cellular behavior. We developed a methodology to decipher the roles of mechanical cues in directing the migration of endothelial cells in the early stages of vasculogenesis. We discovered that the role of ECM-mediated mechanical signaling in directing the process of CLS formation intensifies over time (Chapter 4). Knowledge of how individual cells or groups of cells behave enhances our understanding of how native tissues self-organize and could ultimately enable more precise approaches for engineering tissues and synthesizing multicellular communities. This methodology could be more broadly applied to the single-cell studies in the formation of other tissue types.

In the second half of this thesis we focused on leveraging microtechnologies in tackling major challenges in disease.

First, by introducing microfluidic-based diagnostics as a successful example of application of microtechnology in directly affecting the global health in the poor regions of the world, we studied the performance of these test, which is directly related to their amount of captured antigens in the sample, under real world constraints. Using theoretical modeling and experimental binding assays, for the operator of the microfluidic assay we sought to find the answers for questions such as: at what flow rate and sample concentration the assay should be run? We specifically found: 1) a ‘‘reagent-limited’’ regime which exists only under the constraints of finite sample volume and assay time; 2) a critical flow rate (e.g. 0.5 $\mu L.min^{-1}$ under our assay conditions) to gain the maximum signal with the fastest assay time; 3) an increase in signal by using a short concentrated plug (e.g. 5 μL, 100 nM) rather than a long dilute plug (e.g. 50 μL, 10 nM) of sample; 4) the possibility of spending a considerable fraction of the assay time out of the reaction-limited regime. Overall, an improved understanding of fundamental physical

processes may be particularly beneficial for the design of point-of-care assays, where volumes of reagents and available samples are limited, and the desired time-to-results is short.

Application of Microtechnologies in tackling challenging problems in disease is much broader than microfluidic-based diagnostics. In the appendices A and B, we presented two microfluidic platforms for the *in vitro* and *in vivo* study of heterotypic cell-cell interactions. These platforms will ultimately be used to accurately identify cancer drugs' efficacy across genetically heterogeneous panel of cancer cells. Together, these methods provide a powerful suite of tools for high-throughput analysis of biological species at micron scale and could potentially unlock the mysteries behind the emergent properties observed at the macro-scale.

Appendix 1. To develop a real-time microfluidic system for studying mammalian cells in 3D microenvironments

1.1. Introduction

In this appendix we demonstrate a microfluidic chip for studying the real-time growth and communication of systems of cells in three-dimensional (3D) microenvironments. This chip contains a 4 by 4 array of individually addressable microchambers, inside which small groups of mammalian cells are grown. By turning on and off sets of microvalves, the 3D extracellular microenvironment inside each chamber, along with the interconnecting pathways that connect the cell chambers, can be modified independently and in real time.

The development of microfabricated systems for biological applications has resulted in methods that allow for exquisite control over cellular microenvironments [105-107]. For example, cells can be spatially positioned to micron resolution, and chemicals can be delivered to cells to subcellular spatial resolution [6-8]. Many different cell types (including bacteria and mammalian cells) can be routinely grown and patterned inside a poly(dimethylsiloxane) (PDMS) microchip, but typically on flat 2D surfaces [108-110]. Recent studies indicate that for many biological processes (such as fibroblast motility, progression of melonoma tumors, and the polarity and differentiation of mammary epithelial cells), 3D microenvironments may mimic physiological context better than 2D surfaces in terms of cell morphology, adhesion, proliferation, and migration [111-113]. Whereas bulk 3D extracellular matrices (ECM) (such as collagen I, Matrigel, alginate, hyaluronic acid, agarose, gelatin, and acrylate-based hydrogels) are commonly used *in vitro* systems for providing mechanical and chemical stimulation to cells, studies of mammalian cells in microfabricated 3D matrices are only emerging. These studies

include the encapsulation of cells in microchannels to mimic tissue architecture and to study mammalian cells in perfusion cultures [114-120].

Our technical approach uses pneumatically actuated microvalves, which were previously developed by the groups of Quake and others [105, 121, 122] for a broad range of applications, including the analysis of live cells (such as cell sorting and long-term monitoring of bacteria). In this work, we aim to use microfluidics to impart real-time, dynamic control over the 3D environments of an array of mammalian cells while also incorporating the ability to study chamber-to-chamber communication of diffusible factors. Specifically, we aim to develop microvalves to study mammalian cells in 3D environments (to enhance biological relevance, we focus on Matrigel, a naturally derived ECM that is used to study cells in 3D [123-125]), and to demonstrate their use for studying long-term culture of undifferentiated mouse embryonic stem cells.

1.2. Methods

1.2.1. Device design and fabrication

We designed a microfluidic device composed of two layers of PDMS elastomer: a fluidic flow layer on the bottom, and a pneumatically-actuated control layer (filled with air or water) on the top, with the two layers separated by a 5 to 10 µm-thin PDMS membrane (Fig. A1-1). In the fluidic flow layer, channels were 100 µm wide, whereas microposts and chambers were 20 µm and 200 µm in diameter, respectively; this geometry of the chamber along with the microposts prevented the 3D gel from being displaced from the chamber. In the pneumatic control layer, channels over the actuation areas were 140 µm wide. In addition, in the pneumatic control layer, we designed ring-shaped valves over the chambers to create shallow conduits above 3D gels for rapid media perfusion; these valves were 40 µm wide and 100 µm in diameter. Due to their

thinner width than the regular actuation valves, the ring-shaped valves do not deflect completely to the bottom of the fluidic channel under standard operating pressures (from 20 to 50 psi).

We fabricated both layers of PDMS using soft lithography followed by replica molding. [121, 126] We designed photomasks using CleWin (WieWeb Software, the Netherlands) and printed them at a high resolution using a commercial service (20,000 dpi; CAD Art Services Inc.). The master for the pneumatic control layer was fabricated using a 15 µm-tall layer of epoxy-based negative photoresist SU8-2015 (MicroChem, Newton, MA) on a silicon wafer. The master for the fluidic flow layer was fabricated using an 18 µm-tall positive photoresist SPR220-7 photoresist layer; after development, we re-flowed the photoresist by heating the wafer on a hot plate at 140°C for 15 minutes to form channels with a round geometry (thus allowing complete closure of the channel upon actuation of valves). Both masters were then exposed to a vapor of trimethylchlorosilane for 1 hour (to aid PDMS removal), and replica molded with PDMS (Dow Corning Sylgard 184) made from a 10:1 ratio of base to curing agent; the PDMS mold was thick (~0.5 mm) for the pneumatic control layer, and thin (~30 µm; spin-coated at 2500 rpm for 1 min) for the fluidic flow layer. We treated the two PDMS layers with oxygen plasma, and very gently aligned the two layers using a microscope with the aid of 16 alignment marks built into the two layers. We finished the alignment within 2 minutes, such that the PDMS surfaces remained hydrophilic; once aligned, compression by hand of the two pieces irreversibly bonded the two layers. The two PDMS layers were placed on a hotplate at 90°C for 15 minutes to facilitate bonding. Then, the two layers were cut out from the wafer and interconnecting holes were punched through. Finally, the resulting device was mounted onto a clean glass slide with the channel side facing downwards under the assistance of oxygen plasma treatment for 1 min, and

then heated on a hotplate at 95°C for 15 minutes. The assembled microchip is shown in Figure A1-1B.

To set up the equipment for operating the valves, we connected a compressed nitrogen gas tank to a splitter, then to two tubing manifolds, split into voltage-gated solenoid valves (Lee Co, LHDA2433115H) to form multiple independent pressure sources, and then connected to the microfluidic chip via polyethylene tubings. This configuration allowed the valves in the control layer to be individually controlled. We operated the microvalves either by manually connecting the voltage switches on the breadboard where a compressed nitrogen tank can be placed nearby, or by manually applying positive pressure via syringes (for example, in the cold room); in all cases, the control layer was filled with water. We have also used a LabVIEW program to control the voltage-gated solenoid valves using a digital acquisition card (AT-DIO-32HS, National Instruments) for high-speed operations of a microfluidic chip containing a 10 x 10 array (unpublished results).

1.2.2. Culture of mammalian cells and preparation of cell-encapsulated 3D ECM

We isolated primary mouse embryonic fibroblasts (MEF) from CF-1 strain mice at 13 days gestation (Charles River Laboratories) using the established protocol from WiCell Research Institute. We cultured the MEFs in Dulbecco's Modified Eagle's Medium (DMEM) with 10% bovine calf serum, supplemented with 1% non-essential amino acids (all reagents from Invitrogen) in 5% CO_2 and 37°C. Before injecting MEFs into the chip, we used a Cs-137 irradiator at 8000 rads to irradiate the MEFs to prevent them from dividing as a feeder layer.

For stem cells, we obtained mouse (strain R1) embryonic stem (ES) cells that express GFP under an Oct4 promoter from the Vunjak-Novakovic lab (original source from the Zandstra lab). We first cultured them in 5% CO_2, 37°C, in complete ES cell growth media: knockout

Dulbecco's minimal essential medium (KO-DMEM; Gibco) supplemented with 0.01% of LIF (Chemicon), 15% ES qualified fetal bovine serum (Gibco), 0.1 mM 2-mercaptoethanol (Sigma), 2 mM L-glutamine (Invitrogen), 0.1 mM non-essential amino acids, and 1mM sodium pyruvate. Next, we cultured the mouse ES cells in flasks coated with 0.1% gelatin (Sigma), and passaged them every 2-3 days (depending on the morphology and size of colonies), with a change of complete ES cell growth media every day and 3 hours before passages. Differentiation media was prepared by supplementing 1mM retinoic acid (RA) (Sigma) the complete ES cell growth media in the absence of LIF.

To prepare cell-encapsulated ECM, we thawed Matrigel (BD Biosciences) overnight at 4°C in a refrigerator. We trypsinized the MEFs, centrifuged them, and resuspended them at 10^8 cells/mL in ice-cold Matrigel. Similarly, we trypsinized colonies of mouse ES cells, centrifuged them, and resuspended the cells as small clumps at 10^8 cells/mL in ice-cold Matrigel.

1.2.3. Operation of microfluidic chip: loading of cells and ECM and perfusion of reagents

To load cell-encapsulated ECM into the microchambers, we first sterilized the PDMS chip by dipping the chip in ethanol followed by air-drying, and moved the chip and cell-Matrigel mixtures to a cold room. For a PDMS chip with an $m \times n$ array of microchambers, there are (m+1) flow channels and (2n) control channels (for a 4 × 4 array of microchambers, 5 inlets/outlets for flow channels and 8 inlets for control channels).[121] Initially, we closed all control valves. To seed the cell-Matrigel mixture into a microchamber at a specific position (i^{th} row, j^{th} column), we release the air pressure at the $(2j-[i]_{mod2})^{th}$ inlet of the control layer, and a moderate amount of 4°C cell-Matrigel mixture is pipetted through the ith inlet of the flow layer [for example, to seed the mixture at the (2,2) position, we release the 4th inlet of the control layer,

and inject the cell-Matigel mixture through the 2nd inlet of the flow layer; see Supplementary Information for the definition of flow and control layer inlets' numbering]. We flowed the liquid mixtures (and all other fluids into the microfluidic chip) by positive pressure via a syringe or syringe pump (Genie Plus infusion/withdrawl pump, Kent Scientific). After observing by microscopy that cells have been loaded inside the chamber, we reapplied pressure to the inlet of the control layer. We repeated this procedure to place all types of cell-Matrigel mixtures into designated microchambers. After the seeding process was done, we moved the chip to room temperature while keeping the valves closed for 30 minutes, to allow the cell-Matrigel mixtures to gel. We then opened all the valves, and mESC medium was perfused into the whole PDMS chip at a flow rate of 0.1 µL/min.

We placed the microfluidic chip on a microscope stage and inside a stage-top environmental chamber (at 37°C, 5% CO_2, and constant humidity) with constant perfusion of fresh media. To perfuse reagents through the ECM in the microchambers (such as the experiments on determining time for complete media perfusion of a microchamber, and staining cells *in situ*), we delivered reagents (such as media, green and red dyes from Ateco Spectrum Food Colors, or PBS) by positive pressure using a syringe pump at 0.1 µL/min. We visualized dyes by taking images through the eyepiece of an Olympus SZ61 stereoscope at 45x under brightfield conditions with a Canon PowerShot S2 IS. To photopolymerize 3D microstructures in our chip, we used a Leica CTR 6000 inverted fluorescent microscope (Leica Microsystems, IL) equipped with an automated motorized-stage and InVitro acquisition software (MediaCybernetics, MD). The pre-polymer consisted of 40% w/v of PEG-diacrylate (Sigma), 2% w/v of Irgacure 2959 (Ciba Specialty Chemicals, Tarrytown, NY) as photoinitiator, and 20mM CellTracker

Blue(CMAC, Invitrogen). Exposures were carried out with a mercury arc lamp operating at 365 nm for 10 seconds.

Modeling of perfusion

We modeled flow through the 3D ECM in the chamber as flow through a porous media. Previously, early work in modeling fluid flow through porous media by Darcy [127] was adapted to evaluate bulk physiological interstitial flow through the ECM of a tissue [128-130]. Due to the complex geometry of our designs, rather than using continuum approximations (such as the Darcy or Brinkman models) to evaluate the bulk physiological flow, we used a CFD approach in which porous media is modeled by the addition of a momentum source term to the standard Navier-Stokes fluid flow equation [131]. The source term S is composed of two parts: a viscous loss term and an inertial loss term.

$$\mathbf{S} = -(\frac{\mu}{K}\mathbf{v} + \frac{1}{2}C_2\rho|\mathbf{v}|\mathbf{v})$$

where μ is dynamic viscosity, K is the permeability, C_2 is the inertial resistance factor, ρ is density and $\mathbf{v}$ is the velocity vector.

We used commercial computational fluid dynamics (CFD) software (FLUENT, Lebanon, NH) to simulate the difference in perfusion rates. We constructed a geometrical model of the chamber using the software Gambit (v2.2; Fluent Inc, Lebanon, NH), based on tetrahedral/hybrid element types for meshing of the chamber with a mesh size of 0.5 µm. The conduit was simulated as a channel with a rectangular profile. We treated all surfaces except the inlets and outlets as walls, and applied a constant pressure of 18.7 kPa to the chamber inlet plane while setting the three outlets to 0 Pa.

1.2.4. Fluorescence microcopy

To assess cell viability, we perfused the ECM in the microchambers with the Live/Dead assay kit (Invitrogen), followed by incubation at 37°C for 30 minutes. We acquired fluorescent images using a Leica DMI6000B inverted microscope equipped with a Qimaging Retiga 2000R camera and commercial image acquisition software (InVitro).

For the 3D reconstruction images, we prepared 4 mg/ml type I collagen and 8.3 mg/ml samples and let them gel in a 37°C incubator for 1 hour before imaging. We imaged the samples using an Olympus Fluoview 300 IX70 inverted confocal microscope with a HeNe laser at 488 nm excitation/532nm emission and 40x magnification. In Fluoview, the chambers were imaged by taking *z*-stacks every 1 µm throughout the whole gel. The raw images were then reconstructed and processed in ImagePro using a 0.46 µm voxel size.

1.3. Results

1.3.1. Design and fabrication of microfluidic system

Integrating 3D ECM into microfluidic chips poses special design considerations, such as effective perfusion of medium and reagents without displacing the gel from the chamber. We used the pneumatically actuated valves developed by Quake and others, and designed small posts and valve features specifically for working with 3D matrices (Fig. A1-1). The 3D ECM in each chamber in the array can be individually loaded and perfused in real time, and the behavior of cells inside the 3D chambers can be monitored by phase-contrast or fluorescence microscopy.

Our microfluidic chip contains two PDMS layers (attached to a glass substrate). The fluid layer, where cells and ECM are placed, contains 16 individually addressable microchambers (200-µm diameter and 18-µm tall) organized in a 4×4 geometry and spaced 330 µm apart from each other. Five inlets and five outlets are used to load and purge the chambers. A water-filled

control layer on top is pressurized by a compressed nitrogen source (to deflect the PDMS membrane downwards to seal off the fluid channel underneath); each channel in the control layer is independently controlled by an external solenoid valve that can be adjusted manually or by voltage (Fig. A1-1A andB). Four valves surround each chamber in the fluid layer; controlling the opening and closing of channels in the fluid layer (to allow exchange of diffusive factors between adjacent chambers) can potentially produce 16 different 3D microenvironments since each chamber has access to a different set of neighboring chambers.

Compared to previous work,[121] our procedure for fabricating and operating the chip features two notable differences. First, to build the two-layer device, we treated the two PDMS layers with oxygen plasma before alignment and bonding to allow actuation of the valves at high pressure. Compared to devices using the bonding of PDMS layers made from 1:5 and 1:20 ratios (these devices typically withstand pressures up to 20 psi), plasma treatment provides tight bonding of the two layers while leaving the device intact for pressures up to 70 psi; this higher pressure was needed to close taller fluidic channels than previous studies (18 µm vs. 9 µm [121]) in order to achieve a sufficiently thick ECM (at least 15 µm to be considered 3D[132]). Our results demonstrated that the two-layer device can be aligned and produced to high spatial fidelity using the plasma-bonding method (Fig. A1-1C and D). Second, to facilitate working with 3D ECM that gels at room temperature, we loaded the chambers with liquid ECM in the cold room (by actuating the valves manually using syringes or via gas tanks) before moving the devices to room temperature in order to gel the Matrigel.

To facilitate the perfusion of media or biochemical reagents through the 3D ECM inside the microchambers, we incorporated two sets of new design elements. First, in the control layer, we designed ring-shape microvalves that are positioned on top of each individual chamber of the

fluid layer (Fig. A1-1C). Thus, after loading of the liquid ECM into individual chambers, actuation of the ring-shaped valve (followed by gelling of the ECM, and opening of the ring-shaped valve) will result in the formation of small conduits above the gelled ECM to allow for facile medium perfusion; we ensured these valves do not deflect completely to the bottom of the fluid channel by decreasing their width to 40 µm. Second, we designed small posts around each chamber to act as a fence to maintain the integrity of the gel during perfusion.

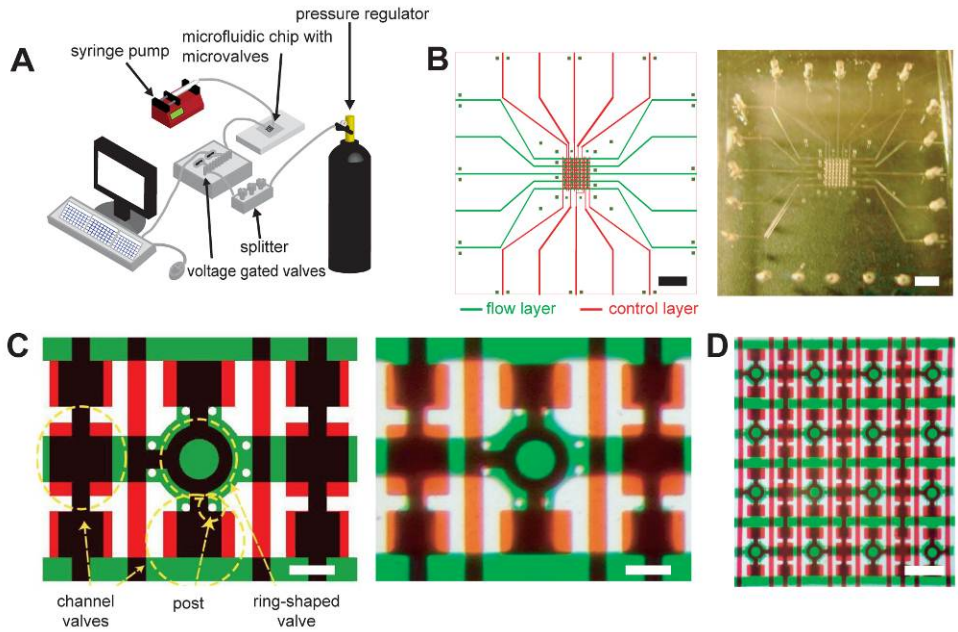

Figure A1-1: Design and structure of the microfluidic setup. (A) A schematic diagram of the experimental setup. A two-layered PDMS chip is connected to a regulated gas tank via voltage-gated valves. For media perfusion through all microchambers, a syringe pump is connected to the chip. For injection of reagents or cell-matrix mixtures into specific microchambers, the path of the fluid flow is controlled through the switching of the voltage-gated valves. **(B)** Design of the microfluidic chip as shown by an overlay of both the control and flow layers (left), and picture of the corresponding chip after assembly (right). Scale bars = 2 mm. **(C)** Design of a single chamber (left), and brightfield image of the device loaded with two different food coloring dyes (green in fluidic flow layer and red in control layer) (right). The microvalves are located at enlarged crossings of a control channel with a flow channel when viewed from the top. Scale bar = 100µm. **(D)** Brightfield image of the 16 microchambers loaded with green dye in the flow layer and red dye in the control layer. Scale bar = 300 µm.

1.3.2. Loading of 3D ECM and cells into microchambers

For the 3D ECM in this study, we used Matrigel, a reconstituted basement membrane matrix (composed mainly of laminin and collagen IV[133]). Matrigel is a naturally derived ECM used

in previous studies to mimic natural 3D environments for mammalian cells, and has been used to encapsulate mouse ES cells.[124, 134] As an example of a real-time sequence of controlling microvalves, we briefly describe the loading and purging of a cell-Matrigel mixture into desired chambers. We loaded the desired chambers with cell-Matrigel mixtures by first flowing the solution into the chip without closing any valves. We could load all 16 chambers within 20 seconds of injection. Next, we closed the valves surrounding the loaded chambers, and purged the remaining chambers with PBS. For two neighboring chambers denoted (by row and column) (2,2) and (2,3), we released the 2*3-[2]mod2=6th inlet of the control layer to flush the (2,3) chamber with PBS through the 2nd flow layer inlet (Fig. A1-2A). Since each chamber contains a volume of 0.2 nL, we used a cell density of 108 cell/mL to achieve on average 20 cells/chamber (in practice, we observed clumping of cells). Thus, by opening and closing different microvalves in an appropriate sequence, we loaded 3D cell-laden ECM into individual selected chambers, and could selectively purge cells and ECM out of other chambers (Fig. A1-2B).

Although Matrigel has a viscosity of 10-15 cP [135] (about 10 to 15 times the viscosity of water), we easily loaded it into the chambers as long as the temperature was maintained around 4°C during the loading process. By loading of the Matrigel into a chamber, actuation of the ring-shaped valve, gelling of the Matrigel, and release of the valve, we aimed to produce a small conduit above the gelled structure. We verified the 3D nature of the ECM inside the microchambers and visualized the conduits using confocal microscopy followed by 3D reconstruction (Fig. A1-2C). We also loaded collagen I, another commonly used 3D naturally derived ECM, [125] into the microchamber with a conduit for media perfusion using this technique (Fig. A1-2D).

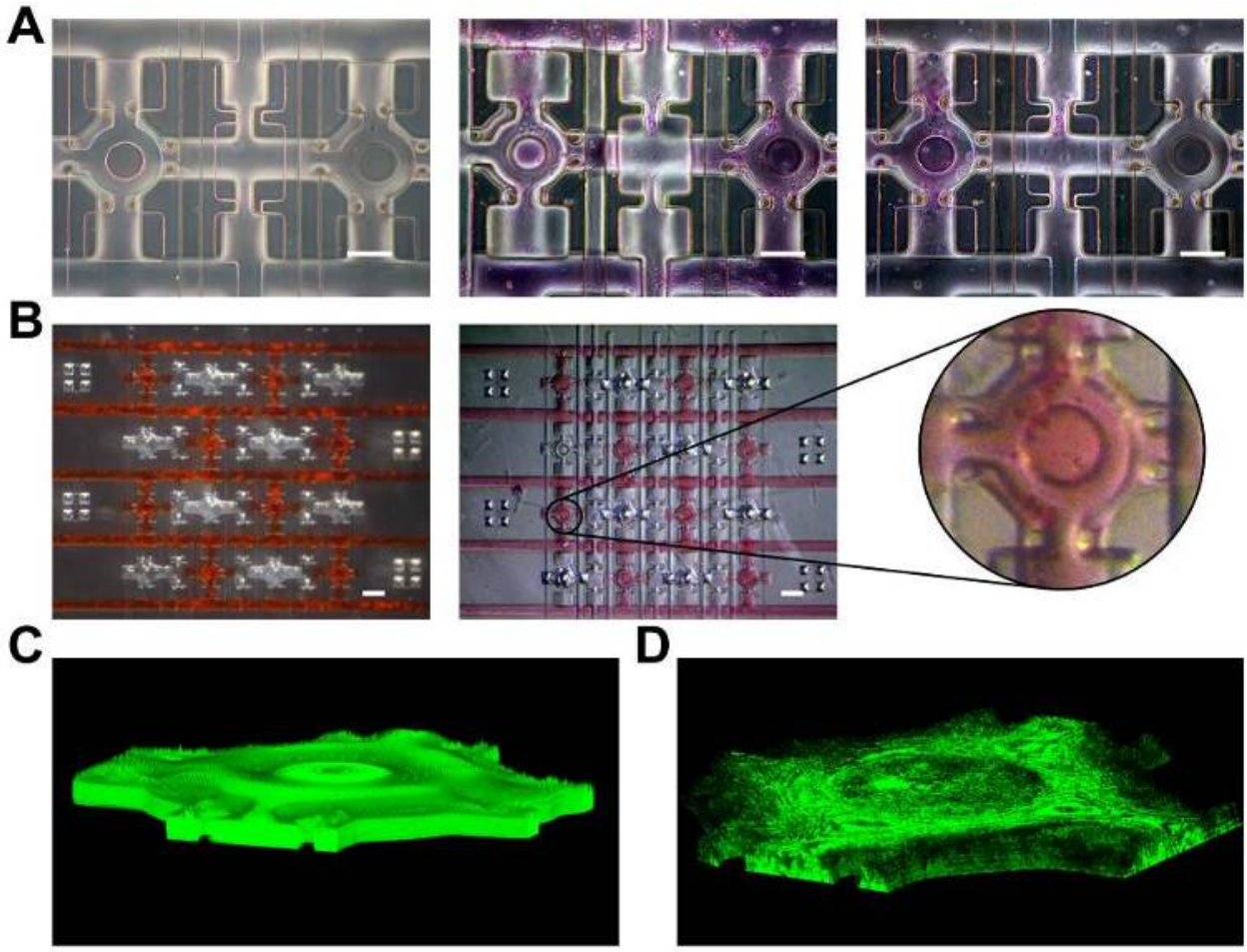

Figure A1-2: Demonstration of actuation of valves. (A) Phase-contrast images showing the loading of a single chamber with Matrigel encapsulating MEFs. The cell-Matrigel mixture is loaded into the two empty chambers (left), valves surrounding the left chamber are closed (center), and the right chamber is purged (right). The Matrigel is gelled after the right chamber is purged. Scale bar = 100 µm. **(B)** Demonstration of ability to individually address chambers, by loading red dye (left) and cell-Matrigel mixture (right) into a checkerboard pattern. The pattern is created by first closing four sets of valves to prevent the mixtures from entering the chamber (while leaving the rest of the valves open). Then the solution is injected into the top left inlet. Scale bar = 200 µm. **(C)** 3D reconstruction of a confocal image (taken at 40x magnification) of a chamber loaded with 3D Matrigel, with visible conduits above the 3D gel created by partial deflection of a ring-shaped valve positioned above the chamber. **(D)** 3D reconstruction of a confocal image of a chamber loaded with a 3D collagen I matrix, with visible conduits.

1.3.3. Perfusion through 3D ECM

Using this setup, we aimed to demonstrate that gels could readily be perfused *in situ* with media and reagents reliably and quickly (Fig. A1-3A). In an initial experiment, we loaded a chamber with a mixture of liquid Matrigel and red food coloring dye, partially depressed the chamber valve to create a conduit, and gelled the mixture. Using time-lapse microscopy, we

observed that with a flow rate of 1 µL/min of buffer, we could purge the dye out of a single chamber filled with 3D Matrigel in about 2 seconds (Fig. A1-3A).

We explored our ability to analyze cells *in situ* inside 3D matrices by perfusing the gels with analytical reagents. In this experiment, we cultured and stained MEFs in Matrigel by performing a viability assay. We continuously perfused the MEFs inside the Matrigel with a Live/Dead solution for 30 minutes. We observed cell viability of around 90%, which is comparable to the viability observed for mammalian cells in other experiments using 3D ECM [115, 116] (Fig. A1-3B).

Rather than a fixed perfusion rate, we also investigated the integrity of the gel structures (stabilized in their positions by the microposts) at high flow rates (up to 100 µL/min). As we increased the flow rate by 10 µL/min increments, the pressure buildup due to resistance from the small dimensions of the channel appeared to expand the PDMS microchannels. Nonetheless, even at the highest flow rate attempted (100 µL/min), the gel and cells remained in the chamber (Fig. A1-3C).

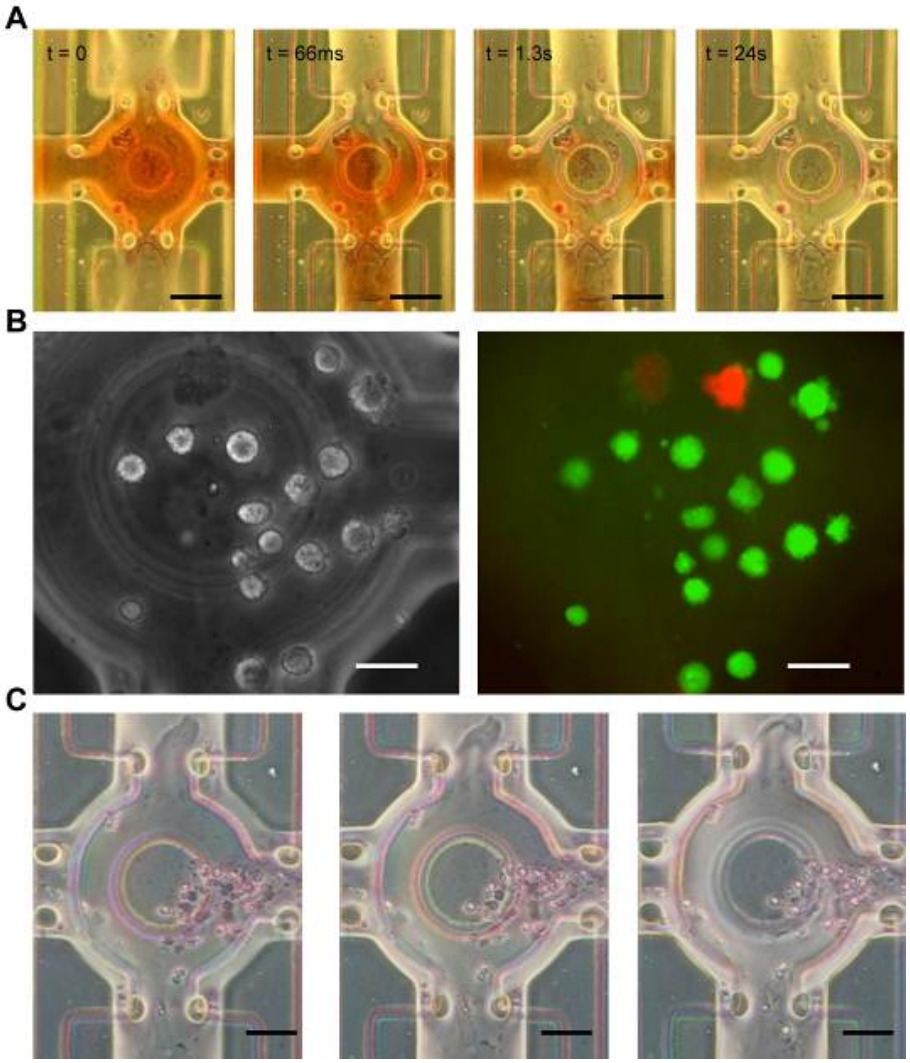

Figure A1-3: Characterization of ring-shape microvalves and microposts. (A) Time-lapse brightfield images showing perfusion of water through a single chamber loaded with a 3D Matrigel and red food coloring dye (some debris remained lodged in the gel). When water flows into the chamber, the red dye is washed away in the conduit (as shown at t=66ms). The remaining dye in other regions slowly washes away and is completely cleared after 24 seconds. Scale bar = 100 µm. **(B)** Phase contrast (left) and fluorescent (right) images of MEFs that are stained in situ using the Live/Dead assay. After the MEF-Matrigel mixture is gelled within the chamber, it is perfused with the Live/Dead reagents for 30 minutes. The cell viability rate is about 90%. Scale bar = 25µm. **(C)** Phase-contrast images of a single chamber under different flow rates of 1 µL/min (left), 10 µL/min (center), and 100 µL/min (right). With the microposts anchoring the 3D gel, the Matrigel remains firmly in the chamber at high flow rates. Scale bar = 50 µm.

In order to verify our claim that the conduits facilitate the perfusion of media through the gel, we used a computational fluid dynamics (CFD) modeling approach to analyze fluid behavior

in the chamber. We modeled flow through the 3D ECM in the chamber as flow through a porous media. (see Supplementary Information for further details of the modeling).

Figure A1-4A shows the local velocity distributions for three different cross-sectional planes, with and without conduits above the 3D ECM inside the chamber. The cross-sectional plane at mid-plane cuts through the 3D ECM, and hence represents the rate of perfusion through one portion of the 3D matrix. For this plane (and all other planes), the velocity is higher for the chamber with the conduit than without the conduit. Overall, the flow rate is higher for the chamber with a conduit (5.2 µL/min) than without a conduit (1.1 µL/min). The approximate five-fold increase in flow rate can be achieved for a range of applied pressures (Fig. A1-4B). To achieve even higher flow rates in the chamber, one can increase either the inlet pressure or the height of the conduit (Fig. A1-4C).

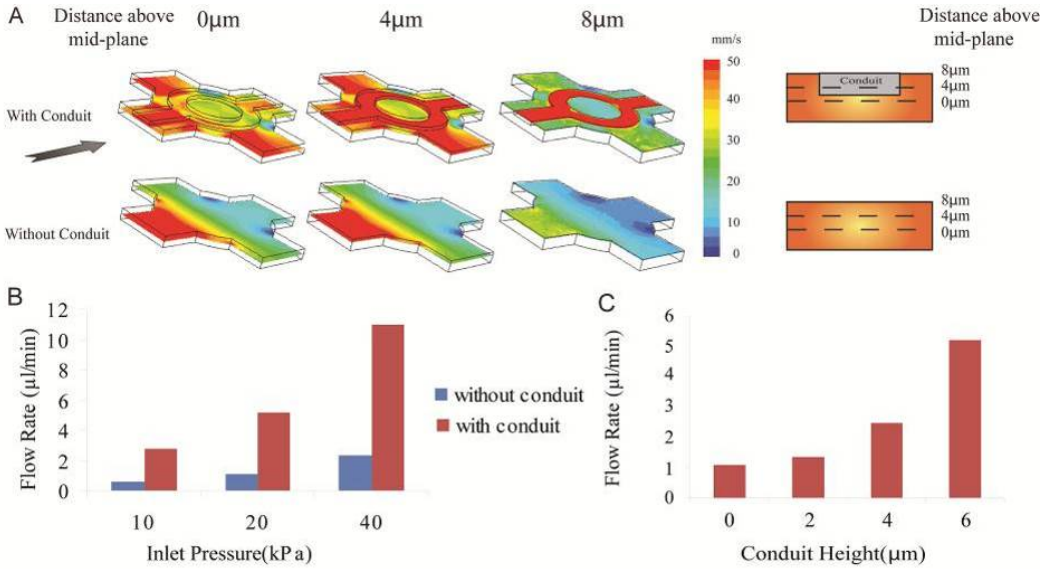

Figure A1-4: Fluid modeling of perfusion efficiency. (A) Flow velocities across the microchambers with and without a 6 µm-tall conduit. Vertical cross sections of the channel indicate the position of the three horizontal cross-sectional planes relative to the 3D Matrigel and open conduit, in chambers with and without the conduit. The images on the right show the local velocity distribution for the cross-sectional planes at 8, 4 and 0 µm above the mid-plane with a pressure drop of 20 kPa between the inlet and outlets. Chambers with conduits exhibit flow rates of about five-fold higher and more uniform velocity distribution than chambers without conduits. **(B)** Comparison of the flow rate within chambers with and without conduits, under pressure drops of 10, 20, and 40 kPa. **(C)** Comparison of flow rates within chambers with different conduit heights under constant pressure drop of 20 kPa. Under the same pressure, an increase in conduit height from 0 to 6 microns is modelled to increase the flow rate about five-fold.

The model also showed that the conduit helped produce a uniform velocity distribution in the 3D gel. Finally, since we observed that pressures in the control layer of greater than 70 psi tended to disrupt the bonding of the microfluidic chips, it may be advantageous to alter conduit heights to achieve the desired interstitial flow rate [136] rather than applying high pressure [128].

1.3.4. Culture and staining of mouse embryonic stem cells inside 3D ECM

As a demonstration of a biological application, we explored the ability of our microfluidic chip to culture embryonic stem (ES) cells. The ability of ES cells to maintain an undifferentiated state is highly sensitive to their 3D microenvironments (such as growth factors, presence of neighboring cells, and the size of the embryonic stem-cell cluster): for example, mouse ES cells differentiate in plain media without supplementation with leukemia inhibitory factor (LIF).[137] Also, whereas most studies on ES cells have been performed on flat 2D surfaces, studies of mouse ES cells in well-controlled 3D ECM are only emerging.[117, 138, 139] In the future, the ability to analyze the differentiation of ES cells under well-controlled 3D ECM may improve understanding of the basic mechanism for maintaining the self-renewal capacity of ES cells, as well as aiding large-scale in vitro propagation of ES cells for regenerative medicine.

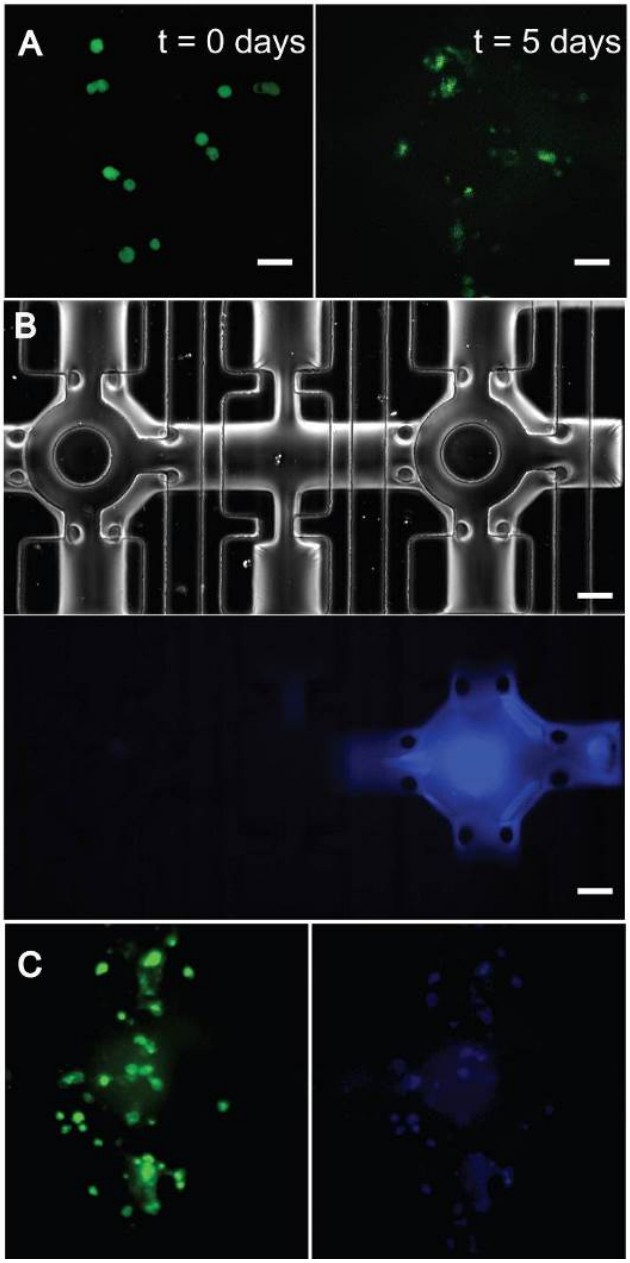

Figure A1-5: Flow study of mouse ES cells in chambers of 3D Matrigel inside microfluidic chip. (A) Fluorescence images of mouse ES cells encapsulated within 3D Matrigel immediately after gelling of the Matrigel, and after five days of culture. (Different regions were taken in the two images.) The mouse ES cells express GFP under an Oct4 promoter, and therefore fluoresce green only if they are undifferentiated. Scale bars = 50µm. **(B)** Phase-contrast image of two neighboring chambers before loading of reagents (top), and fluorescence image (blue channel) of the two neighboring chambers after loading and gelling of PEG-diacrylate with CellTracker Blue in the right chamber, and mouse ES cells in Matrigel in the left chamber (bottom image). (Note that the blue fluorescence in the right chamber is due to the polymerized PEG-diacrylate, not CellTracker Blue, which fluoresces blue only when it is inside cells.) All valves are closed. Scale bar = 50µm. (**C)** Fluorescence images of stem cells in the left chamber taken under green (left) and blue (right) channels (of the same region), indicating the cells express GFP and have uptaken CellTracker blue, respectively. Scale bar = 50µm.

We first analyzed the differentiation state of mouse ES cells cultured over days in 3D Matrigel microchambers inside our micofluidic chip. A challenge in maintaining the viability of mammalian cells in microfluidic chips, especially in systems with 3D matrices, is effective perfusion. Mouse ES cells are sensitive to ineffective perfusion because they differentiate in the absence of LIF (which must otherwise be supplemented in the media); in this experiment, the mouse ES cells express GFP under the control of the Oct4 promoter, and turn off GFP expression when they lose their pluripotency. To maintain a viable long-term culture of undifferentiated mouse ES cells, we perfused the cell-Matrigel chambers with fresh media (supplemented with LIF) every 12 hours, and monitored the fluorescence of the cells. Our results show that the mouse ES cells, encapsulated within 3D Matrigel, remained undifferentiated and viable for at least five days inside the microfluidic chip, as they remained brightly fluorescent (Fig. A1-5A). The demonstrated ability to maintain ES cells in an undifferentiated state – coupled with our ability to vary growth factors, presence of neighboring cells, and the size of the hydrogel for an individually addressable array of 3D microchambers – may allow high-resolution interrogation of the factors behind stem-cell growth and differentiation, in a manner that bulk gel experiments cannot easily achieve.

Finally, we performed an *in situ* staining assay of the mouse ES cells by exposing the chamber to the analytical reagents in a neighboring chamber; this experiment established the feasibility of diffusible factors moving from one chamber to a neighboring chamber that contains cell-laden ECM, upon opening of the valves. In a configuration of two neighboring chambers (Fig. A1-5B), we first loaded the right chamber with a cell-staining dye (CellTracker Blue) in a photopolymerized 3D gel (PEG-diacrylate), and closed the surrounding valves. We then introduced a mixture of mouse ES cells and Matrigel into the left chamber, and gelled the

mixture. Before opening of the valve that connects the two chambers, we confirmed that the mouse ES cells in the left chamber did not fluorescence blue (Fig. A1-5B). Upon opening the valve between the two chambers to allow the CellTracker dye to diffuse from the right chamber to the left chamber, the mouse ES cells in the left chamber fluoresced blue after half an hour (Fig. A1-5C) and also fluoresced green (confirming an undifferentiated state) (Fig. A1-5C), as expected.

1.4. Discussion

This study builds on previous work for studying cells in controlled microenvironments. For studying mammalian cells on 2D surfaces, perfusion systems have been developed to improve the culture of hepatocytes on PDMS membranes.[140] In another study, tissue aggregates could be induced to form in compartments on microstructured scaffolds.[141] These studies allowed superfusion or perfusion of media to the cells, but offered limited spatiotemporal control of the perfusion. Real-time control of mammalian cells on 2D environments has recently been demonstrated.[142] For 3D cultures, a microchannel-based system has been developed to perfuse a number of.mammalian cell types in 3D.[115] This approach facilitated observation of cells under constant perfusion in 3D, but capabilities for controlled high-throughput experiments of an array of cells may be limited using a simple microchannel-based configuration with no microvalves. Finally, an array of twelve micro-bioreactors has been developed for spatiotemporal investigation of factors that regulate differentiation of mammalian cells in 3D.[118] The chambers, however, were not individually addressable.

Compared to previous work, the microfluidic design in this study provides real-time and individually addressable control over 3D microenvironments in an array of chambers (and the connections between neighboring chambers), in a manner suitable for long-term cell culture,

observation, and analysis. In the future, by loading each chamber with a different type of ECM and cells, and by perfusing different reagents into the chambers at different times, it may be possible to observe the behavior of cells in a large number of different 3D microenvironments in parallel. Possible applications include the ability to study cells under different perfusion rates, different spatiotemporal sequences of cell-cell signaling, and perfusion of different growth factors.

1.5. Conclusion

We have developed a novel microfluidic system for controlling and studying an array of mammalian cells in 3D microenvironments. This approach integrates the powerful technology of pneumatically actuated microvalves with studies of mammalian cells in 3D microenvironments. The microvalves enable selective delivery of reagents to individual 3D chambers, as well as spatial control of diffusion pathways between neighboring chambers. Conduits above the 3D matrices allowed rapid and controlled perfusion through the matrices (such that the 3D matrix does not block fluid flow), and microposts positioned around the chambers stabilized cell-laden 3D gel under high flow rates (such that the 3D matrix is not displaced). Further, permanently bonded (plasma-treated) PDMS chips allowed leak-free operation of the chip under pressures of up to 70 psi, thereby permitting the closing of microvalves over channels of sufficiently large heights for culturing cells in 3D matrices. Altogether, our system could manipulate cell-matrix suspensions, control chamber-to-chamber communication, and enable rapid perfusion of reagents through an array of 3D extracellular matrices with high spatial and temporal precision. In the future, this technology may be appropriate for high-throughput screening, single-cell studies, or studies of paracrine signaling in 3D cell cultures where rapid changes of 3D microenvironments or long-term culture is desired.

Appendix 2. To develop a platform to accurately identify *in vivo* drug efficacy across heterogeneous genotypes

2.1. Introduction

Large number of anticancer drugs indicates that the search for a single broad-spectrum anticancer drug may have to yield to a personalized medicine approach, where different anticancer drugs are prescribed for patients with different genotypes of cancers. For example, whether a specific patient will respond to an anticancer drug depends on the genotypes of his or her tumor cells (as well as the specific genotypes of surrounding stromal cells, including, endothelial cells, fibroblasts, macrophages, myeloid-derived suppressor cells, TIE2-expressing monocytes, and mesenchymal stem cells). However, the challenge is that using current techniques, where the *in vivo* testing of one genotype requires one host animal, it is extremely difficult to predict the *in vivo* efficacy of lead compounds across a large number of genotypes. As a result, only a very small number of genotypes of patient subpopulation is tested in the expensive Phases II and III, and otherwise promising lead compounds that pass Phase I can easily fail in Phase II and III trials. The end product is a non-ideal process where lead compounds with high safety and favorable ADME-Tox are discarded completely due to lack of "efficacy", even though such compounds may in fact be effective for other cancer genotypes.

Currently, the ability to screen the effectiveness of anticancer compounds in a high-throughput manner resides in conventional HTS methods (originally developed 15 years ago) that focus on *in vitro* readouts. These readouts are useful, but bear an unclear correlation to results *in vivo*. We plan to leverage state-of-the-art bioengineering techniques to develop a platform where compounds can be tested for efficacy against a large number of genotypes in an *in vivo* setting. We hope that this platform will help unlock the full potential of each drug

candidate, as its efficacy will be assessed in an *in vivo* setting for not just the specific genotypes designated in a Phase II or III trial, but instead, across a very large number and range of genotypes.

So far, the monolayer culture system is the most widely used *in vitro* method to investigate the efficacy of anticancer therapeutic agents. However, the inability of the monolayer system to accurately mimic tumor microenvironments leads to inaccurate prediction of drug efficacy *in vivo*; for example, during the past two decades, only 8% of the drug candidates that enter Phase I trials reach the bedside. To better mimic tumor microenvironments, numerous *in vitro* 3D culture systems have been proposed within the last two decades; for instance, multicellular tumor cell spheroids (MTCS) are believed to accurately emulate tumor cells *in vivo* both in terms of their pathophysiology and response to therapy. These aggregates can mimic tumor tissue more effectively than regular 2D cell cultures because spheroids, much like tumors, usually contain both surface-exposed and deeply buried cells, proliferating and non-proliferating cells, and well-oxygenated and hypoxic cells (the latter secreting tumor cell cytokines). Nevertheless, it remains extremely difficult, if not impossible, to recreate tumor microenvironment *in vitro*.

The other conventional preclinical approach for assessing the efficacy of anticancer compounds is through animal models, such as transgenic mice and xenografts. However, the low throughput of these systems and the inability to test large number of cell-lines limits their potential to capture the genomic heterogeneity of real cancer patients. Consequently, it is extremely challenging to identify the subgroups of responsive cancer cells for the lead compound.

There is a large body of evidence that suggests that many drug candidates are highly effective towards subpopulations of cancers. For trastuzumab, HER2 receptor expression level

was chosen as the biomarker for patient stratification, with the result that the drug was highly efficacious for a subpopulation of breast cancer patients. The subpopulations themselves are large markets: in 2009, around 8% of the entire anticancer drug market in the US was attributed to trastuzumab.

We are proposing to focus on the Hh pathway. There is mounting evidence that this pathway is firmly linked to the etiology of basal cancer carcinoma and a subset of medulloblastoma, with efficacy demonstrated in animal models and compounds currently in Phase II clinical trials (GDC-0449, LDE225, BMS-833923, IPI-926, PF-04449913, LEQ506 and TAK-441). Also, there is increasing evidence that other sporadic cancers such as pancreas, prostate, lung, and breast could benefit from Hh inhibitors. For example, Hh inhibitors has been shown to be effective in many tumors which are lacking Hh pathway mutations; in these cases, the drugs act on the stroma rather than the tumor cells themselves. Hence, the efficacy of cancer drugs also depends on the different genotypes of stromal cells around the tumors, which can differ from patient to patient. Here, by capitalizing on recent technologies in microprocessing implantable biomaterials, we aim to develop a high-throughput screening platform to test the efficacy of a cancer drug across heterogeneous genotypes of tumors in a realistic in vivo setting(Fig. A2-1).

2.2. Methods

2.2.1. Construct design and fabrication

We used standard soft lithography techniques to fabricate a microfluidic construct composed of three layers; a loading layer; a chamber layer, and a membrane layer (Fig. A2-2B). Loading layer is a thick polydimethylsiloxane(PDMS) layer with 100-µm tall channels connecting the inlets to the top of the microchambers in the chamber layer. Chamber layer on the other hand is a

thin (300 µm) PDMS layer which has an array of 500-µm circular through-holes. The third layer, membrane layer, is a very thin PDMS layer (60 µm) which covers the bottom side of the chambers, an array of 4-µm micropores at the bottom of each chamber, allows nutrient/oxygen exchange with the microchambers [8].

Patterns of the three layers were designed in Autocad (Autodesk Inc., USA) and were directly written on AZ1500-resist-coated 4 inch chrome masks using µPG 101 Laser Writer (Heidelberg Instruments Mikrotechnik GmbH, Germany). To make the masters, we spun-coated a 100-µm, a 300-µm, and a 60-µm layer of epoxy-based photoresist SU-8 3050 (MicroChem, Newton MA) onto three 4-inch Si wafers (Silicon Sense, Nashua NH), exposed them to 365-nm UV light through three different chrome masks using an OmniCure® S2000 UV exposure system (Lumen Dynamics Group Inc, Canada) for channel, chamber, and membrane layers respectively, and developed the features with propylene glycol monomethyl ether acetate (Sigma-Aldrich, St. Louis MO). Masters were then exposed to a vapor of Trichloro(1H, 1H, 2H, 2H - Perfluorooctyl) Silane (Sigma, 448931) for 1 hour (to aid PDMS removal).

We used partial curing technique to bond the three layers of PDMS together. We replica molded the masters with PDMS (Dow Corning Sylgard 184) made from a 15:1 ratio of base to curing agent. In order to achieve partial curing the ~0.5-cm thick PDMS piece for the channel layer was cured at 70°C for 40 min. We peeled off the channel layer from its master, tape-cleaned it and punched holes through the PDMS molds using a flattened 16G1$^{1}/_{2}$ needle (Becton Dickinson, Franklin Lakes NJ) to create the inlets. To make the 300-µm thick chamber layer, chamber layer master were PDMS spun coated at 700 rpm for 30s and subsequently cured at 70°C for 30 min. Then we aligned the channel layer on top of the chamber layer using a custom-made device and bonded under pressure at 70°C for 2 hr. Then we peeled off the bonded layers.

To fabricate the 60-µm thick membrane layer, we first diluted PDMS with toluene (7:1 ratio) and spun coated the master with the diluted PDMS at 2000 rpm for 30s and subsequently cured at 70°C for 10 min. Then we aligned the previously bonded two-layer piece on the membrane layer using the custom made device and bond them together under pressure at 70°C for 2 hr. Then we peeled of the three bonded layer construct and inserted the tubing to inlets followed by sealing.

2.2.2. Cancer and stromal cells culture

HT-29 and DLD-1 colorectal adenocarcinoma epithelial cells were purchased from ATCC (HTB-38 and CCL-221) and expanded in ATCC-formulated McCoy's 5a and RPMI-1640 Medium respectively supplemented with fetal bovine serum (ATCC 30-2007) to a final concentration of 10%.

10T1/2 fibroblast cell line, as transfection host, were purchased from ATCC (CCL-226) and expanded in Eagle's Basal medium with 2 mM L-glutamine, 1.5 g/L sodium bicarbonate and Earle's BSS. To make the complete growth medium, we added heat-inactivated fetal bovine serum (Invitrogen, 10082-139) to a final concentration of 10%.

2.2.3. Hedgehog (HH) pathway reporter

In order to measure hedgehog signaling activity in the 10T1/2 cells, we transfeted them with Cignal GLI reporter (CCS-6030L, SABiosciences) using Attractene transfection reagent (301005, Qiagen). The GLI reporter is a mixture of a GLI-responsive luciferase construct and a constitutively expressing Renilla construct (40:1). The GLI-responsive luciferase construct encodes the firefly luciferase reporter gene under the control of a minimal (m)CMV promoter and tandem repeats of the GLI transcriptional response element. The number of response elements and the intervening sequence between these response elements has been experimentally

optimized to maximize the signal to noise ratio. The GLI reporter construct monitors both increases and decreases in the transcriptional activity of GLI, and hence the activity of the hedgehog signaling. The constitutively expressing Renilla construct encodes the Renilla luciferase reporter gene under the control of a CMV immediately early enhancer/promoter and acts as an internal control for normalizing transfection efficiencies and monitoring cell viability. We used dual-luciferase assay (E2920, Promega) to monitor the activity of GLI and determine the effect of various treatments. We visualized the luciferase signal using LAS-4000 gel imager (Fujifilm Life Science, USA).

2.2.4. Construct cell loading and culture

Prior to loading the construct with the cell, we UV-sterilized it for half an hour; then through the inlet tubing, we loaded 2 ml of the HT-29 and DLD-1 cell-media mixture at the concentration of 10^6 cells/mL to each chamber. We cultured the cells for one week so the spheroids are formed within the chambers while the construct is immersed in the culture media. Then, after the spheroids are formed we punch the middle part of the construct (Fig. A2-2C) flipped it over and cultured the transfected fibroblast 10T1/2 cells on the membrane side of the membrane.

2.3. Results

We aim to perform high-throughput screening of a cancer drug across heterogeneous genotypes of tumors in a realistic *in vivo* setting. Specifically, the ultimate goal is to probe the drug response of different type of tumor cell lines simultaneously while recapitulating the physiology and microenvironment of solid tumors. Using microfluidic technology we developed an implantable cassette containing 20 chambers, each capable of encapsulating a different cell type. This platform enables high-throughput studies of tumor-stroma interaction within a realistic *in vivo* setting (Fig. A2-1). Currently, the construct has 20 different chambers but could

be easily expanded and the end result is a device akin to a 96-well or 386-well plate, except that the entire device is made of biocompatible material, is only millimeters in dimensions and thickness, and can be directly implanted into an animal host.

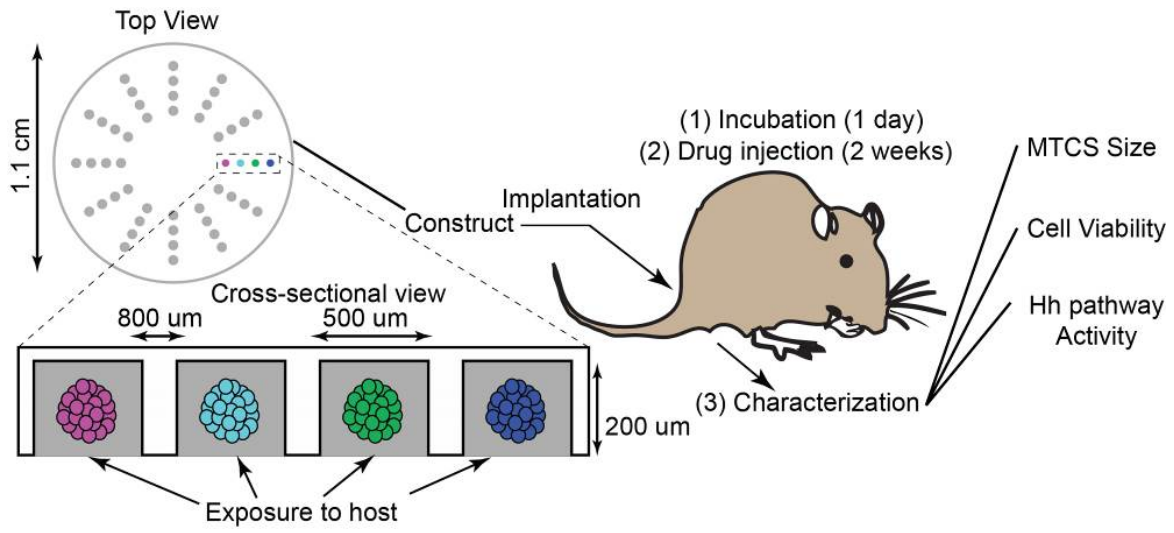

Figure A2-1: Overall experimental strategy and schematic of tumor cell laden construct. Left: Construct loaded with different tumor cells (top). Cross-section of chambers showing different tumor cells (bottom). Right: Overall experimental strategy including construct implantation and characterization.

2.3.1. Construct fabrication

We fabricated the construct using soft lithography techniques as described in the Methods. The most challenging part of the construct fabrication was the binding of different layers. Since, we have to align the microscale features of each layer, we could not use the time sensitive binding methods (which otherwise provide strong binding); hence, we used partial curing method with the ratio of 15:1 for PDMS to curing reagent. The challenge with this technique is to figure out the correct curing time and bonding pressure to preserve the micron-scale features and also create strong air-tight binding.

The other challenge was fabricating the membrane layer master. In order to trap the cells, the pores should be small (~4 µm); however, due to large thickness of the posts, the aspect ratio of these structures is very large. Large aspect ratio caused these post structures to be very fragile

with weak adhesion to the substrate and as we peeled off the construct from the master, these structures came off as well. Hence, by trying different designs we tried to maximize the adhesion strength of the posts while keeping their width minimal, such that they can trap the cells.

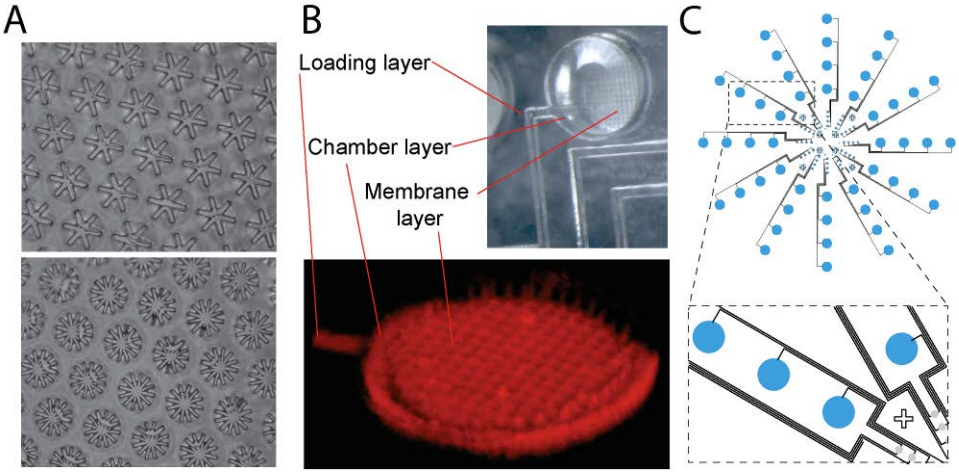

Figure A2-2: Construct fabrication. **A)** Different membrane designs **B)** Close-up of a single chamber before (top) and after (bottom) loading with fluorescent tracers. **C)** Top view of the microfluidic device encapsulating 20 different cell types (top) and its blowup image showing the microfluidic channel leading to the chambers (bottom).

2.3.2. Cell loading for *in vitro* cross-talk experiment

The ultimate goal of this project is to load 20 different cancer cell lines -- each of which having distinct genotype -- into the 500 um diameter, 300 um-tall cylindrical microchambers. But, currently to rule out the possibility of cross-talk between the tumor cells of different chamber mediated through stromal cells, we loaded all of the chambers with only two tumor cell lines, HH ligand expressing (HT-29) and non-expressing (DLD-1) cell lines, and studied the effect of HH ligand secreted from the HT-29 cells on the HH pathway activity of the stromal cells (10T1/2) cells either in the close proximity of the HT-29 cells or those associated with the neighboring chamber containing DLD-1 cells.

In brief, HH ligands secreted by tumor cells bind to Patched (PTCH1) receptor on stromal cells, causing internalization and degradation, thereby releasing Smoothened (SMO) to enter the primary cilia. This results in nuclear translocation and stimulates the transcription of HH pathway target genes and growth factor (GF) secretion by stromal cells. As all HH signaling through the canonical pathway requires SMO, small molecules such as cyclopamine, which inhibit SMO function, completely block all HH pathway signaling.

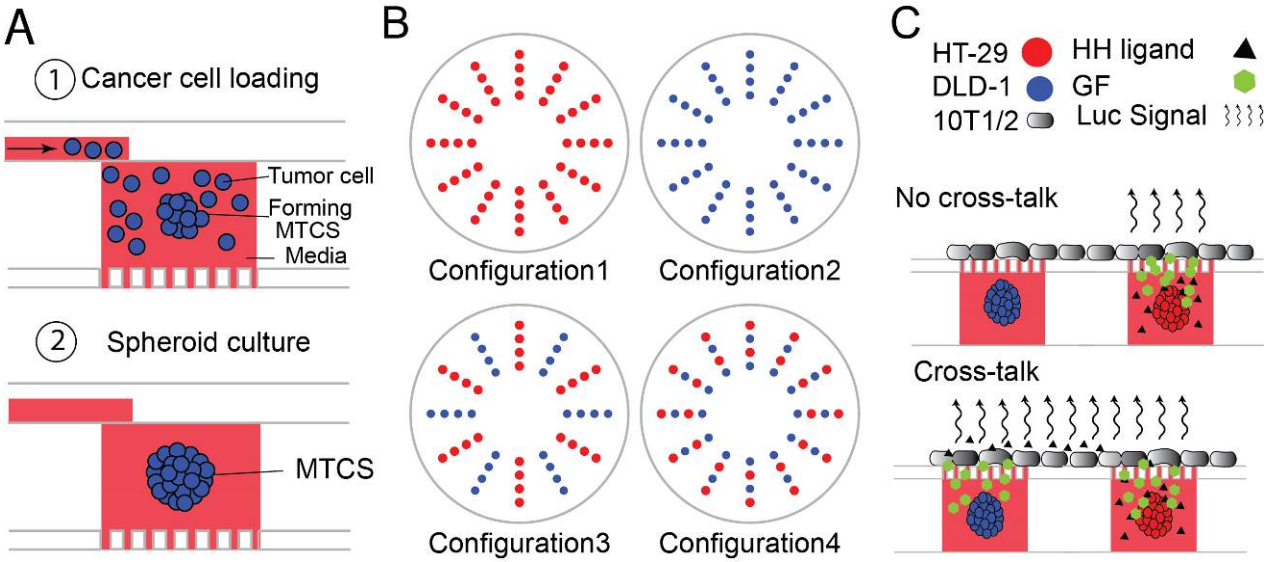

Figure A2-3: Construct loading for in vitro cross-talk assay. **A)** Loading of cancer cells (top) and culture (bottom). **B)** Different configuration of HT-29 and DLD-1 cells **C)** HH-reporter-transfected 10T1/2 monolayer culture for cross-talk assay.

2.3.3. Luciferase assay

Prior to performing the *in vitro* cross-talk experiment, we have to make sure that HH ligand secretion from HT-29 cell will elicit HH pathway activity in HH-reporter-transfected 10T1/2 cells compared to DLD-1 cell. We co-cultured 10T1/2 cells with either HT-29 cells or DLD-1 cells or added SHH protein (which is known to elicit HH pathway activity) at three different concentrations of low, medium and high for 1 day. We characterized the firefly and Renilla luciferase activity of the 10T1/2 for all of these cases and calculated the Relative Response Ratio

(RRR). The 10T1/2 cells co-cultured with HT-29 cells shows higher RRR compared to those co-cultured with DLD-1 cells.

Firefly luciferase signal **Renilla luciferase signal**

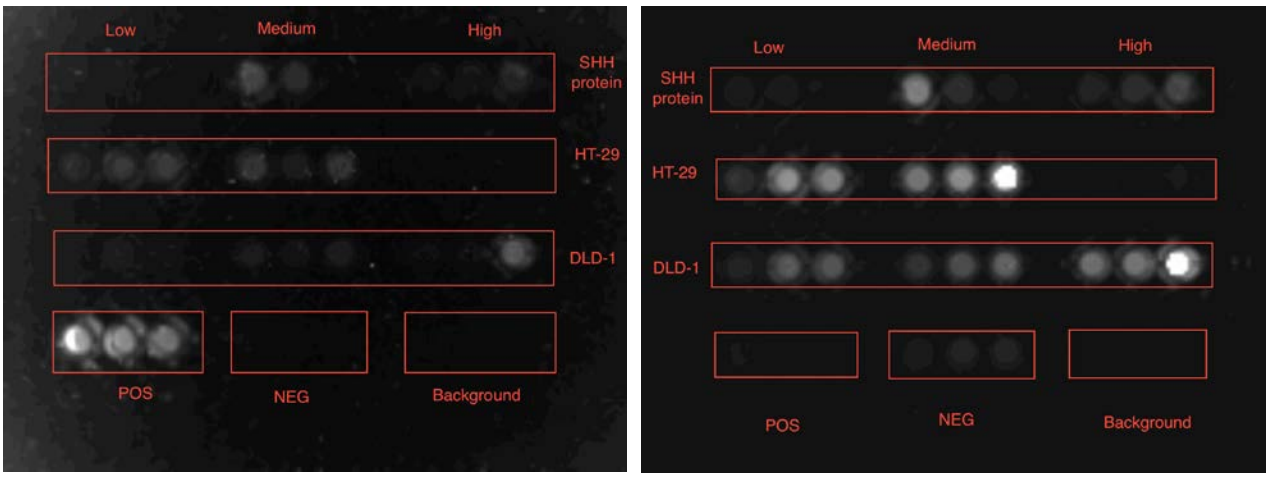

Figure A2-4: Luciferase assay. Left; Firefly and Right: Renilla luciferase signal. 10T1/2 cells co-cultured with either HT-29 cells, DLD-1 cell or SHH protein (which is known to elicit HH pathway activity) at three different concentration of low, medium and high for 1 day and imaged using the dualglow reagent.

We used dual-glow luciferase assay to characterize the effect of HH ligand on the stromal cell HH pathway activity. This reagent is lysing the cells; hence, mix the content of all cells. So, we can't use this reagent to study cross-talk as described in the previous section (Fig. 2-3C). Instead, we are planning to use a cell permeable luciferase substrate such that we can probe the luciferase signal locally with lysing the cells so we could derive the positional luciferase activity map and conclude about the cross-talk. Beetle Luciferin (E1603, Promega) is such a substrate; however, the current problem is that luciferase signal made via this substrate is extremely week which makes it impossible to do the cross-talk experiment.

2.4. Discussion

We are planning to conduct the in vitro characterization of this platform by finishing the in vitro cross-talk experiment. After studying the cross-talk assay in vitro, one have to repeat this experiment in vivo; duplicate constructs of each configuration (8 constructs in total) should be made and implanted in mouse (one construct in each). Then, Hh inhibitors should be administered to four mice (test group) each carrying a different configuration and administrated vehicle to the other four mice. After 2 weeks of drug administration (twice daily) to the test group, all construct (the test and the control groups) should be extracted and the difference between the size of the test group and the corresponding control group for HT-29 and DLD-1 cells should be measured. If the difference in tumor size for test and control groups for both HT-29 and DLD-1 tumor spheroids are similar across different configurations, one can rule out the possibility of cross-talk between the chambers. By implanting constructs with different combinations of cell types and different geometries, one can minimize any cross-talk effects between chambers. Another advantage of this approach is that all cells are screened in a single host, to minimize host-to-host variability, a significant source of variation in conventional animal host experiments.

The next step is to identify the percentage of the medulloblastoma cancer subtypes responsive to anti-Hh therapy. Medulloblastoma cancers are a suitable cancer for this technology since it is still unclear in the medulloblastoma community what percentage of subtypes, and which subtypes, will ultimately benefit from anti-Hh therapeutics. Normally, extensive preclinical studies should be performed to identify an accurate and ideally large population of the drug responsive cell lines. However, performing *in vivo* preclinical studies for multiple genotypes can be cumbersome and expensive. Ultimately, one can test a large range of genomic

heterogeneity of medulloblastoma cancer subtypes in a single construct. To do so, one should extract different cell lines from the biopsy samples, acquired from National Disease Research Interchange (NDRI) for example. By determining the responsive population of the medulloblastoma cancer cells, one can assess the efficacy of drugs for all genotypes at once.

Two major aberrant signaling patterns have been proposed for the development and/or maintenance of Hh pathway-dependent cancer: i) ligand-independent signaling and ii) ligand-dependent paracrine signaling. In the case of basal cell carcinoma, almost all tumors show evidence of genetic aberration in Hh pathway (i.e. constitutive ligand-independent Hh pathway activity). However, the situation is quite different in medulloblastoma, where only ~30% of the tumors show mutation in Hh pathway, which is indicative of Hh pathway ligand-independent activation. This distinction is important clinically because other types of medulloblastoma tumors, which are responsive to therapy *in vivo* but not *in vitro*, may follow the ligand-dependent signaling pattern.

This platform can distinguish these two mechanisms by following the *in vitro* drug treatment for one of the constructs as a test group, and having the untreated animal as control. Tumor cell types which showed considerable change in the measured metrics among test and control groups (e.g. spheroid diameter), could follow the first signaling pattern or both the first and the second signaling pattern. However, the tumor cell lines which showed no changes in the measured metrics could be inhibited only by the second mechanism, ligand-dependent paracrine signaling. Hence, we are determining a subset of the medulloblastoma cell lines which are responsive to anti-Hh treatment but not through direct inhibition. Identifying the mechanism of inhibition of tumor growth by HhAntag could be influential in determining the mechanism of drug resistance: in a recent clinical case of metastatic adult medulloblastoma, the patient relapsed because of

mutation of the drug-binding site in SMO in tumor cells which might not be the case for other tumor subtypes which proliferate via paracrine signaling. The testing of such signaling mechanisms in an animal host for a large number of cancer genotypes, even though such knowledge may influence the course of treatment, remains challenging using conventional *in vitro* or animal host models.

Bibliography

1. Weiner, N., *Cybernetics or Control and Communication in the Animal and the Machine* 1948, Cambridge: MIT Press.
2. Wurm, M., et al., *Microtechnology meets systems biology: the small molecules of metabolome as next big targets.* J Biotechnol, 2010. **149**(1-2): p. 33-51.
3. Peirce, S.M., *Computational and mathematical modeling of angiogenesis.* Microcirculation, 2008. **15**(8): p. 739-51.
4. Jemal, A., et al., *Global cancer statistics.* CA Cancer J Clin, 2011. **61**(2): p. 69-90.
5. Shoemaker, R.H., *The NCI60 human tumour cell line anticancer drug screen.* Nat Rev Cancer, 2006. **6**(10): p. 813-23.
6. Kane, R.S., et al., *Patterning proteins and cells using soft lithography.* Biomaterials, 1999. **20**(23-24): p. 2363-76.
7. Chiu, D.T., et al., *Patterned deposition of cells and proteins onto surfaces by using three-dimensional microfluidic systems.* Proc Natl Acad Sci U S A, 2000. **97**(6): p. 2408-13.
8. Sia, S.K. and G.M. Whitesides, *Microfluidic devices fabricated in poly(dimethylsiloxane) for biological studies.* Electrophoresis, 2003. **24**(21): p. 3563-76.
9. Squires, T.M., R.J. Messinger, and S.R. Manalis, *Making it stick: convection, reaction and diffusion in surface-based biosensors.* Nat Biotechnol, 2008. **26**(4): p. 417-26.
10. Basu, S., et al., *A synthetic multicellular system for programmed pattern formation.* Nature, 2005. **434**(7037): p. 1130-4.
11. Hooshangi, S. and W.E. Bentley, *From unicellular properties to multicellular behavior: bacteria quorum sensing circuitry and applications.* Curr Opin Biotechnol, 2008. **19**(6): p. 550-5.
12. Hilgenfeldt, S., S. Erisken, and R.W. Carthew, *Physical modeling of cell geometric order in an epithelial tissue.* Proc Natl Acad Sci U S A, 2008. **105**(3): p. 907-11.
13. Keller, P.J., et al., *Reconstruction of Zebrafish Early Embryonic Development by Scanned Light Sheet Microscopy.* Science, 2008. **322**(5904): p. 1065-1069.
14. Blanchard, G.B., et al., *Tissue tectonics: morphogenetic strain rates, cell shape change and intercalation.* Nature Methods, 2009. **6**(6): p. 458-U86.

15. Carmeliet, P., *Angiogenesis in life, disease and medicine.* Nature, 2005. **438**(7070): p. 932-6.
16. Jain, R.K., et al., *Engineering vascularized tissue.* Nature Biotechnology, 2005. **23**(7): p. 821-823.
17. Folkman, J. and C. Haudenschild, *Angiogenesis Invitro.* Nature, 1980. **288**(5791): p. 551-556.
18. Jain, R.K., et al., *Quantitative angiogenesis assays: progress and problems.* Nat Med, 1997. **3**(11): p. 1203-8.
19. Auerbach, R., et al., *Angiogenesis assays: a critical overview.* Clin Chem, 2003. **49**(1): p. 32-40.
20. Donovan, D., et al., *Comparison of three in vitro human 'angiogenesis' assays with capillaries formed in vivo.* Angiogenesis, 2001. **4**(2): p. 113-21.
21. Kubota, Y., et al., *Role of Laminin and Basement-Membrane in the Morphological-Differentiation of Human-Endothelial Cells into Capillary-Like Structures.* Journal of Cell Biology, 1988. **107**(4): p. 1589-1598.
22. Vailhe, B., et al., *The formation of tubular structures by endothelial cells is under the control of fibrinolysis and mechanical factors.* Angiogenesis, 1998. **2**(4): p. 331-44.
23. Staton, C.A., et al., *Current methods for assaying angiogenesis in vitro and in vivo.* Int J Exp Pathol, 2004. **85**(5): p. 233-48.
24. Serini, G., et al., *Modeling the early stages of vascular network assembly.* EMBO J, 2003. **22**(8): p. 1771-9.
25. Drake, C.J., *Embryonic and adult vasculogenesis.* Birth Defects Res C Embryo Today, 2003. **69**(1): p. 73-82.
26. Zaman, M.H., et al., *Migration of tumor cells in 3D matrices is governed by matrix stiffness along with cell-matrix adhesion and proteolysis.* Proc Natl Acad Sci U S A, 2006. **103**(29): p. 10889-94.
27. Bautch, V.L., *Endothelial cells form a phalanx to block tumor metastasis.* Cell, 2009. **136**(5): p. 810-2.
28. Jain, R.K., *Normalization of tumor vasculature: an emerging concept in antiangiogenic therapy.* Science, 2005. **307**(5706): p. 58-62.

29. Megason, S.G. and S.E. Fraser, *Imaging in systems biology.* Cell, 2007. **130**(5): p. 784-795.

30. Keren, K., et al., *Mechanism of shape determination in motile cells.* Nature, 2008. **453**(7194): p. 475-U1.

31. Ambler, C.A., et al., *Assembly of trunk and limb blood vessels involves extensive migration and vasculogenesis of somite-derived angioblasts.* Dev Biol, 2001. **234**(2): p. 352-64.

32. Schmidt, A., K. Brixius, and W. Bloch, *Endothelial precursor cell migration during vasculogenesis.* Circ Res, 2007. **101**(2): p. 125-36.

33. Coveney, D., et al., *Four-dimensional analysis of vascularization during primary development of an organ, the gonad.* Proceedings of the National Academy of Sciences of the United States of America, 2008. **105**(20): p. 7212-7217.

34. Arnaoutova, I. and H.K. Kleinman, *In vitro angiogenesis: endothelial cell tube formation on gelled basement membrane extract.* Nat Protoc, 2010. **5**(4): p. 628-35.

35. Meade-Tollin, L.C. and C.J. Van Noorden, *Time lapse phase contrast video microscopy of directed migration of human microvascular endothelial cells on matrigel.* Acta Histochem, 2000. **102**(3): p. 299-307.

36. Griffith, L.G. and G. Naughton, *Tissue Engineering--Current Challenges and Expanding Opportunities.* Science, 2002. **295**(5557): p. 1009-1014.

37. Oates, A.C., et al., *Quantitative approaches in developmental biology.* Nature Reviews Genetics, 2009. **10**(8): p. 517-530.

38. Muzzey, D., et al., *A systems-level analysis of perfect adaptation in yeast osmoregulation.* Cell, 2009. **138**(1): p. 160-71.

39. Bansal, N., A. Blum, and S. Chawla, *Correlation clustering.* Machine Learning, 2004. **56**(1-3): p. 89-113.

40. Gramm, J., et al., *Graph-modeled data clustering: Exact algorithms for clique generation.* Theory of Computing Systems, 2005. **38**(4): p. 373-392.

41. Cai, Y., et al., *Cytoskeletal coherence requires myosin-IIA contractility.* J Cell Sci, 2010. **123**(Pt 3): p. 413-23.

42. Ishizaki, T., et al., *Pharmacological properties of Y-27632, a specific inhibitor of rho-associated kinases.* Mol Pharmacol, 2000. **57**(5): p. 976-83.

43. Gramm, J., et al., *Graph-modeled data clustering: Fixed-parameter algorithms for clique generation.* Algorithms and Complexity, Proceedings, 2003. **2653**: p. 108-119.
44. Maeda, Y.T., et al., *Ordered patterns of cell shape and orientational correlation during spontaneous cell migration.* Plos One, 2008. **3**(11): p. e3734.
45. Friedl, P. and D. Gilmour, *Collective cell migration in morphogenesis, regeneration and cancer.* Nat Rev Mol Cell Biol, 2009. **10**(7): p. 445-57.
46. Vitorino, P. and T. Meyer, *Modular control of endothelial sheet migration.* Genes & Development, 2008. **22**(23): p. 3268-3281.
47. Connolly, J.O., et al., *Rac regulates endothelial morphogenesis and capillary assembly.* Mol Biol Cell, 2002. **13**(7): p. 2474-85.
48. Swain, P.S., M.B. Elowitz, and E.D. Siggia, *Intrinsic and extrinsic contributions to stochasticity in gene expression.* Proc Natl Acad Sci U S A, 2002. **99**(20): p. 12795-800.
49. De Smet, F., et al., *Mechanisms of vessel branching: filopodia on endothelial tip cells lead the way.* Arterioscler Thromb Vasc Biol, 2009. **29**(5): p. 639-49.
50. Aird, W.C., *Phenotypic heterogeneity of the endothelium: I. Structure, function, and mechanisms.* Circ Res, 2007. **100**(2): p. 158-73.
51. Mammoto, A., et al., *A mechanosensitive transcriptional mechanism that controls angiogenesis.* Nature, 2009. **457**(7233): p. 1103-U57.
52. Matouk, C.C. and P.A. Marsden, *Epigenetic regulation of vascular endothelial gene expression.* Circ Res, 2008. **102**(8): p. 873-87.
53. Kamei, M., et al., *Endothelial tubes assemble from intracellular vacuoles in vivo.* Nature, 2006. **442**(7101): p. 453-6.
54. Juliano, R.L. and S. Haskill, *Signal transduction from the extracellular matrix.* J Cell Biol, 1993. **120**(3): p. 577-85.
55. Martin, P., *Wound healing--aiming for perfect skin regeneration.* Science, 1997. **276**(5309): p. 75-81.
56. Bernstein, L.R. and L.A. Liotta, *Molecular mediators of interactions with extracellular matrix components in metastasis and angiogenesis.* Curr Opin Oncol, 1994. **6**(1): p. 106-13.

57. Dickinson, R.B. and R.T. Tranquillo, *Optimal Estimation of Cell-Movement Indexes from the Statistical-Analysis of Cell Tracking Data.* Aiche Journal, 1993. **39**(12): p. 1995-2010.

58. Vogel, V. and M. Sheetz, *Local force and geometry sensing regulate cell functions.* Nature Reviews Molecular Cell Biology, 2006. **7**(4): p. 265-275.

59. Curtze, S., et al., *Dynamic changes in traction forces with DC electric field in osteoblast-like cells.* J Cell Sci, 2004. **117**(Pt 13): p. 2721-9.

60. Lamalice, L., F. Le Boeuf, and J. Huot, *Endothelial cell migration during angiogenesis.* Circ Res, 2007. **100**(6): p. 782-94.

61. Lo, C.M., et al., *Cell movement is guided by the rigidity of the substrate.* Biophysical Journal, 2000. **79**(1): p. 144-152.

62. Reinhart-King, C.A., M. Dembo, and D.A. Hammer, *Cell-Cell Mechanical Communication through Compliant Substrates.* Biophysical Journal, 2008. **95**(12): p. 6044-6051.

63. Dzyubachyk, O., et al., *Automated analysis of time-lapse fluorescence microscopy images: from live cell images to intracellular foci.* Bioinformatics, 2010. **26**(19): p. 2424-30.

64. Pan, B., et al., *Full-field strain measurement using a two-dimensional Savitzky-Golay digital differentiator in digital image correlation.* Optical Engineering, 2007. **46**(3).

65. Fung, Y.C., *Biomechanics: Mechanical Properties of Living Tissues*. 1993: Springer.

66. Parsa, H., R. Upadhyay, and S.K. Sia, *Uncovering the behaviors of individual cells within a multicellular microvascular community.* Proc Natl Acad Sci U S A, 2011. **108**(12): p. 5133-8.

67. Stevenson, M.D., et al., *Pericellular conditions regulate extent of cell-mediated compaction of collagen gels.* Biophys J, 2010. **99**(1): p. 19-28.

68. Kohen, N.T., L.E. Little, and K.E. Healy, *Characterization of Matrigel interfaces during defined human embryonic stem cell culture.* Biointerphases, 2009. **4**(4): p. 69-79.

69. Manz, A. and J.C.T. Eijkel, *Miniaturization and chip technology. What can we expect?* Pure and Applied Chemistry, 2001. **73**(10): p. 1555-1561.

70. Lion, N., et al., *Why the move to microfluidics for protein analysis?* Current Opinion in Biotechnology, 2004. **15**(1): p. 31-37.

71. Beebe, D.J., G.A. Mensing, and G.M. Walker, *Physics and applications of microfluidics in biology.* Annu Rev Biomed Eng, 2002. **4**: p. 261-86.

72. Brody, J., et al., *Biotechnology at low Reynolds numbers.* Biophys J, 1996. **71**(6): p. 3430-3441.

73. Chin, C.D., V. Linder, and S.K. Sia, *Lab-on-a-chip devices for global health: past opportunities and future challenges.* Lab Chip, 2007.

74. Bange, A., H.B. Halsall, and W.R. Heineman, *Microfluidic immunosensor systems.* Biosensors and Bioelectronics, 2004. **20**(12): p. 2488-2503.

75. Wild, D., *The Immunoassay Handbook.* 3rd edition ed. 2005: Elsevier Science.

76. Trobe, J.D. and G.J. Kost, *Principles & Practice of Point-of-care Testing*. 2002: Lippincott Williams & Wilkins.

77. Delamarche, E., D. Juncker, and H. Schmid, *Microfluidics for Processing Surfaces and Miniaturizing Biological Assays.* Adv Mat, 2005. **17**(24): p. 2911-2933.

78. Linder, V., S.K. Sia, and G.M. Whitesides, *Reagent-loaded cartridges for valveless and automated fluid delivery in microfluidic devices.* Anal. Chem., 2005. **77**: p. 64-71.

79. Sia, S.K., et al., *An integrated approach to a portable and low-cost immunoassay for resource-poor settings.* Angewandte Chemie-International Edition, 2004. **43**(4): p. 498-502.

80. Gupta, S., et al., *Characterization and optimization of gold nanoparticle-based silver-enhanced immunoassays.* Anal Chem, 2007. **79**(10): p. 3810-20.

81. Rossier, J., F. Reymond, and P.E. Michel, *Polymer microfluidic chips for electrochemical and biochemical analyses.* Electrophoresis, 2002. **23**(6): p. 858-67.

82. Linder, V., et al., *Application of surface biopassivated disposable poly(dimethylsiloxane)/glass chips to a heterogeneous competitive human serum immunoglobulin G immunoassay with incorporated internal standard.* Electrophoresis, 2002. **23**(5): p. 740-9.

83. Dodge, A., et al., *Electrokinetically driven microfluidic chips with surface-modified chambers for heterogeneous immunoassays.* Anal Chem, 2001. **73**(14): p. 3400-9.

84. Bernard, A., B. Michel, and E. Delamarche, *Micromosaic immunoassays.* Anal Chem, 2001. **73**(1): p. 8-12.

85. Phillips, K.S. and Q. Cheng, *Microfluidic immunoassay for bacterial toxins with supported phospholipid bilayer membranes on poly(dimethylsiloxane).* Anal Chem, 2005. **77**(1): p. 327-34.

86. Dong, Y. and C. Shannon, *Heterogeneous immunosensing using antigen and antibody monolayers on gold surfaces with electrochemical and scanning probe detection.* Anal Chem, 2000. **72**(11): p. 2371-6.

87. Rossier, J.S. and H.H. Girault, *Enzyme linked immunosorbent assay on a microchip with electrochemical detection.* Lab Chip, 2001. **1**(2): p. 153-7.

88. Rossier, J.S., et al., *Characterization of Protein Adsorption and Immunosorption Kinetics in Photoablated Polymer Microchannels.* Langmuir, 2000. **16**(22): p. 8489 -8494.

89. Goldstein, B., et al., *The influence of transport on the kinetics of binding to surface receptors: application to cells and BIAcore.* J Mol Recognit, 1999. **12**(5): p. 293-9.

90. Zimmermann, M., et al., *Modeling and optimization of high-sensitivity, low-volume microfluidic-based surface immunoassays.* Biomed Microdevices, 2005. **7**(2): p. 99-110.

91. Hu, G., Y. Gao, and D. Li, *Modeling micropatterned antigen-antibody binding kinetics in a microfluidic chip.* Biosens Bioelectron, 2007. **22**(7): p. 1403-9.

92. Gervais, T. and K.F. Jensen, *Mass transport and surface reactions in microfluidic systems.* Chemical Engineering Science, 2006. **61**(4): p. 1102-1121.

93. Foley, J.O., et al., *Experimental and model investigation of the time-dependent 2-dimensional distribution of binding in a herringbone microchannel.* Lab Chip, 2008. **8**(4): p. 557-64.

94. Myszka, D.G., et al., *Extending the range of rate constants available from BIACORE: interpreting mass transport-influenced binding data.* Biophys J, 1998. **75**(2): p. 583-94.

95. de Mello, A.J. and N. Beard, *Dealing with real samples: sample pre-treatment in microfluidic systems.* Lab Chip, 2003. **3**(1): p. 11N-19N.

96. Zhou, J., S.F. Chen, and S.Y. Jiang, *Orientation of adsorbed antibodies on charged surfaces by computer simulation based on a united-residue model.* Langmuir, 2003. **19**(8): p. 3472-3478.

97. Jennissen, H.P. and T. Zumbrink, *A novel nanolayer biosensor principle.* Biosens Bioelectron, 2004. **19**(9): p. 987-97.

98. Gupta, S., et al., *Characterization and optimization of gold nanoparticle-based silver-enhanced immunoassays.* Analytical Chemistry, 2007. **79**(10): p. 3810-3820.

99. de la Escosura-Muniz, A., M.M.D. Costa, and A. Merkoci, *Controlling the electrochemical deposition of silver onto gold nanoparticles: Reducing interferences and increasing the sensitivity of magnetoimmuno assays.* Biosensors & Bioelectronics, 2009. **24**(8): p. 2475-2482.

100. Widegren, J.A. and R.G. Finke, *A review of the problem of distinguishing true homogeneous catalysis from soluble or other metal-particle heterogeneous catalysis under reducing conditions.* Journal of Molecular Catalysis a-Chemical, 2003. **198**(1-2): p. 317-341.

101. Patakfalvi, R., S. Papp, and I. Dekany, *The kinetics of homogeneous nucleation of silver nanoparticles stabilized by polymers.* Journal of Nanoparticle Research, 2007. **9**(3): p. 353-364.

102. Besson, C., E.E. Finney, and R.G. Finke, *A mechanism for transition-metal nanoparticle self-assembly.* Journal of the American Chemical Society, 2005. **127**(22): p. 8179-8184.

103. Watzky, M.A. and R.G. Finke, *Transition metal nanocluster formation kinetic and mechanistic studies. A new mechanism when hydrogen is the reductant: Slow, continuous nucleation and fast autocatalytic surface growth.* Journal of the American Chemical Society, 1997. **119**(43): p. 10382-10400.

104. Wild, D., *Separation systems*, in *The Immunoassay Handbook, 2nd Ed*, D. Wild, Editor. 2001, Nature Publishing Group: New York. p. 149-158.

105. Quake, S.R. and A. Scherer, *From micro- to nanofabrication with soft materials.* Science, 2000. **290**(5496): p. 1536-40.

106. Rogers, J.A. and R.G. Nuzzo, *Recent progress in soft lithography.* Materials Today, 2005. **8**(2): p. 50-56.

107. Whitesides, G.M., et al., *Soft lithography in biology and biochemistry.* Annu Rev Biomed Eng, 2001. **3**: p. 335-73.

108. Lee, P.J., et al., *Nanoliter scale microbioreactor array for quantitative cell biology.* Biotechnol Bioeng, 2006. **94**(1): p. 5-14.

109. Tourovskaia, A., X. Figueroa-Masot, and A. Folch, *Differentiation-on-a-chip: a microfluidic platform for long-term cell culture studies.* Lab Chip, 2005. **5**(1): p. 14-9.

110. Bhatia, S.N., et al., *Microfabrication of hepatocyte/fibroblast co-cultures: role of homotypic cell interactions.* Biotechnol Prog, 1998. **14**(3): p. 378-87.

111. Griffith, L.G. and M.A. Swartz, *Capturing complex 3D tissue physiology in vitro.* Nat Rev Mol Cell Biol, 2006. **7**(3): p. 211-24.

112. Raines, E.W., *The extracellular matrix can regulate vascular cell migration, proliferation, and survival: relationships to vascular disease.* Int J Exp Pathol, 2000. **81**(3): p. 173-82.

113. Abbott, A., *Cell culture: biology's new dimension.* Nature, 2003. **424**(6951): p. 870-2.

114. Tan, W. and T.A. Desai, *Microscale multilayer cocultures for biomimetic blood vessels.* J Biomed Mater Res A, 2005. **72**(2): p. 146-60.

115. Toh, Y.C., et al., *A novel 3D mammalian cell perfusion-culture system in microfluidic channels.* Lab Chip, 2007. **7**(3): p. 302-9.

116. Ling, Y., et al., *A cell-laden microfluidic hydrogel.* Lab Chip, 2007. **7**(6): p. 756-62.

117. Gottwald, E., et al., *A chip-based platform for the in vitro generation of tissues in three-dimensional organization.* Lab Chip, 2007. **7**(6): p. 777-85.

118. Figallo, E., et al., *Micro-bioreactor array for controlling cellular microenvironments.* Lab Chip, 2007. **7**(6): p. 710-9.

119. Cheung, Y.K., et al., *Direct patterning of composite biocompatible microstructures using microfluidics.* Lab Chip, 2007. **7**(5): p. 574-9.

120. Albrecht, D.R., et al., *Probing the role of multicellular organization in three-dimensional microenvironments.* Nat Methods, 2006. **3**(5): p. 369-75.

121. Thorsen, T., S.J. Maerkl, and S.R. Quake, *Microfluidic large-scale integration.* Science, 2002. **298**(5593): p. 580-4.

122. Grover, W.H., et al., *Development and multiplexed control of latching pneumatic valves using microfluidic logical structures.* Lab Chip, 2006. **6**(5): p. 623-31.

123. Kleinman, H.K. and G.R. Martin, *Matrigel: basement membrane matrix with biological activity.* Semin Cancer Biol, 2005. **15**(5): p. 378-86.

124. Abilez, O., et al., *A novel culture system shows that stem cells can be grown in 3D and under physiologic pulsatile conditions for tissue engineering of vascular grafts.* J Surg Res, 2006. **132**(2): p. 170-8.

125. Frisk, T., et al., *A concept for miniaturized 3-D cell culture using an extracellular matrix gel.* Electrophoresis, 2005. **26**(24): p. 4751-8.

126. Unger, M.A., et al., *Monolithic microfabricated valves and pumps by multilayer soft lithography.* Science, 2000. **288**(5463): p. 113-6.

127. Swartz, M.A. and M.E. Fleury, *Interstitial flow and its effects in soft tissues.* Annu Rev Biomed Eng, 2007. **9**: p. 229-56.

128. Ng, C.P. and M.A. Swartz, *Fibroblast alignment under interstitial fluid flow using a novel 3-D tissue culture model.* Am J Physiol Heart Circ Physiol, 2003. **284**(5): p. H1771-7.

129. Butler, S.L., et al., *Interstitial fluid flow in tendons or ligaments: a porous medium finite element simulation.* Med Biol Eng Comput, 1997. **35**(6): p. 742-6.

130. Wang, S. and J.M. Tarbell, *Effect of fluid flow on smooth muscle cells in a 3-dimensional collagen gel model.* Arterioscler Thromb Vasc Biol, 2000. **20**(10): p. 2220-5.

131. Pedersen, J.A., F. Boschetti, and M.A. Swartz, *Effects of extracellular fiber architecture on cell membrane shear stress in a 3D fibrous matrix.* J Biomech, 2007. **40**(7): p. 1484-92.

132. Cukierman, E., et al., *Taking cell-matrix adhesions to the third dimension.* Science, 2001. **294**(5547): p. 1708-12.

133. Biosciences, B.D., *Product Literature-MATRIGEL.* 2003. **1**: p. 4-5.

134. Arufe, M.C., et al., *Directed differentiation of mouse embryonic stem cells into thyroid follicular cells.* Endocrinology, 2006. **147**(6): p. 3007-15.

135. Albrecht, D.R., et al., *Multiphase electropatterning of cells and biomaterials.* Lab Chip, 2007. **7**(6): p. 702-9.

136. Fleury, M.E., K.C. Boardman, and M.A. Swartz, *Autologous morphogen gradients by subtle interstitial flow and matrix interactions.* Biophys J, 2006. **91**(1): p. 113-21.

137. Davey, R.E., et al., *LIF-mediated control of embryonic stem cell self-renewal emerges due to an autoregulatory loop.* FASEB J, 2007. **21**(9): p. 2020-32.

138. Hwang, N.S., et al., *Effects of three-dimensional culture and growth factors on the chondrogenic differentiation of murine embryonic stem cells.* Stem Cells, 2006. **24**(2): p. 284-91.

139. Wang, X., et al., *Proliferation and differentiation of mouse embryonic stem cells in APA microcapsule: A model for studying the interaction between stem cells and their niche.* Biotechnol Prog, 2006. **22**(3): p. 791-800.

140. Ostrovidov, S., et al., *Membrane-based PDMS microbioreactor for perfused 3D primary rat hepatocyte cultures.* Biomed Microdevices, 2004. **6**(4): p. 279-87.

141. Eschbach, E., et al., *Microstructured scaffolds for liver tissue cultures of high cell density: morphological and biochemical characterization of tissue aggregates.* J Cell Biochem, 2005. **95**(2): p. 243-55.

142. Gomez-Sjoberg, R., et al., *Versatile, Fully Automated, Microfluidic Cell Culture System.* Anal Chem, 2007.